REPORT DOCUMENTATION PAGE

Public reporting burden for this collection of information is estimated to average 1 hour per response, including the time for reviewing instructions, searching existing data sources, gathering and maintaining the data needed, and completing and reviewing this collection of information. Send comments regarding this burden estimate or any other aspect of this collection of information, including suggestions for reducing this burden to Department of Defense, Washington Headquarters Services, Directorate for Information Operations and Reports (0704-0188), 1215 Jefferson Davis Highway, Suite 1204, Arlington, VA 22202-4302. Respondents should be aware that notwithstanding any other provision of law, no person shall be subject to any penalty for failing to comply with a collection of information if it does not display a currently valid OMB control number. **PLEASE DO NOT RETURN YOUR FORM TO THE ABOVE ADDRESS.**

1. REPORT DATE *(DD-MM-YYYY)*	2. REPORT TYPE	3. DATES COVERED *(From - To)*
30 August 2015	Thesis	15 June 2015- 30 August 2015

4. TITLE AND SUBTITLE	5a. CONTRACT NUMBER
High Temperature Latent Heat Thermal Energy Storage To Augment Solar Thermal Propulsion for Micro. Sats	
	5b. GRANT NUMBER
	5c. PROGRAM ELEMENT NUMBER

6. AUTHOR(S)	5d. PROJECT NUMBER
Matthew R. Gilpin	
	5e. TASK NUMBER
	5f. WORK UNIT NUMBER
	Q0CA

7. PERFORMING ORGANIZATION NAME(S) AND ADDRESS(ES)	8. PERFORMING ORGANIZATION REPORT NO.
Air Force Research Laboratory (AFMC) AFRL/RQRS 1 Ara Drive Edwards AFB, CA 93524-7013	

9. SPONSORING / MONITORING AGENCY NAME(S) AND ADDRESS(ES)	10. SPONSOR/MONITOR'S ACRONYM(S)
Air Force Research Laboratory (AFMC) AFRL/RQR 5 Pollux Drive Edwards AFB, CA 93524-7048	
	11. SPONSOR/MONITOR'S REPORT NUMBER(S)
	AFRL-RQ-ED-OT-2015-265

12. DISTRIBUTION / AVAILABILITY STATEMENT
Approved for public release; distribution unlimited

13. SUPPLEMENTARY NOTES
For submission for USC Thesis paper (August 2015)
PA Case Number: # 15347; Clearance Date: 6/26/2015

14. ABSTRACT
Solar thermal propulsion (STP) offers an unique combination of thrust and efficiency, providing greater total ΔV capability than chemical propulsion systems without the order of magnitude increase in total mission duration associated with electric propulsion. Despite a over 50 year development history, no STP spacecraft has flown to-date as both perceived and actual complexity have overshadowed the potential performance benefit in relation to conventional technologies. The trend in solar thermal research over the past two decades has been towards simplification and miniaturization to overcome this complexity barrier in an effort finally mount an in-flight test. A review of micro-propulsion technologies recently conducted by the Air Force Research Laboratory (AFRL) has identified solar thermal propulsion as a promising configuration for microsatellite missions requiring a substantial ΔV and recommended further study. A STP system provides performance which cannot be matched by conventional propulsion technologies in the context of the proposed microsatellite "inspector" requiring rapid delivery of greater than 1500 m=s ΔV. With this mission profile as the target, the development of an effective STP architecture goes beyond incremental improvements and enables a new class of microsatellite missions. Here, it is proposed that a bi-modal solar thermal propulsion system on a microsatellite platform can provide a greater than 50% increase in ΔV vs. chemical systems while maintaining delivery times measured in days. The realization of a microsatellite scale bi-modal STP system requires the integration of multiple new technologies, and with the exception of high performance thermal energy storage, the long history of STP development has provided "ready" solutions.

15. SUBJECT TERMS
N/A

16. SECURITY CLASSIFICATION OF:			17. LIMITATION OF ABSTRACT	18. NUMBER OF PAGES	19a. NAME OF RESPONSIBLE PERSON M. Young
a. REPORT Unclassified	b. ABSTRACT Unclassified	c. THIS PAGE Unclassified	SAR	176	19b. TELEPHONE NO *(include area code)* N/A

HIGH TEMPERATURE LATENT HEAT THERMAL ENERGY STORAGE TO AUGMENT

SOLAR THERMAL PROPULSION FOR MICROSATELLITES

by

Matthew R. Gilpin

_____

A Dissertation Presented to the

FACULTY OF THE GRADUATE SCHOOL

UNIVERSITY OF SOUTHERN CALIFORNIA

In Partial Fulfillment of the

Requirements for the Degree

DOCTOR OF PHILOSOPHY

(AEROSPACE ENGINEERING)

August 2015

Dedication

For My Parents - Engineers aren't born, they're made.

To Katharine - So glad we made it! ♫

Acknowledgments

First and foremost, I must acknowledge the support I have received from the Air Force Research Laboratory throughout my nine years at USC. I am incredibly grateful for the opportunities I have received and the research career that I have been afforded. I especially need to thank Dr. Marcus Young and Dr. David Scharfe for shepherding me through this project and giving a young intern the chance to excel.

I also owe a great debt to the mentors that convinced me to pursue a Ph.D. A special thanks goes to Dr. Anthony Pancotti for demonstrating a commitment to expanding the boundaries of technology and pushing me to also look further. I also need to thank Dr. Taylor Lilly, Dr. Andrew Ketsdever and Dr. Nate Selden. When I was first hired in CHAFF, I could not have imagined the opportunity I faced, and as I reflect on my time at USC as an undergraduate, Masters and Ph.D student, no other experience - either personal, professional or academic - has had a more profound impact on my life goals.

In addition to the AFRL, this work would not have been possible without an extremely dedicated and capable team of undergraduate and graduate students. Matthew Orr, Martin Hilario, Turner Topping, Rayed Kahn, Andy Su, Mallory Smith and Gavin Moler - your contributions were essential to this research effort.

Finally, I must thank the ARCS foundation for their support in both my graduate and undergraduate studies. By providing financial stability during times of great turmoil, you made it possible to devote myself to advancing my research.

Table of Contents

List of Figures

List of Tables

Abstract

Solar thermal propulsion (STP) offers an unique combination of thrust and efficiency, providing greater total ΔV capability than chemical propulsion systems without the order of magnitude increase in total mission duration associated with electric propulsion. Despite a over 50 year development history, no STP spacecraft has flown to-date as both perceived and actual complexity have overshadowed the potential performance benefit in relation to conventional technologies. The trend in solar thermal research over the past two decades has been towards simplification and miniaturization to overcome this complexity barrier in an effort finally mount an in-flight test.

A review of micro-propulsion technologies recently conducted by the Air Force Research Laboratory (AFRL) has identified solar thermal propulsion as a promising configuration for microsatellite missions requiring a substantial ΔV and recommended further study. A STP system provides performance which cannot be matched by conventional propulsion technologies in the context of the proposed microsatellite "inspector" requiring rapid delivery of greater than 1500 m/s ΔV. With this mission profile as the target, the development of an effective STP architecture goes beyond incremental improvements and enables a new class of microsatellite missions.

Here, it is proposed that a bi-modal solar thermal propulsion system on a microsatellite platform can provide a greater than 50% increase in ΔV vs. chemical systems while maintaining delivery times measured in days. The realization of a microsatellite scale bi-modal STP system requires the integration of multiple new technologies, and with the exception of high performance thermal energy storage, the long history of STP development has provided "ready" solutions.

For the target bi-modal STP microsatellite, sensible heat thermal energy storage is insufficient and the development of high temperature latent heat thermal energy storage is an enabling technology for the platform. The use of silicon and boron as high temperature latent heat thermal energy storage materials has been in the background of solar thermal research for decades without a substantial investigation despite a broad agreement in the literature about the performance benefits obtainable through high energy storage density and quasi-isothermal heat release at high temperature.

In this work, an experimental approach was taken to uncover the practical concerns associated specifically with applying silicon as an energy storage material. A new solar furnace was built and characterized enabling the creation of molten silicon in the laboratory. These tests have demonstrated the basic feasibility of a molten silicon based thermal energy storage system and have highlighted asymmetric heat transfer as well as silicon expansion damage to be the primary engineering concerns for the technology. For cylindrical geometries, it has been shown that reduced fill factors can prevent damage to graphite walled silicon containers at the expense of decreased energy storage density.

Concurrent with experimental testing, a cooling model was written using the "enthalpy method" to calculate the phase change process and predict test section performance. Despite a simplistic phase change model, and experimentally demonstrated complexities of the freezing process, results coincided with experimental data. It is thus possible to capture essential system behaviors of a latent heat thermal energy storage system even with low fidelity freezing kinetics modeling allowing the use of standard tools to obtain reasonable results.

Finally, a technological road map is provided listing extant technological concerns and potential solutions. Improvements in container design and an increased understanding of convective coupling efficiency will ultimately enable both high temperature latent heat thermal energy storage and a new class of high performance bi-modal solar thermal spacecraft.

<div align="right">

Chapter 1

</div>

Introduction

1.1 Propulsion for High Performance Microsatellite Missions

The principle motivation for this research effort was a review of microsatellite propulsion technologies published by the Advanced Concepts Propulsion Group of the Air Force Research Laboratory (AFRL) in 2009 [1]. This review highlighted the known utility and cost reductions possible when using a microsatellite platform and identified a robust propulsion mechanism as an enabling technology for a new class of fast response missions. Enhancing propulsion capability increases the range of orbit change maneuvers for what is inherently a lower cost, lower time to orbit spacecraft and also increases the availability of launch options [2, 3].

The AFRL review proposed a mission profile for a 200 kg microsatellite "inspector" requiring a 1.5 km/s ΔV capability and evaluated the readiness of various technologies to meet this aggressive target. Chemical propulsion options in the form of miniaturized bi-propellant and monopropellant thrusters were explored targeting high thrust, low power operation. While the miniaturized bi-propellant system was seen as an ideal solution, it was noted that the technology was in extremely early-stage development. Electric propulsion options were also explored but low power availability on a microsatellite limits thrust levels, resulting in mission times measured in months and years as opposed to days. When considering near-term technology, a high performance microsatellite

<div align="right">

1

</div>

must rely on relatively inefficient monopropellant chemical thrusters capable of meeting mission duration requirements at the expense of reduced payload mass.

The review also highlighted the unique possibilities of a solar thermal propulsion system. Solar thermal propulsion, even when using non-cryogenic propellants such as ammonia, maintains relatively high thrust levels while exceeding the efficiency of mono and bi-propellant chemical systems. Thus, the mission requirements for a microsatellite "inspector" are met with only a slight increase in mission time compared to non-chemical options while maintaining a reasonable payload mass fraction. It was recommended that solar thermal microsatellite concept be further explored as a potential near term solution to enable the proposed microsatellite mission.

1.2   State of Solar Thermal Propulsion

Solar thermal propulsion (STP) uses concentrated sunlight to add thermal energy to a gaseous propellant which is then ejected through a conventional nozzle to produce thrust. This relatively simple concept has been under development since the mid 1950s when it was first proposed as a means of reducing launch mass by eliminating the need for a separate oxidizer. Despite over fifty years of development, and a unique combination of thrust and efficiency, no STP systems have flown to-date. Progress of STP technology has been limited by concerns over perceived system complexity, storage of cryogenic propellants, power loss when in eclipse and the mission impact of requiring a separate thermal collection system in addition to standard photovoltaics and batteries.

The majority of early solar thermal development was focused on the deployment of large scale spacecraft where solar thermal was used to compete with existing cryogenic bi-propellant technology. The proposed systems offered significant efficiency advantages but the scale required the development of large solar concentrators and mechanisms for coupling collected solar energy effectively into the working fluid. The thermal energy subsystem had to co-exist with conventional

2

components on the spacecraft and as a result, solar thermal propulsion gained a reputation as a promising yet complicated design.

A seminal report published in 1979 by Rockwell International was the first systems level effort to define a 28,100 kg solar thermal spacecraft and the findings became the basis for the next decade of solar thermal development [4]. Work was focused on producing prototype solar receivers, heat exchangers, inflatable solar concentrator designs and relevant ground test facilities with the goal of a spaceflight demonstration. By 1989, the technology was declared feasible but budget cuts at what was then the Air Force Rocket Propulsion Laboratory (AFRPL) terminated further study.

The next phase of solar thermal development focused on a bi-modal operational concept where the thermal sub-system on board the spacecraft is used for electrical power generation in addition to propulsion. This advancement greatly reduced the perceived complexity of a solar thermal spacecraft and the Integrated Solar Upper Stage program (ISUS) was begun to develop a flight ready system by the close of the decade. While ultimately unsuccessful in mounting a flight mission, the ISUS program did succeed in ground testing a prototype thermal energy receiver and storage mechanism. In contrast to previous development efforts which viewed thermal energy storage as unnecessary, the proposed bi-modal configuration necessitated the inclusion of graphite as a sensible heat thermal energy storage material. Termination of the ISUS program marked the end of large-scale solar thermal development. But, it should be noted that for the second time, STP was put on hold for budgetary, as opposed to technological reasons.

In the aftermath of the ISUS program, solar thermal technology was explored as a potential propulsion mechanism for microsatellites. Seeing microsatellites as a low cost, attainable launch opportunity, researchers focused on simplicity in an effort to finally mount a space demonstration of STP. Reduced power requirements resulted in inflatable solar concentrators being replaced by rigid thin film designs and cryogenic propellants were neglected in favor of lower performance yet more easily sortable propellants such as ammonia. Despite a unique and relatively low cost proposal, STP development again stalled due to a lack of funding.

3

In this work, the bi-modal concepts developed during the 1990's and the recent microsatellite efforts are combined to propose a bi-modal solar thermal microsatellite as the technological evolution of the STP concept. The deployment and the associated risks of an inherently novel spacecraft architecture have prohibited the flight of any STP concept to-date. For such a system to be realized, STP must provide significant performance benefits. In the context of a high-performance microsatellite as proposed by the AFRL, a bi-modal solar thermal concept can provide significant (35-60% discussed in this work) ΔV increase over chemical propulsion while maintaining the necessary responsivity.

Over half a century of STP development has produced "ready" solutions for the majority of technologies required to develop a bi-modal solar thermal microsatellite and a technological review has determined that a high performance energy storage mechanism is the only remaining hurdle to the development of an effective STP spacecraft.

1.3   Thermal Energy Storage

To date, all solar thermal propulsion efforts containing thermal energy storage have utilized the sensible heat of materials such as graphite and boron carbide. Sensible heat thermal energy storage can provide adequate performance for large spacecraft. However, on a microsatellite platform with tight mass and volume constraints, the energy storage density is insufficient. Additionally, a bi-modal architecture with radiatively coupled thermophotovoltaic converters is highly affected by the large temperature swings inherent in sensible heat thermal energy storage.

Here it is proposed that a switch to latent heat thermal energy storage is required as the final enabling technology for a high performance solar thermal microsatelite. With sufficient thermal energy storage capacity, traditional photovoltaics and batteries can be removed from the spacecraft reducing propulsion and power system mass. Additionally, the relative temperature stability of latent heat release results in higher propulsive and electrical efficiency along with lower stresses on spacecraft components.

4

Transitioning to a latent heat system requires that a new class of thermal energy storage materials be developed. Both boron and silicon are presented as ideal candidates due to a combination of a high melting temperature and a high heat of fusion. In this work, boron is considered a long-term high performance solution and silicon is presented as a near term development target with potential terrestrial applications.

This effort is not the first to propose the use of silicon and boron as energy storage materials. In the existing solar thermal propulsion literature, both silicon and boron have been mentioned as thermal energy storage candidates in the context of broad conceptual studies. However, there have been no thorough investigations due to the absence of existing research in addition to cost and schedule constraints. For terrestrial applications, silicon is proposed as the "ideal" thermal energy storage material for thermophotovoltaic systems [5], but the existing literature is limited to 1-D studies and calculations based on basic material properties.

1.4   Scope of Research

The goal of this research is to determine the basic feasibility of high temperature latent heat thermal energy storage and to facilitate the development of a high performance bi-modal solar thermal microsatellite. An emphasis is placed on experimental demonstration as the existing literature lacks discussion of practical engineering concerns and viable solutions.

This work begins with a thorough literature review tracing the history of solar thermal propulsion and the natural evolution of the proposed bi-modal solar thermal propulsion system. The technological requirements of the proposed system are presented along with existing solutions identifying high temperature thermal energy storage as the final technological limitation. Both silicon and boron are identified as potential thermal energy storage candidates and two technological comparisons are presented demonstrating the performance benefits which can be gained.

5

To conduct experiments with molten silicon, a new solar furnace facility was built. Both the design and characterization are discussed here. Concurrent with solar furnace development, container materials were investigated and initial solar furnace tests were performed highlighting the need for multi-dimensional thermal modeling. This drove the development of an in-house MATLAB cooling model using the "enthalpy method" to calculate the silicon phase change process.

Molten silicon tests were performed using the solar furnace facility and results were compared against the in-house MATLAB model showing that macro system properties can be obtained using relatively simple phase change treatment. Experiments identified asymmetrical freezing as well as expansion damage to be the primary engineering limitations for high temperature latent heat thermal energy storage and a reliable design condition was identified for cylindrical geometries by reducing the fill factor of the phase change material container.

Finally, future research topics are presented with an emphasis on container development, long-term contamination testing, and convective coupling characterization of a latent heat gas blowdown system. Recent interest in nuclear thermal bi-modal space power systems is targeting silicon based latent heat thermal energy storage which provides potential motivation to further investigate these topics.

6

<div align="right">

Chapter 2

</div>

Solar Thermal Propulsion History

The concept of solar thermal propulsion has been under investigation since its proposal over 50 years ago seeking a combination of high thrust and high efficiency to reduce launch mass and expand satellite operations.

Early solar thermal propulsion development was focused on large spacecraft and presumed that solar thermal would be utilized purely as a propulsive mechanism. This resulted in highly complex architectures and concerns about vehicle integration limited the scale of solar thermal development and prevented in-space demonstration.

Ground test activity was focused on proof of concept solar thermal heat exchanger design and the feasibility of large scale solar concentrators.

In the early 1990s, the concept of a bi-modal solar thermal spacecraft was proposed where the thermal subsystem could be used for both propulsive and electrical power. This concept, combined with a general reduction in spacecraft scale, greatly simplified spacecraft designs. Individual components began to reach technological maturity and test campaigns demonstrated hardware for potential in-flight demonstrations. Ultimately, no missions were launched. However, bi-modal system development identified solar thermal as an ideal candidate for small, high performance satellites.

7
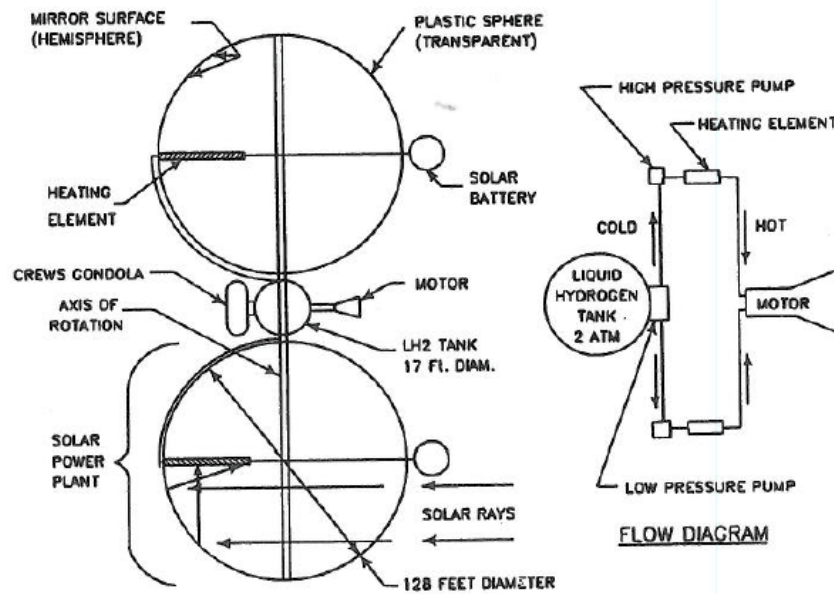
Figure 2.1: Ehricke's original proposed configuration for a solar thermal spacecraft [6]. Note that the location of the heat exchangers within the spherical concentrators requires extensive high temperature, high pressure plumbing.

2.1 Concept Proposal

Krafft Ehricke first proposed the concept of a solar thermal rocket in 1956 as a way to reduce launch mass and increase the energy supply for an orbiting satellite [6]. The proposed solar thermal rocket consisted of three primary components: the solar collector, a receiver/absorber and a propellant feed mechanism. The solar collector focuses energy into the receiver/absorber where the thermal energy is transfered to a propellant before it is ejected through a nozzle. As originally proposed by Ehricke, a prototype solar thermal spacecraft would have been relatively large and complex with a gross weight in excess of 7000 kg, a liquid hydrogen propellant mass fraction approaching 70% and two 39 m diameter inflatable spherical solar concentrators capable of generating modest propellant temperatures of approximately 1000 K. It is interesting to note that Ehricke's original proposal included a "solar battery" to provide electrical energy for the spacecraft. However, the conversion method was undefined as Ehricke's report pre-dates the use of spacecraft photovoltaics.

8

Following Ehricke's proposal, Electro-Optical Systems (EOS) conducted the first detailed experimental investigation of the solar thermal concept in 1963 using funding provided by the Air Force Rocket Propulsion Laboratory (AFRPL). This experimental effort successfully conducted hot flow hydrogen tests with a solar heated molybdenum absorber and tungsten-rhenium flow tubing. Using a 1.5 m diameter solar concentrator, EOS achieved hydrogen gas temperatures approaching 2300 K, which corresponds to a theoretical I_{sp} of approximately 700 s [7]. EOS demonstrated the feasibility of the basic solar rocket concept. However, work was halted due to both funding and technical concerns. In addition to large budget cuts which shifted development money to a competing advanced propulsion concept, there existed a perception in the propulsion community that the solar thermal rocket was an awkward design requiring extensive solar concentrators and long stretches of articulated plumbing. The EOS study scarcely approached the issue of "vehicle integration" and the scientific community found outstanding technological concerns sufficient to abandon the solar thermal rocket concept for over a decade [7].

2.2   Initial Developments

In the late 1970s, the advent of the space shuttle revived the solar thermal concept. The AFRPL saw the highly capable shuttle as an ideal candidate for placing a complicated solar thermal spacecraft into orbit and they believed that the space shuttle would provide a host of new mission scenarios well suited to solar rocket technology [4]. In 1979, the AFRPL funded an extensive study at Rockwell International and Ethridge's final project report became the foundation for the next 15 years of solar thermal research. Ethridge proposed the use of off-axis parabolic concentrators to focus sunlight into a centrally mounted receiver, greatly simplifying solar thermal spacecraft design. As can be seen in Figure 2.2, the use of a central receiver eliminated the extensive plumbing from Ehricke's proposal and allowed decoupling of solar concentration from the orientation of the spacecraft. Furthermore, off-axis parabolic concentrators offered improved optical performance

9

Table 2.1: LEO-GEO transfer analysis data reprinted from Ethridge for a space shuttle delivered 28,100 kg spacecraft [4]. Note that engine performance numbers represent the authors use of future estimates in 1979.

Engine Type	LO$_2$-H$_2$	Ion	Solar 1	Solar 2
ΔV, m/s	4270	5850	5850	4800
I_{sp}, s	475	2,940	872	872
Trip Time, $days$	5	180	14	40
Payload to GEO, kg	9,250	20,000	9,300	13,200

over spherical designs and avoided plume impingement on the concentrators themselves and other spacecraft components. Note that Ethridge did not include a mechanism for thermal storage.

In addition to examining the previously neglected issue of vehicle integration, Ethridge also performed an in depth analysis of solar thermal propulsion for transfer between low Earth orbit (LEO) and geosynchronous orbit (GEO). The LEO-GEO mission was analyzed using spacecraft scaled by the space shuttle maximum separation weight (approximately 28,100 kg) and two solar thermal designs were compared against competing technologies. The first solar thermal configuration was optimized for a rapid trip time and the second increased the mission duration to reduce the power requirements for the solar concentration system. Data from the Ethridge study, given in Table 2.1, demonstrates the payload advantage solar thermal propulsion gains over chemical systems if slightly longer transfer times are permitted. Additionally, solar thermal systems maintain maneuver durations well below those required by electric propulsion. Ethridge's report concluded that a solar rocket was possible with state-of-the-art technologies and specifically recommended the near term production of an engine/absorber and prototype solar collector for evaluation [4].

Throughout the 1980s, AFRPL oversaw the construction of facilities to evaluate and experimentally test the concepts laid out in Ethridge's seminal report. The AFRPL contracted the Rocketdyne division of what was then Rockewell International to produce a prototype receiver and thruster which was delivered to the AFRPL for testing in 1984 [8]. During the development of

10
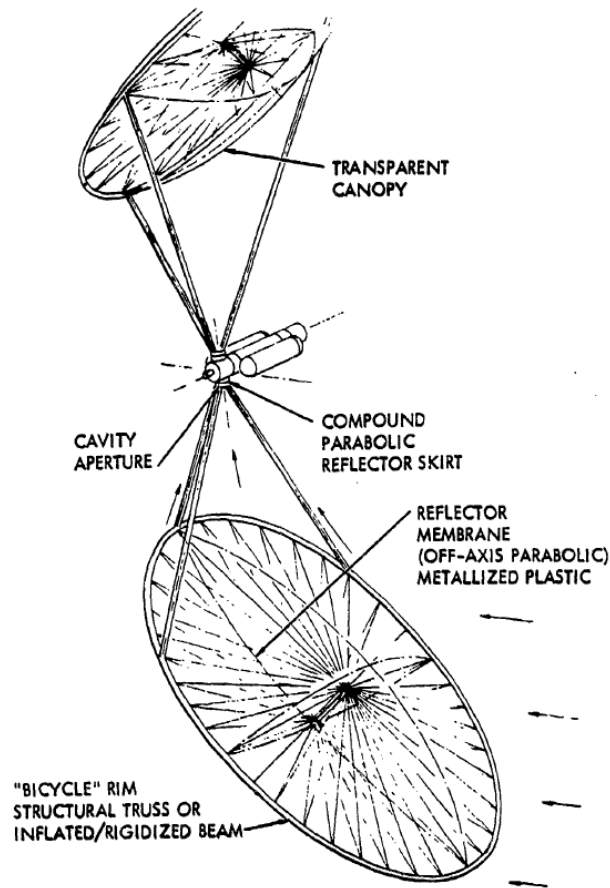
Figure 2.2: Solar thermal spacecraft design proposed in 1979 by AFRPL and Rockwell International. The use of off-axis parabolic reflectors greatly simplified the design of a solar thermal spacecraft by allowing a centrally mounted receiver and eliminating articulated plumbing. Drawing reprinted from Ethridge [4].

the thruster at Rocketdyne, multiple thruster and heat exchanger concepts (shown schematically in Figure 2.3) were considered for both indirect and direct heat absorption techniques. Indirect or windowless concepts used solar radiation to heat a refractory heat exchanger which then transfered heat to a flowing propellant. Direct and windowed concepts included the use of propellant seedants to directly absorb solar radiation and transfer the heat to the propellant stream. Rotating porous beds, vortex traps to retain seedants, and the use of "aerodynamic windows" to pass sunlight directly to the propellant stream were all considered. While direct heating options showed a possible performance benefit and were not limited by heat exchanger material properties, a simple

11
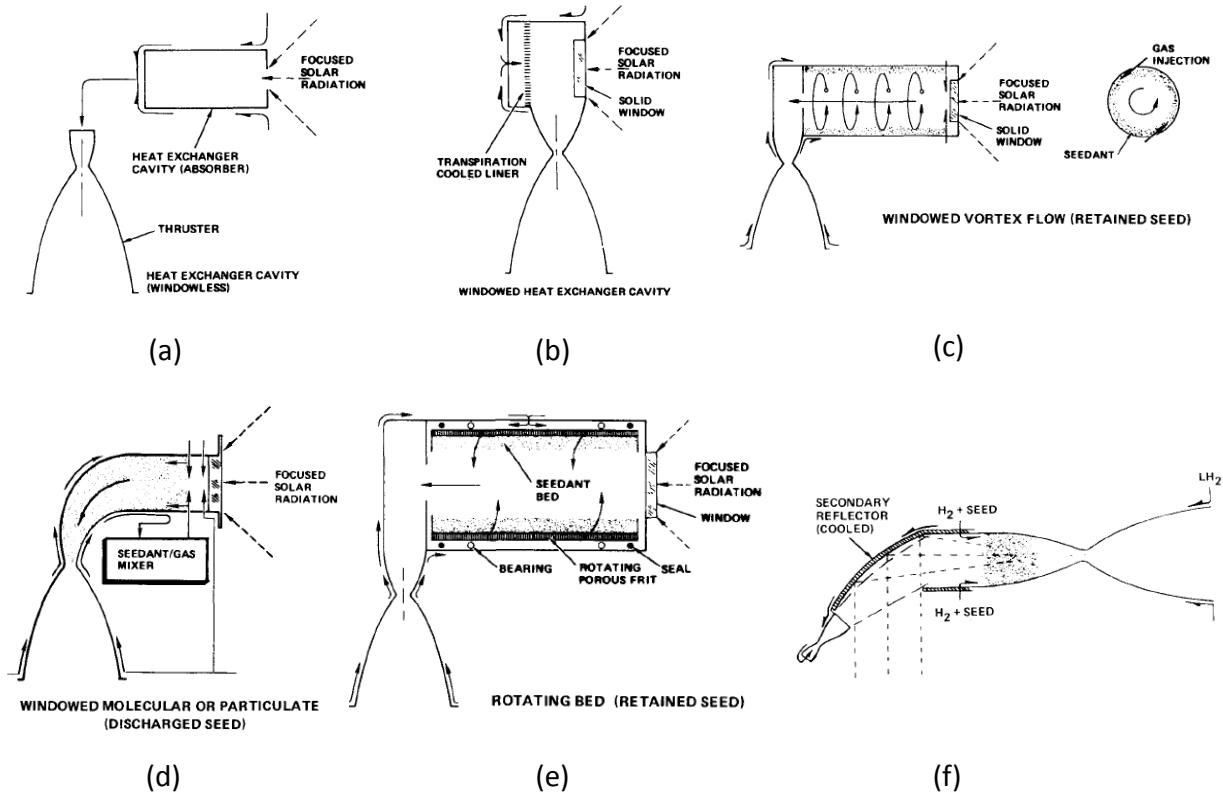
Figure 2.3: Rocketdyne solar receiver concepts. a) Windowless heat exchanger b) Windowed heat exchanger c) Windowed vortex flow exchanger utilizing a vortex flow pattern to retain propellant seedants and preserve I_{sp} d) Windowed particulate concept which discharged seedants in the propellant stream e) Rotating bed concept f) Aerodynamic window proposed to implement a direct heating concept with a simplistic design. Schematics reprinted from Shoji [9].

indirect heat exchanger design was chosen for cost, schedule and risk reasons. The thruster delivered to the AFRPL, shown schematically in Figure 2.4, used a coiled rhenium tube as a combined absorber and heat exchanger. The design targeted an H$_2$ exit temperature of 2705 K, an I_{sp} of approximately 800 s and thrust of 3.7 N.

12
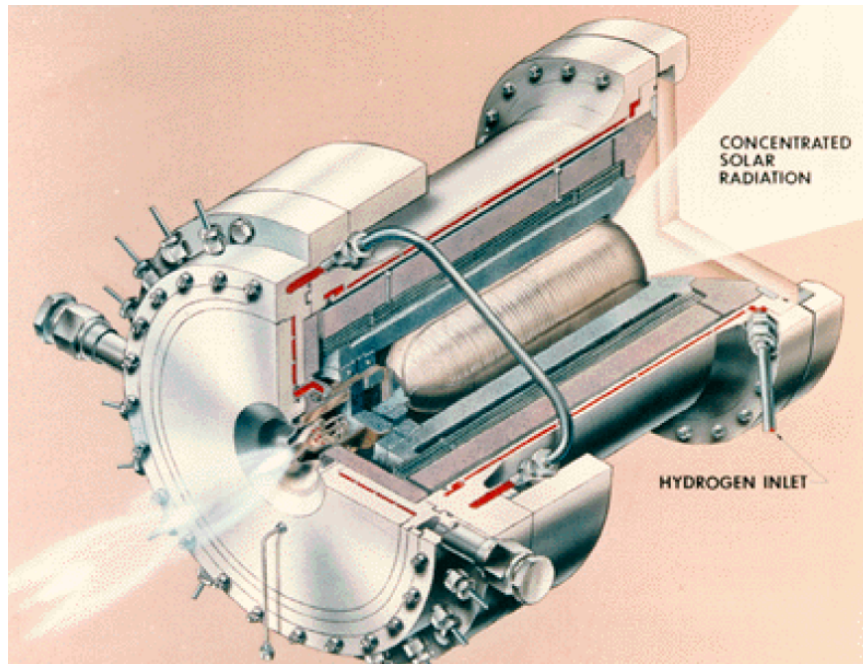
Figure 2.4: Cutaway drawing for the Rockeydyne solar thermal assembly. Originally printed in Shoji [9].

To test the Rocketdyne thruster, the AFRPL was concurrently developing a solar furnace and thrust stand facility. The initial furnace, whose specifications drove the development of the Rocketdyne thruster, proved unsatisfactory upon delivery and a replacement furnace was built based on existing JPL designs. The 25 ft tall, 25 ft wide AFRPL solar concentrator, shown in Figure 2.5, was constructed using over 228 facets and had a design power delivery of 24 kW. During characterization, however, the furnace was only able to deliver 17.5 kW at the focal point - nearly 30% below the input power specification for the delivered Rocketdyne thruster and receiver [10]. Despite the low power level of the AFRPL facility, the Rocketdyne thruster was tested for over 65 hours "on-sun" and achieved H$_2$ temperatures of 1810 K (67% of the target temperature) corresponding to an estimated I_{sp} of 650 s [11].

During the ground test campaign, the AFRPL also investigated various concepts for deployable solar concentrators to address optics, deployability and robustness against space debris and

13
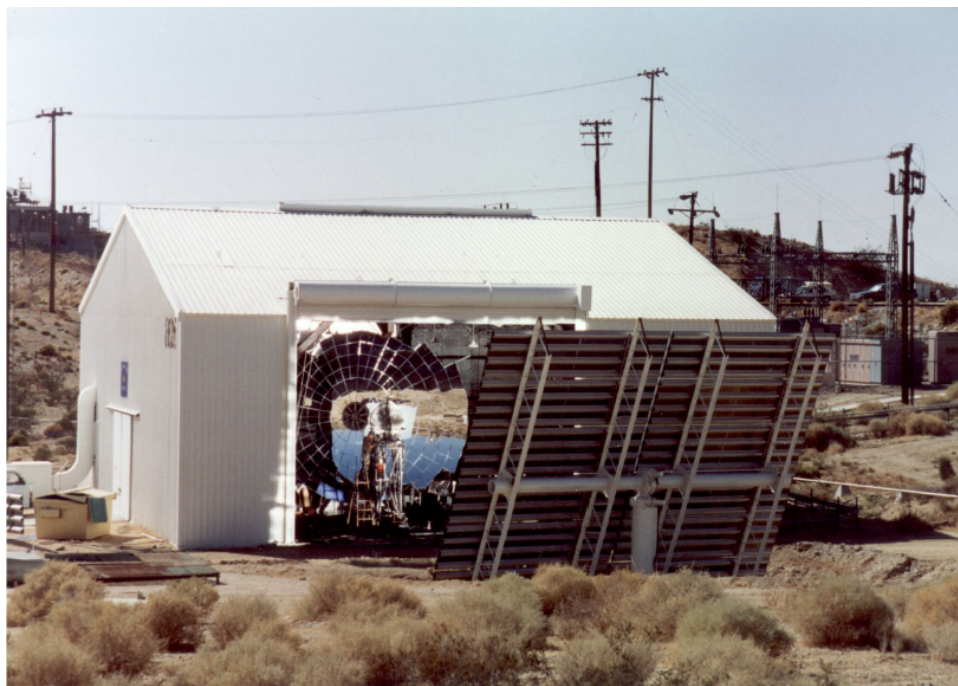
Figure 2.5: AFRPL solar thermal facility circa 1992.

micrometeroid impact. Early in the AFRPL investigation an "electrostatically controlled concentrator" was proposed as a means to prevent concentrator deflation. This technique used embedded electric grids to apply electrostatic forces which maintained concentrator shape and it was demonstrated on a small scale [10]. Following these tests, development focused on designing concentrators using an inflatable toroidal rim to provide primary support. Toroidal concentrator development was successful in producing small scale reflectors capable of sustaining a suitable optic. However, the supporting truss remained in the rudimentary stage at the close of the decade [10].

By 1989, project managers at AFRPL declared solar thermal propulsion a feasible technology and plans were made for a fully integrated systems test in 1994 and an in-space demonstration around 1997. Again, however, solar thermal propulsion faced laboratory budget cuts to the in-house AFRPL program. Smaller projects still continued such as the development of direct absorption thrusters by Rocketdyne using porous disk targets. This effort leveraged existing AFRPL

14

facilities and worked to capitalize on then recent improvements to refractory manufacturing techniques [12]. It was noted during this period that the research funding environment became the limiting factor for solar thermal propulsion and not the state of technological readiness [13].

2.3 Bi-Modal Solar Thermal Propulsion

The next major development in solar thermal propulsion began in the early 1990s as an offshoot of nuclear thermal technology. Nuclear thermal mission designers were considering a novel concept that combined the propulsion and power generation subsystems of a spacecraft into a single integrated system driven by a nuclear thermal energy source. Zubrin et al. proposed a "bi-modal" approach which modified an existing $40\ kWe$ nuclear-thermionic reactor so the core could be used to directly heat hydrogen propellant in addition to providing electric power [14]. This configuration was referred to as the Integrated Power and Propulsion Stage and allowed for similar weight savings as electric propulsion integration while dramatically reducing transfer times due to the relatively high thrust and efficiency of a hydrogen thermal rocket. The USAF Philips Laboratory (previously the AFRPL) outlined a set of performance requirements and investigated various nuclear bi-modal systems suggesting that a bi-modal satellite bus could provide the operational flexibility for the development of new military strategies and significantly reduce operating costs with lower payload weights and increased satellite capabilities [15].

Despite promising technology, nuclear thermal research stalled due to funding cuts, challenges with public perception, high regulatory costs and the difficulty of arranging nuclear ground tests necessary for system validation [13, 14, 16]. As an alternative, BWX Technologies (now Babcock & Wilcox) developed and patented the solar bi-modal concept which leveraged the extensive investment of the previous decade in nuclear thermal propulsion, nuclear thermal power generation and solar thermal propulsion to conceptualize an integrated thermal stage [17, 18]. The proposed solar bi-modal concept shared many technologies with its nuclear thermal counterparts

15

and replaced the nuclear energy source with a central receiver to collect and store concentrated solar energy for both thermionic electric conversion and propellant heating.

The AFRPL conducted a small study as a preliminary investigation into the solar bi-modal concept showing that a bi-modal system held a payload mass advantage over conventional upper stages while maintaining a highly flexible and responsive architecture [17]. More importantly, the AFRPL identified the concept as a means to cheaply improve the economy of current space launch systems during a period of low developmental and project budgets when the existing inventory of launch vehicles were costly and offered limited performance. By drawing on the heritage of previous research efforts, a solar bi-modal upper stage was seen as a way to quickly reduce the cost of USAF space operations using near-term technologies [17].

2.4   Integrated Solar Upper Stage (ISUS) Program

To demonstrate the benefits of a solar bi-modal system (and bi-modal systems in general), the aggressive Integrated Solar Upper Stage (ISUS) program was initiated in 1994. This collaborative project was inspired by the Air Force Space Command's identification of affordability and responsiveness as key operational deficiencies and was managed by the AFRPL with support from the Naval Research Laboratory, Idaho National Laboratory, NASA Lewis Research Center, and various defense contractors. Little existing research effort was targeting the modernization of upper stages and ISUS was presented as an easily accessible breakthrough technology [16, 19].

The ISUS program's primary focus was launch vehicle "stepdown" which would allow smaller, yet similarly capable payloads to be launched into medium earth orbit (MEO), GEO and highly elliptical orbits from smaller launch vehicles. The baseline mission considered in the early stages of development suggested that a high performance solar bi-modal upper stage would allow a nominal communications satellite, typically launched from a Delta II/7925 ($50M per launch in 1995), to be "stepped down" to launch on a Titan IIG ($18-30M per launch in 1995) [16]. The idea of a stepdown was made possible by a paradigm shift in upper stage design brought forth by the

16

bi-modal concept. The orbit raising stage was typically seen as disposable, but the ISUS stage would be integrated with the payload and used to provide power and propulsion to the spacecraft throughout its lifetime.

The goals for the ISUS program called for relevant ground testing and development of ISUS subsystems in the next two years and the flight demonstration of a militarily useful communications payload on an approximately 2000 kg satellite in a 12 hour Molniya orbit by early 1998 [3]. These targets ultimately proved to be overly optimistic. However, the ISUS project did succeed in providing a usable framework for future bi-modal development.

ISUS systems development targeted three primary areas of concern: the receiver-absorber-converter (RAC), the hydrogen propellant feed system and the thermionic conversion subsystem. Despite being able to draw heavily on both solar thermal and nuclear thermal research from the previous decade, these technological areas still required experimental validation before launch. Rigid, faceted solar concentrators similar to those developed for previous space based dynamic power systems were selected early in the program as a way to reduce overall programmatic risk at the cost of performance when compared to inflatables [3, 20].

The most compelling result of the ISUS program, with respect to the contents of this paper, is the development and ground testing of a prototype RAC. The ISUS RAC unit, diagrammed in Figure 2.6, was the first solar thermal concept to utilize a thermal energy storage (TES) material to absorb and store concentrated sunlight. While the addition of TES to solar thermal propulsion had been previously mentioned in the literature, it was not seen as essential to solar thermal technology and was not thoroughly explored. Ethridge's study postulated that the addition of TES would simply reduce transfer times by allowing thrust during eclipse for non-impulsive burns [4]. Shoji suggested that TES would allow for reduced concentrator size by allowing for "charging" of a solar thermal engine during coast periods, however, only considering the reduction in concentrator size resulted in a net mass increase from the addition of TES and the concept was abandoned [11].

17

Solar Collection

Primary concentrated sunlight enters through a Secondary Connector

Solar energy is absorbed at the RAC cavity walls

Graphite thermal storage heats as the sunlight is absorbed

Propulsion
Propellant enters a preheater through an inlet line

Power
Thermionic converters produce electricity as heat from the RAC passes through them. Waste heat is radiated to space by heat pipes.

A layer of insulation reduces heat leakage from the RAC

The propellant heating is completed in the RAC body

Hot propellant gathers in the outlet plenum and then passes to the thruster where it expands and exhausts.

Figure 2.6: Subsystem diagram of the ISUS RAC unit. Figure reprinted from Partch and Frye [21].

The inclusion of TES in the ISUS RAC design provided propulsive benefits and reduced concentrator size. However, the primary reason for inclusion was to provide constant electrical output supporting the bi-modal concept. The ISUS RAC represented a completely thermal spacecraft bus relying on TES as the primary means of energy storage and output.

The heat exchanger and absorber for the ISUS RAC was constructed using 20 kg of graphite and 15 kg of protective rhenium coating. Graphite sensible heat thermal energy storage was selected due to acceptable performance and the absence of previous development towards high temperature latent heat materials. Previous investigations into latent heat thermal energy storage existed from space based dynamic power system development. However, the thermal storage media studied (LiF-CaF$_2$) operated at temperatures too low to be considered for a solar thermal rocket [22]. Graphite sensible heat TES was an existing technology and presented a low enough technical risk to meet the aggressive program goals.

18

A protective rhenium coating was required to suppress graphite reactivity in the hot hydrogen environment and reduce carbon evaporation rates at STP temperatures. Investigations conducted at BWX Technologies indicated that un-protected graphite would lose mass in sufficient quantities to pose a danger to solar concentration surfaces and hydrogen flow integrity [23]. Rhenium was shown to be the most promising coating due to a low vapor pressure, no reaction with hydrogen, a lack of carbide formation, ductility at high temperatures and manufacturability.

In an effort to raise the ISUS system to a technology readiness level (TRL) of 6 and pave the way for flight experiments, the ISUS engine ground demonstration (EGD) used a solar simulator at what is now the NASA Glenn research center. A schematic of the "Tank 6" testing arrangement is given in Figure 2.7. Original testing goals for the EGD were to integrate all aspects of the bi-modal system (H_2 storage and feed, thermionic conversion, power management, space relevant concentrator facets and RAC) into the ground test. However, technical and integration problems resulted in testing only of the RAC hardware [24, 25, 26].

The ISUS EGD program culminated in hot flow hydrogen testing through the prototype RAC and experimentally demonstrated the ability of the proposed heat exchanger to transfer heat from the TES into a flowing hydrogen propellant. Data shown in Figure 2.8 shows how propellant temperature (assumed during testing to be approximately the temperature of the exit tube) remained relatively constant during the first seven minutes of the burn and approached the temperature of the RAC receiver cavity.

Hydrogen blowdown testing showed successful thermal coupling, but temperatures remained below program goals. The existing solar concentrator in NASA's Tank 6 facility required upgrades to provide enough power for the ISUS prototype RAC and the upgrades performed during the ISUS project proved insufficient [25]. It was also found that the RAC and multi-layer insulation package suffered from higher heat loss than design models predicted [27]. The EGD program achieved only 56% of the desired hydrogen burns required to simulate the thrust profile of the reference
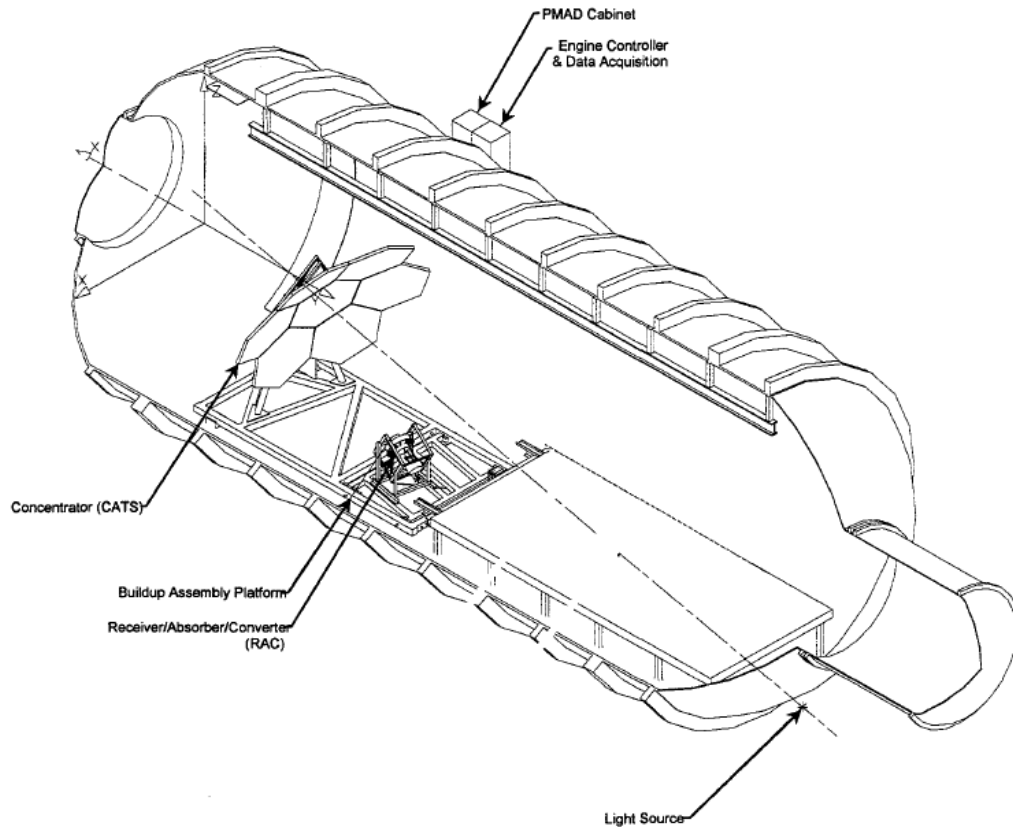
Figure 2.7: Schematic of the ISUS engine ground demonstration (EGD) experiment. Diagram reprinted form Frye and Kudija [25].

flight mission and "on-sun" testing only reached propellant temperatures of 2150 K instead of target temperatures of greater than 2300 K.

While the ISUS EDG succeeded in being the first ground demonstration of a solar thermal system using thermal energy storage, it did not succeed in providing the necessary technological validation to mount the ISUS space demonstration. Excluding follow-on thermionic testing at the New Mexico Energy Conversion Research Lab, the ISUS program was brought to a close in 1998 [26].
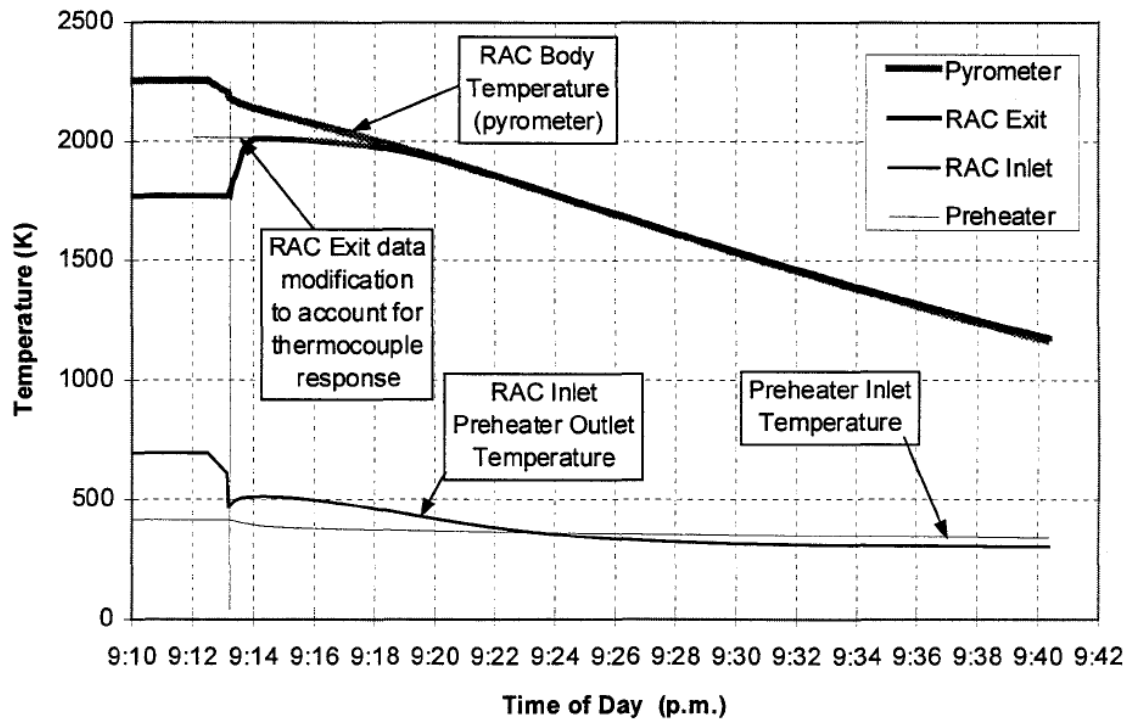
Figure 2.8: ISUS RAC experimental data from hydrogen blowdown testing. RAC exit temperature was measured at the outer surface of the exhaust tube which is assumed to be equivalent to the hydrogen exit temperature. Graph reprinted from Frye and Kudija [25]

2.5 Post-ISUS

In the aftermath of the ISUS program, what is now called the Air Force Research Lab (AFRL) began sponsoring two solar thermal development efforts under two separate divisions [28]. As a direct continuation of the ISUS concept, the AFRL at Kirtland AFB provided Boeing (the then owner of Rocketdyne) with funding to design the Solar Orbit Transfer Vehicle (SOTV) with the intention of performing a flight validation of the bi-modal concept. Concurrently, the AFRL at Edwards AFB, using funding through the Integrated High Payoff Rocket Propulsion Technology Program (IHPRPT), sponsored Thiokol and SRS to perform a proof-of-concept test of an inflatable

21
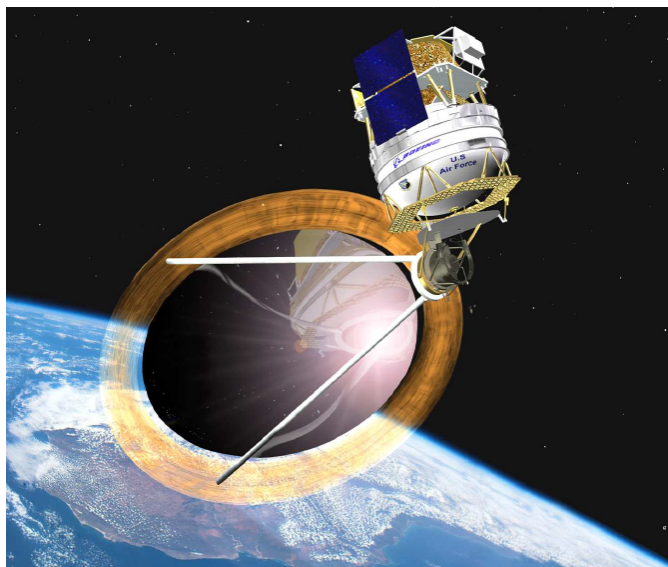
Figure 2.9: Concept rendering of the Boeing/AFRL Solar Orbit Transfer Vehicle (SOTV). Reprinted from Kennedy et al. [27].

solar concentrator known as the STP Critical Flight Experiment (CFE). In 2000, AFRL management merged the two programs and replaced the rigid concentrator designed for the SOTV with the inflatable concentrator under development by the CFE.

The Boeing SOTV, shown configured with the inflatable concentrator in Figure 2.9, was a direct application of ISUS technologies in an effort to demonstrate the potential of solar thermal in space. The smaller spacecraft was based on previous demonstration designs proposed during the ISUS program when funding and scheduling gradually reduced the scope of the ISUS mission [29]. Intended for launch using a Taurus rocket, the SOTV was purely a demonstrator of bi-modal solar thermal technology and would provide the necessary validation of hydrogen propellant handling, solar concentrator performance and control, as well as thermionic conversion under microgravity [30].

The CFE program was a continuation of in-house inflatable development which had been ongoing at Edwards AFB since the mid 1980s. Researchers strove to produce an inflatable concentrator of sufficient optical quality and to also develop a functional pointing mechanism. SRS and Thiokol

22

Figure 2.10: Flight scale concentrators developed during the CFE program. Reprinted from Holmes [31].

succeeded in producing 2 m x 3 m and 4 m x 6 m inflatable concentrators, seen in Figure 2.10, and tested the control system at the component level [28]. The program was set to culminate with a fully integrated test of the inflatable concentrator, pointing mechanism and a direct gain tungsten engine. However, before these tests were completed, the program exceeded its budget and development was halted. It is important to note that the concentrators produced by the program were considered to be "optical quality" and could have been used in a demonstration mission [31].

Concurrent with developmental efforts funded by the AFRL, NASA Marshall sponsored the Shooting Star Experiment (SSE), which attempted to mount a flight demonstration of a solar thermal engine using a porous heat exchanger and a deployable Fresnel lens-based solar concentrator. This concept of a porous direct gain heat exchanger was investigated in the early 1990s by the Phillips Laboratory and the SSE experiments added rhenium coated graphite foam thermal energy storage [3, 32]. The use of thermal energy storage allowed for significant thrust levels within the power confines of a Fresnel lens based concentrator. This system was tested using electric heaters

23
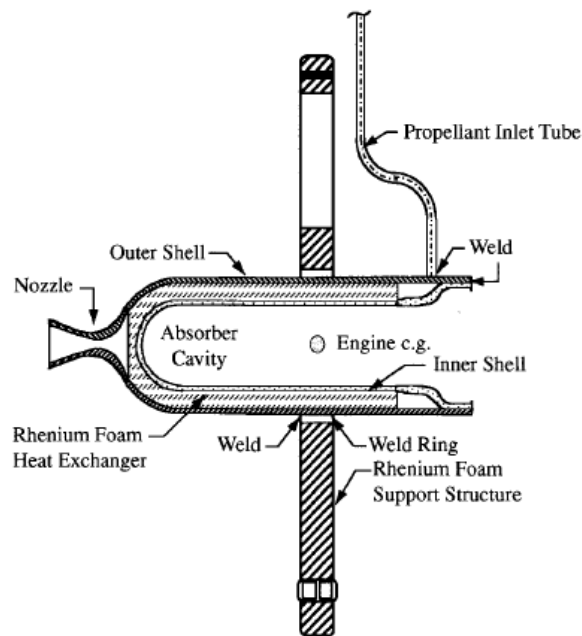
Figure 2.11: Cutaway diagram of the Shooting Star Experiment (SSE) hardware showing the location of the rhenium foam heat exchanger and thermal energy storage. Reprinted from Tucker and Salvail [32].

and was demonstrated "on-sun" at the NASA Marshall Solar Thermal Test Facility showing that a rhenium foam provided a highly efficient heat exchanger configuration [33]. Despite significant progress, funding for further testing and mounting a flight experiment did not materialize and the project was closed.

The SOTV/CFE and SSE programs marked the end of large scale solar thermal demonstration development. Much as Ethridge had defined the scope of solar thermal development through the 1980s, the ISUS program and bi-modal development was the primary driver throughout the 1990s. In the early 2000s, the solar thermal concept became the focus of smaller investigations which attempted to miniaturize the concept and apply it to microsatellites in the hopes of finally mounting an STP space experiment.

24

<div style="text-align: right">

Chapter 3

</div>

Bi-Modal Solar Thermal Propulsion for Microsatellites

After the ISUS program, solar thermal development shifted towards smaller projects targeting low-cost flight demonstration on a microsatellite platform. The concept of a solar thermal microsatellite was investigated at the Surrey Space Center (SCC) and their work defined both the potential performance and the general spacecraft architecture. Based on the results of the SCC effort, the Air Force Research Laboratory proposed that solar thermal propulsion was a promising candidate for a high performance microsatellite [1]. Additionally, it was suggested that operating in a bi-modal configuration could eliminate some of the operational concerns preventing the launch of previous flight efforts. A review of the technologies required shows that, with the exception of high performance thermal energy storage, the components necessary for mounting a successful bi-modal solar thermal microsatellite exist within the current technology.

3.1   Solar Thermal Microsatellite Development

The ISUS program and subsequent follow-on efforts explored the utility of solar thermal propulsion in small satellite packages (200-400 kg) but failed to mount a flight demonstration. Kennedy,

<div style="text-align: right">

25

</div>

who had previously worked on the ISUS program, proposed in the year 2000, that microsatellites (10-100 kg) were an overlooked option for finally providing experimental verification of the solar thermal concept and that a low cost solar thermal pathfinder mission may be feasible [27]. The lack of high ΔV propulsion options for microsatellites made the addition of a solar thermal unit even more compelling. A three year investigation at the Surrey Space Center (SSC) at the University of Surrey sought to analyze the effects of a solar thermal engine on the microsatellite platform and provide the experimental basis for a long awaited in-space experiment.

Microsatellites offer a low cost and relatively rapid development option for mission designers. However, a lack of significant ΔV capability limits their utility. Additionally, microsatellites launch as secondary payloads with sub-optimal orbit insertion requiring hundreds of meters per second of ΔV for correction. Kennedy proposed that a ΔV capability of 1-3 km/s would be an enabling technology and dramatically increase the microsatellite operating envelope. Analysis for multiple candidate missions showed that a robust ΔV would allow for transfer from geosynchronous transfer orbits (GTO) to geosynchronous orbit (GEO) (1,760 km/s), near earth escape (700-1,770 km/s) and insertion into lunar orbits (2,103 km/s) [3]. Preliminary analysis showed that this ΔV target was well within the capabilities of a microsatellite scaled solar thermal propulsion system with $< 50 \%$ propellant mass fraction [34].

Previous solar thermal concepts hoped to optimize I_{sp} by using hydrogen propellant, but microsatellite weight and volume constraints preclude the use of cryogens. As an alternative, Kennedy proposed the use of either hydrazine (N_2H_4) or ammonia (NH_3) which both have a high storage density, low molecular weight and a theoretical I_{sp} of approximately 400 s [34]. Assuming that the theoretical performance can be achieved, Kennedy showed that STP gained an advantage in both volume and efficiency over currently available microsatellite scaled chemical propulsion systems. A comparison was also made against electric propulsion systems which theoretically offer very large ΔV capabilities (> 10 km/s). However, the low power levels available from a

26

microsatellite platform would result in extremely low thrust levels and maneuver durations would be measured in years rather than days.

After completing initial mission and systems analysis, work at SSC focused on experimental design of a reusable solar thermal receiver to demonstrate feasibility. Limitations on concentrator size and system complexity for a microsatellite platform necessitated the use of a pulsed solar thermal rocket relying on sensible heat thermal energy storage (TES). The TES system consisted of a packed bed heat exchanger using pellets of boron carbide (B_4C). The volumetric heat transfer benefits of a packed bed concentrator and resistance to thermal shock and expansion stresses outweighed the disadvantages of a high pressure drop across the heat exchanger and the potential for propellant "channeling" [3]. B_4C was selected since it has an approximately 20% specific heat advantage over graphite. However, reactivity concerns with the hot propellant stream required that the B_4C particles be coated with a protective layer of BN. A schematic of the target design is given in Figure 3.1 showing a rigid fixed concentrator and self contained receiver, thermal energy storage unit and thruster positioned at the focal point. This architecture intended to use the attitude control of the spacecraft to position the solar concentrators for "thermal charging" maneuvers.

SSC produced two prototype receiver units with the purpose of evaluating material compatibility and sealing methods; the Mk I unit was consistent with the notional design and included thermal storage elements. The Mk II unit was a scaled down spiral channel flow design that removed thermal energy storage in order to reach higher overall system temperatures. Both test sections were heated under vacuum using a central graphite resistive heating element in lieu of solar energy input and multiple hot flow tests were conducted using ammonia propellant. The core material for both the Mk I and Mk II receivers was a TiB_2/BN intermetallic composite and it was determined that flanged seals using graphite foil gaskets were the most promising construction option. While the presence of graphite foil seals presented reactivity concerns, the small graphite surface area limited reaction rates with the incoming propellant stream to manageable levels [3].

27
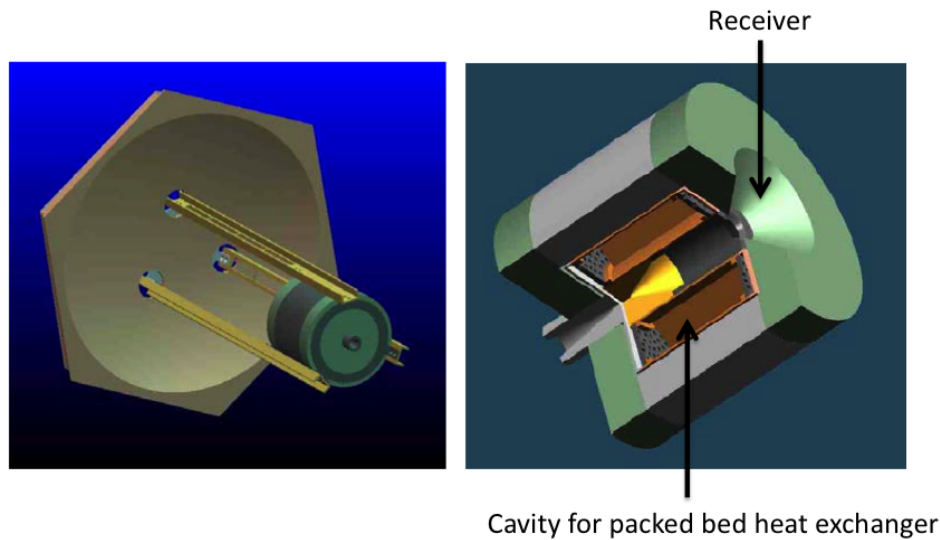
Figure 3.1: Rendering of the notional SCC solar thermal propulsion system with an integrated rigid concentrator. Images taken from Kennedy [3].

The Mk I and Mk II receivers were both heated without propellant to temperatures approaching 1600 K and 2000 K respectively and showed little damage apart from the precipitation of boron oxide binder on the surfaces of TiB$_2$ sections. However, during hot flow tests as chamber pressures approached 140 psi, cracks formed in both test articles presumably due to stress concentrations at ceramic thread locations.

The Mk II receiver was tested using ammonia propellant on a coarse resolution thrust stand and demonstrated thrust levels in excess of 500 mN at an I_{sp} of 237 s. Lower than predicted efficiencies were attributed to propellant leakage at the highest testing temperatures due to loss of seal integrity stemming from thermal expansion [34]. When experimental testing was completed, it was suggested that the majority of testing issues arose from the improper engineering of ceramic structures and that there were "ready" solutions for outstanding sealing problems [27].

Possible candidate missions for flight testing as secondary payload would necessitate a more complicated system than the notional design tested during the ground campaign at SSC. Missions

28
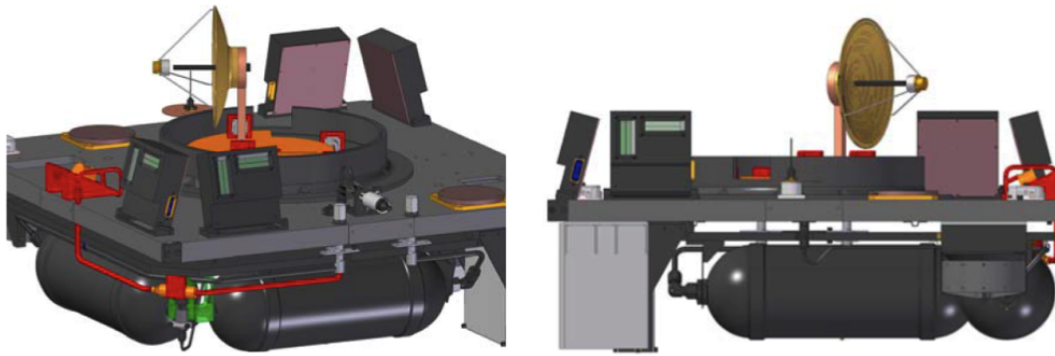
Figure 3.2: Rendering of a microscale solar thermal deorbiting unit for a Disaster Monitoring Constellation (DMC) spacecraft. The single mirror is sized to fit within the the DMC separation ring and is fiber-optically coupled. Figures taken from Kennedy [3].

such as a proposed proof of concept de-orbiting unit on a Disaster Monitoring Constellation (DMC) satellite must address packaging concerns, sun facing surface area and pointing accuracy available on a non-purpose built spacecraft bus. Kennedy suggested the possibility of a 75 W solar thermal system on board the DMC spacecraft with a 112 m/s ΔV capability. The propulsion unit, shown in Figure 3.2, would be capable of lowering the DMC spacecraft into a safely decaying orbit in approximately 13 days using a series of apogee burns [3].

In addition to experimentally demonstrating the base feasibility of a microscale solar thermal receiver, work at SSC evaluated the capabilities of diamond turned aluminum and formed PMA solar concentrators coupled with fiber optic power transmission. Fiber optic development at SSC continued through 2006 and focused on the solar tracking and receiver cavity designs required to mount a feasible system [35]. It was found that utilizing multiple smaller concentrators save weight at the cost of increasing system complexity. Each smaller solar concentrator requires its own tracking system and a low weight, low complexity tracking unit was proposed to provide pointing accuracy on the order of 0.05°. The proposed mechanism was called Fiber Optic Image Position Determination (FIPD) and was designed to assume tracking control for each mirror assembly after the spacecraft bus provides an initial rough alignment. In this system, the target for each

29

solar concentrator is a bundle of optical fibers. Each fiber has an externally mounted photodiode to measure the photoluminesence of the fiber and give a relative intensity measurement. By comparing these relative intensity measurements, the location of the solar image on the fiber bundle can be determined and the tracking mount can be moved in a closed loop system. As a result, a notional system was designed and the locating ability of the fiber optic bundle was proven. However, only rudimentary tests were performed with the integrated tracking system [36].

As with solar thermal efforts before it, the work at SSC did not result in a flight test of solar thermal hardware. The expense, risk, and rise in operational complexity associated with the addition of the solar thermal propulsion unit to an existing satellite prevented the inclusion on any upcoming missions. Despite this, the SSC effort did succeed in identifying the microsatellite as a promising candidate for solar thermal development and proposed STP as a solution for the demonstrated need for high ΔV capability on the microsatellite platform.

In parallel with work at SSC, two smaller efforts also investigated the possibility of microsatellite scale solar thermal propulsion. A group at the Physical Sciences Inc (PSI) headed by Nakamura and funded through the AFRL in the aftermath of the SOTV program performed an experimental investigation into fiber optic power coupling. Unlike Kennedy's investigation which looked at power transfers of less than 5 W, Nakamura demonstrated power transfer of up to 200 W and achieved fiber optically heated receiver temperatures in excess of 1400 K [37]. The work at PSI made use of experimental hardware previously developed for in-situ lunar material processing experiments and showed promise as a means of directly delivering heat to the core of a STP receiver. Along with experimental results, Nakamura also published useful sizing metrics to estimate the total concentrator and fiber optic weights for a 1 N thruster using either H_2 or NH_3 propellant. Using rigid concentrators, Nakamura estimated that combined concentrator and fiber optic weights for an NH_3 system would be 9.46 kg for an on-axis configuration and 8.43 kg for an off-axis configuration. Both of these designs are shown schematically in Figure 3.3.
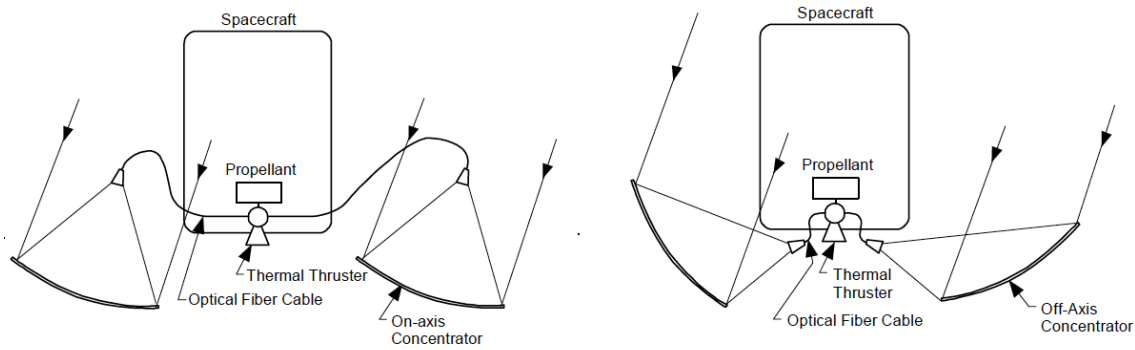
Figure 3.3: On-axis (left) and off-axis (right) fiber optic solar thermal configurations diagrams re-printed from Nakamura et al. [37].

Outside of the United States, the Advanced Space Technology Research Group at JAXA also targeted solar thermal as the "most promising" propulsion design for an orbit transfer vehicle [38]. Their research focused on the development of lightweight solar concentrators and the construction of a solar thermal engine out of single crystal refractory metals. The most promising aspect of their work was the creation of thin film polyester and polyamide solar concentrators with area densities as low as 180 g/m^2. These concentrators were vacuum formed at temperature onto paraboloidal glass molds, taking into account forming error, and allowed to set for several days to relax stresses in the material. This effort resulted in reflectors with concentration ratios exceeding 10,000:1 and vibration resistance sufficient for space launch. Additionally, direct gain receivers were experimentally tested on-sun at atmospheric pressures and propellant temperatures of up to 2000 K were recorded. The JAXA effort combined thin film concentrators and the proposed STP engine into a sample de-orbiting module, shown in Figure 3.4, that was intended for flight on board the newly developed 50 kg μ-LabSat bus. However, the experiment never launched.

31
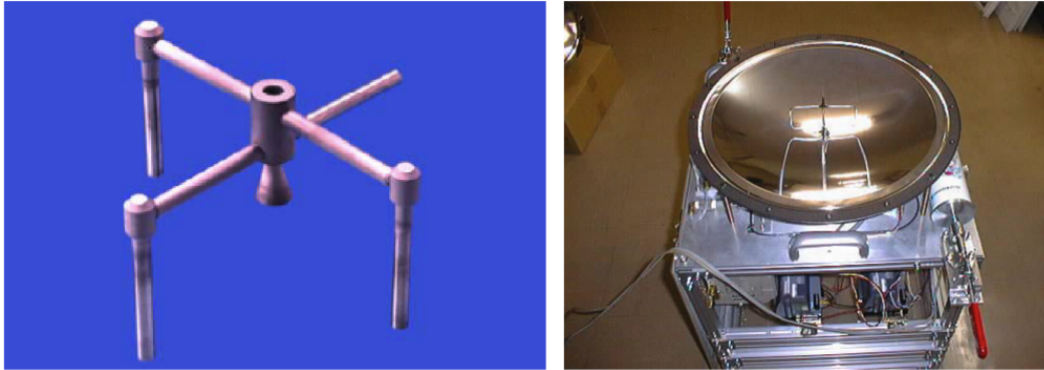
Figure 3.4: Single crystal Mo solar thermal receiver and prototype de-orbiting module with receiver unit mounted centrally inside a thin film solar concentrator. Photographs taken from Sahara et al. [38].

3.2   Bi-Modal Microsatellite Concept

In 2009, the Advanced Propulsion Concepts Group in the AFRL's aerophysics branch published a review of high thrust, high ΔV propulsion options for microsatellites and identified solar thermal propulsion as a promising candidate for high performance missions [1]. The baseline mission for the review was a microsatellite "inspector" that could rapidly be diverted from its existing orbit and rendezvous with another satellite for close proximity operations. Estimates for this mission scenario expected a ΔV requirement of around 1 km/s and an ideal thrust of at least 1 N to ensure rapid mission response. Citing Kennedy's solar thermal microsatellite development effort, the review found that STP offered a compelling combination of efficiency and thrust that could achieve greater ΔV capability than chemical propulsion options with a minimum decrease in responsiveness. It was the recommendation of the authors to pursue further research in what was found to be an enabling technology in "early stage" development [1]. These recommendations proved to be the genesis of this research effort.

Budget issues aside, the historical failure of solar thermal research programs to produce a flight mission stems primarily from the inherent complexity that accompanies mounting a novel propulsion mechanism. Furthermore, the large scale of previous development projects positioned

32

the spacecraft within a design space where the benefits of a solar thermal system did not outweigh the risks to both cost and mission assurance. Large scale STP systems necessitated the use of cryogenic propellants to gain significant advantage over more conventional chemical rockets and the electrical power available on board a large spacecraft bus allows for electric propulsion systems with adequate thrust for conventional mission scenarios.

In contrast, a strong case is made for solar thermal technology on a microsatellite platform. A highly aggressive microsatellite requiring substantial ΔV is currently unable to generate the necessary power for a relatively high thrust electric propulsion system. Additionally, mass and volume limitations require propulsive efficiency beyond what is offered by small scale chemical rockets.

It is proposed that a bi-modal solar thermal microsatellite could serve as a low cost, high performance platform for propulsion intensive mission scenarios. Such a satellite would take the microscale solar thermal concept originally presented by Kennedy and combine it with a means of thermal electric conversion. This would entirely replace the electrical power subsystem (photovoltaics and batteries) of conventional satellites with an entirely thermal-based architecture, effectively reducing complexity. If coupled with a suitable high energy density thermal storage medium, the thermal energy system would function as a conventional satellite bus and provide significant mass savings. Whereas previous small scale solar thermal missions have been viewed as pure demonstrations for the solar thermal concept, the performance benefits of a bi-modal system would create an operational low cost platform within the same mass and volume constraints.

In order to realize a low-cost, high performance microsatellite with rapid deployability, the proposed bi-modal system architecture, illustrated in Figure 3.5, must be designed so that the use of a novel technology has minimal mission impact. Despite higher potential performance, cryogenic propellants have been ruled out due to insulation, pressurant and volume constraints on a microsatellite platform. Instead, ammonia is proposed as the ideal propellant due to ease of storage, acceptable performance and self pressurization to reasonable chamber pressures. While hydrazine

33
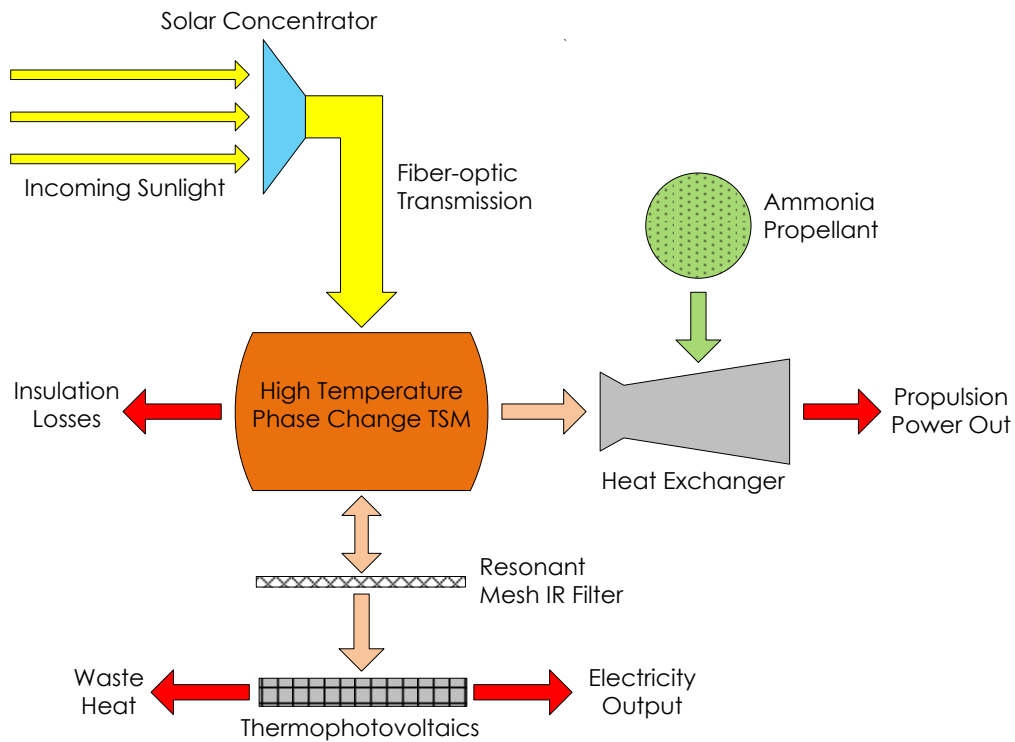
Figure 3.5: Energy flow diagram for a bi-modal solar thermal power system capable of providing both propulsive and electrical power output.

may offer higher performance, the requirements for a pressurant increase system complexity and its toxicity complicates testing and development.

Furthermore, in order to avoid mission impact imposed by the solar concentration system, fiber optics must be used to decouple the solar concentration and solar thermal engine from the spacecraft attitude and sufficient thermal energy storage must be available to provide continuous power to all subsystems despite changing solar flux while in orbit. If these system goals can be realized, a novel, high-performance microsatellite will be enabled.

34

3.3 Technological Requirements

In order to realize a bi-modal solar thermal system at the microsatellite scale, many technological requirements must be met. These include the ability to produce low mass, high performance solar concentration systems, efficient fiber optic power coupling, high specific mass thermal-electric energy conversion, advanced insulation materials and high performance thermal energy storage. Due to the long development history of solar thermal propulsion, the majority of these technologies have already been investigated and many of them have reached technology readiness level (TRL) 5-6.

3.3.1 Solar Concentration

First and foremost, a solar thermal energy system requires high performance solar concentration. The development of solar concentrators for STP has a long history and it appears that concentrator options suitable for microsatellite use are currently available. The work of Sahara et al. at JAXA in particular has experimentally demonstrated sub 200 g/m^2 concentrators with the 10,000:1 concentration ratios required for target temperatures of 2500 K [21, 38, 39]. Since a microsatellite based solar platform would require less than 2 m^2 of total concentrator area, the use of self-supporting thin structures is possible. With the exception of the ISUS program and its heritage in rigid deployable concentrators from the Solar Dynamic Ground Test, the majority of historical concentrator development has focused on the development of inflatable concentrators for large scale satellites [20]. Inflatable structures allow promising packaging possibilities and area densities of < 1 kg/m^2 have been experimentally demonstrated at the surface uniformity required for radio transmission. Published data, however, does not include demonstrations of concentrators with sufficient optical quality required for solar thermal applications as documented RMS slope errors approach 0.5 degrees [3, 36, 40, 41]. Deployable rigid structures proposed by the ISUS program had area densities of 2.5 kg/m^2 which was improved to 1.5 kg/m^2 through changes in manufacturing techniques [25, 42]. These figures are for the mirrored facets themselves and do not include tracking

35

systems, deployment mechanisms or other structures. Harris Corp, the original manufacturer of the ISUS program concentrator array, estimated that these assemblies will add an additional 1.5 kg/m^2 based on large 10 m^2 systems [43]. It is expected that the additional weight estimates would be less dramatic for a micro-scale system. With minimal packaging and support structure, the concentrator's proposed by Sahara et al. can be used as a low mass, high performance system and it is believed that little research effort is required in solar concentrator development beyond packaging for a specific satellite design if inflatable structures are not required.

3.3.2   Fiber Optic Coupling and Pointing Accuracy

The next technological requirement for a bi-modal STP system is fiber optic power transmission and concentrator pointing capability. Fiber optics allow for a de-coupling of solar thermal hardware from spacecraft attitude, which is required if the bi-modal satellite is to be used for anything beyond a technological demonstration. The use of a thermal energy storage design does afford the possibility of using the spacecraft attitude control system to perform "charging" maneuvers before burns. However, the operational impact of multiple re-positioning maneuvers limits the utility of the platform. Work by Nakamura has demonstrated the possibility of fiber optic transmission of concentrated sunlight at the laboratory scale and achieved total system efficiencies (sunlight to fiber exit) of 38% using un-optimized hardware [37]. Nakamura estimates that a realistic space qualified system could raise the total system efficiency to more than 70% by careful engineering and better material selection such as higher reflectivity concentrators and switching to low-OH optical fibers. Henshall's work at SCC also demonstrated a lab scale fiber optic transmission system and showed an end-to-end efficiency of approximately 50% including Cassegrain concentrators [36]. It is believed that the transmission efficiency predictions made by Nakamura are realistic and that there are certainly improvements that can be made to increase end-to-end efficiencies through careful engineering with existing technologies.

It is generally proposed that a pointing accuracy of $0.1°$ will provide acceptable solar concentrator performance on-board a spacecraft and is achievable with current technology [4, 3, 44]. In terms of body pointing capabilities, it is possible to achieve an order of magnitude higher than the required performance as demonstrated by space based observatories such as the Herschel and Plank missions operated by ESA [45]. Microsatellites, such as Surrey Satellite Technology's 165 kg CFESat are currently capable of pointing accuracies on the order of $\pm1°$ and the remaining pointing capability can be made up using commercially available pointing systems and position sensing devices. An example of a commercially available unit is the Type 22 Antenna positioner assembly from Moog which can achieve minimum step sizes of $0.02°$ (noting that the 5 kg system weight could potentially be reduced by re-design to exact specifications) [46]. It should also be noted that work at SSC on Fiber Optic Image Position Determination provides a road map for a low complexity solar tracking solution [36]. There appears to be no fundamental limits to achieving the pointing accuracy required for a solar thermal collection system and careful engineering should yield the required performance.

3.3.3 Thermal-to-Electric Conversion

If the solar concentration system is to be the only source of energy for proposed bi-modal spacecraft, a means of thermal-to-electric energy conversion must be employed. Due to the high temperatures involved in solar thermal propulsion, an effective system must operate with a hot side temperature in excess of 1600 K while retaining a high energy conversion density. If only currently realizable technologies are considered, the conversion options are limited to thermionics (proposed for ISUS), closed brayton systems (proposed for the Solar Dynamic Ground Test) and thermophotovoltaics [47]. Both thermionic conversion and closed brayton systems have strong developmental histories. However, they exhibit poor scaling down to microsatellite power levels [47, 48]. Dynamic systems, in particular, require a condenser stage and the ability to remove sufficient heat from the working fluid is problematic within the confines of a microsatellite [49].

Thus, thermophotovoltaic (TPV) conversion is selected as the most promising candidate for a bi-modal microsatellite. TPV power conversion uses photovoltaic cells that are optimized for IR radiation from a hot radiating body. The key to peak power efficiencies in a TPV system is matching the emission of the radiating body to the peak efficiency wavelengths of the photovoltaic cell.

The use of TPV conversion has seen great improvements in the last two decades. In the early 1990s, work at McDonnell Douglass in partnership with NASA Lewis tested TPV cells coupled with selectively emitting radiating bodies producing experimental cell efficiencies on the order of 30% and solar-to-electric efficiencies specified between 12-20% depending on temperature of the solar receiver [50, 51]. In the early 2000s, EDTEK, with funding from the California Energy Commission, US DoD and the US DoE, investigated thermophotovoltaics as a commercial power generation option when coupled with their patented selective IR filter technology. EDTEK developed what they called a "resonant mesh IR band pass filter:" essentially a gold screen precision etched with a geometric pattern. At the wavelengths of interest, the geometric pattern, coupled with the electrical properties of the material, created a resonant condition in which the sheet functioned as an antenna - absorbing the desired wavelengths on one side and re-emitting them on the other at efficiencies approaching 70% [52]. Wavelengths outside of the desired band gap were reflected back to the radiating body at an efficiency of 98%. Using these resonant mesh filters, EDTEK predicted solar-to-electric efficiencies on the order of 30% with theoretic TPV cell efficiencies approaching 48%. Unfortunately, these numbers were based on extrapolated data from low power experiments as operator error lead to a failure of the advanced testing hardware [52].

In 2000, a review of space power systems by Hyder specified the efficiency of a TPV system to be approximately 19% with a specific power density of 15 W/kg including radiators; this was comparable to the advanced three junction photovoltaic panels of the time [47, 53]. The end-to-end efficiency of thermophotovoltaics are tied to the efficiency limits of advanced photovoltaic cells and there is reason to believe that the specific power density of TPV technology has significant

38

potential for improvement. A parallel is the specific power density growth seen during the same period in conventional photovoltaics. By 2012 the specific power density of PV panels had risen from 15 W/kg in 2001 to 100 W/kg in 2012 and it is believed that similar improvements can be made in TPV system [54].

3.3.4 High Performance Thermal Insulation

The remaining technological requirements for a bi-modal STP system concern the receiver-absorber-converter (RAC) which must receive, store and distribute collected solar energy. The high temperatures needed for solar thermal propulsion require the use of advanced insulation as well as ceramic and refractory construction materials. All materials must be able to operate for sustained periods at temperatures between 1500 - 2600 K and careful consideration is required to avoid adverse material interactions and degradation.

High temperature insulation materials currently exist that can provide acceptable performance at STP temperatures. Table 3.1 lists candidate insulation materials and relevant properties. A notable example with a long development history is carbon bonded carbon fiber (CBCF), which was developed as insulation for NASA RTG projects [55, 56]. Other carbon based insulation such as carbon foams and rigid networks of carbon fibers can achieve similar or better performance and multiple ceramics are available with moderate performance but comparatively high density [57]. A new type of refractory and ceramic doped aerogel is also currently under investigation at the AFRL in conjunction with this research effort.

In addition to solid insulation materials, the use of multi-foil insulation is common in high temperature applications and low emissivity vacuum gaps are critical to TPV systems [52, 55]. An appropriate insulation system will combine radiation shielding, vacuum gaps and solid insulation to ensure minimal heat loss. Special attention must also be paid to material compatibility and reactivity. However, a workable solution is certainly achievable with the existing state of the art.

39

Table 3.1: Potential high temperature insulation materials. Thermal conductivity values given in italics are interpolated from available data.

Material	k_{th} @ 1000 $°C$ [W/mK]	k_{th} @ 1500 $°C$ [W/mK]	k_{th} @ 2000 $°C$ [W/mK]	Density [g/cm^3]	Reference
Silicon Carbide	45	30	*25*	3.2	[58]
Boron Nitride	17-33	22.5	*18*	1.8	[59, 60]
Alumina	6.5	6.6	–	3.8	[59]
1-D Vacuum Gap	1.5	3.8	7.7	–	[61]
Zirconia	2	2.5	*3*	5.5	[59]
Rescor 760	0.93	*1.2*	*1.4*	4	[62]
ONRL CBCF	0.17	0.2	0.26	0.2	[55]
Calcarb CBCF	0.2	0.35	0.65	0.18	[63]
Aerogel Filled Graphite Foam	0.25	0.4	0.75	0.07	[64]
Mo / Zr0$_2$ Multifoil	0.001	0.05	0.1	1.4	[55, 65]

3.3.5   Thermal Energy Storage Material

The selection of a thermal energy storage (TES) material/method is the final technology requirement and drives the overall bi-modal system architecture. The TES material is fundamental to the overall RAC design since the RAC structure must be compatible at storage temperatures and incorporate a suitable method of heat exchange with the propellant stream. The primary factors which drive TES selection are desired operating temperature range, energy storage density, thermal conductivity, reactivity, and whether sensible or latent heat is the primary means of energy storage. To date, all solar thermal designs using a TES approach have relied on sensible heat with either graphite or boron carbide as the TES material [3, 25, 49].

In the case of the ISUS program, the ground demonstration assembly utilized what was essentially a graphite cylinder as the TES medium. The RAC assembly was designed so that the center of the cylinder acted as a blackbody cavity for absorbing solar radiation and 195 3 mm diameter channels were bored through the cylinder wall to act as heat exchanger passages for the propellant stream [66]. A photograph of this graphite assembly, showing the central cylinder and plenumn caps is given in Figure 3.6. In order to survive the hot hydrogen testing environment, the entire

40
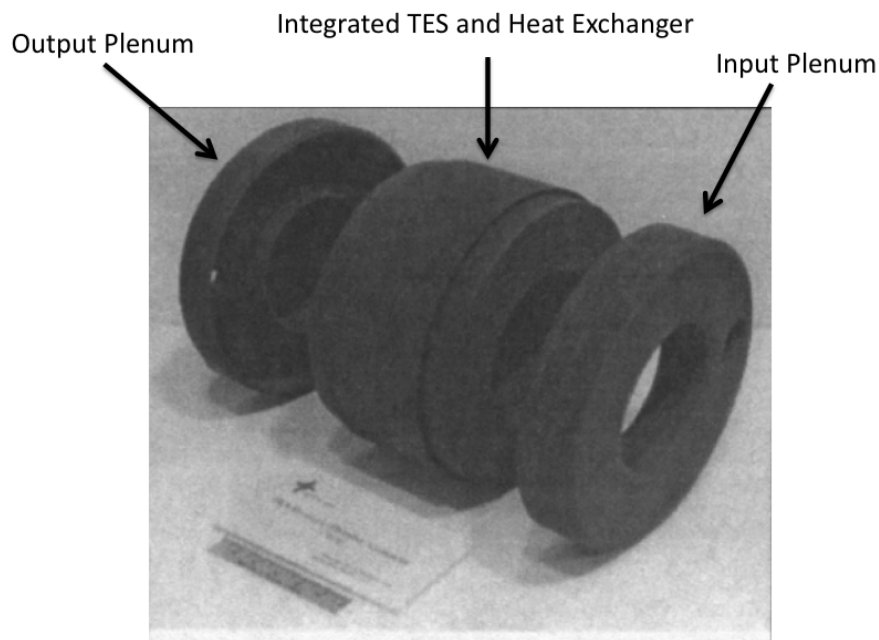
Figure 3.6: Photograph of the uncoated graphite components for the ISUS RAC showing the central combined heat exchanger and TESM. Reprinted from Miles [23].

assembly was coated with rhenium, resulting in total mass values of 15 kg of rhenium and 20 kg of graphite TES [25]. The protective rhenium coating provided satisfactory performance during coupon testing. However, there were remaining difficulties with graphite sublimation sustained through the rhenium coating at temperature [23].

The decision to utilize graphite for the ISUS program, and sensible heat in general, was a function of developmental time constraints and the low TRL level of other TES options. Table 3.2 lists the specific heat of multiple sensible heat storage materials and it can be seen that a significant operating temperature range is required to reach appreciable storage densities. It is for this reason that sensible heat thermal energy storage systems are described in the literature as having "moderate yet acceptable" performance [34].

41

Table 3.2: High temperature sensible heat materials [67, 68].

Material	T_{melt} [K]	C_p @ 2500 K [kJ/kgK]	ΔT required for 1 MJ/kg
Graphite	3923	2.15	475
B$_4$C	2700	2.68	380
Silicon Carbide	2818	1.01	740
Boron Nitride	3273	1.98	510

Published experimental data from the ISUS program allows for an evaluation of a sensible heat storage system during hot flow testing. Figure 2.8 gives the results for the ISUS RAC at a hydrogen feed rate of 1.7 g/s and it can be seen that the system produces an approximately steady state propellant exit temperature for the first seven minutes of the burn. After this, both the TES medium and the propellant temperatures drop rapidly. The ISUS RAC is able to maintain a steady exit temperature because the propellant flowing through the RAC reaches thermal equilibrium with the graphite TES before exiting the heat exchanger. As the entrance region of the graphite TES transfers energy to the propellant and cools, the point at which the propellant reaches equilibrium moves further forward within the TES medium. As long as "hot" thermal energy storage exists beyond this equilibrium point, the propellant maintains a steady exit temperature. Once the propellant begins to draw heat from the RAC across the entire length of the heat exchanger, the exit temperature begins to fall with the overall drop in RAC temperature.

When the ISUS RAC unit reaches an effective energy storage density of 1 MJ/kg approximately 15 minutes into the burn, the propellant exit temperature has dropped to under 75% of the peak value corresponding to a 15% drop in I_{sp}. Since I_{sp} varies with the square root of temperature, the ISUS graphite system is able to maintain the stated "adequate" thermal rocket performance and only particularly long burns will suffer from reduced efficiency.

While the large temperature swing of a sensible heat TES system has a relatively low impact on propulsive efficiency, the effects on thermal electric conversion in a bi-modal configuration are profound. The original specification for the ISUS system allows for converter temperatures between 1900-2200 K at the thermionic converter hot shoe [23]. This 300 K temperature range

42

would prove unacceptable on a microsatellite bi-modal platform relying on radiatively coupled thermophotovoltaics. Based on published data for the EDTEK 1400 nm selective emitter system and GaSb TPV cells, a temperature drop from 2200 K to 1900 K at the emitter (assumed to be black body) will result in an over 50% drop in power output [52]. To maintain steady electrical power on the spacecraft despite fluctuating emitter temperatures, additional weight in the form of batteries or additional TPV units will be required.

Within the constraints of a TPV based bi-modal microsatellite platform, the additional mass and operational inefficiencies of using a sensible heat thermal energy storage system renders it impractical. Therefore, it is proposed that the final technological requirement for a high performance bi-modal microsatellite is adoption of latent heat thermal energy storage. Latent heat storage materials offer both higher energy storage densities and a relatively constant energy output temperature corresponding to the melting point of the storage material. Unlike the technologies discussed previously in this section, there is very limited research into the use of latent heat materials at STP temperatures and there have been no direct experimental efforts. The development of an effective latent heat thermal energy storage system is presented here as the final technological hurdle that must be overcome to realize a high performance bi-modal solar thermal microsatellite platform.

High Temperature Latent Heat Thermal Energy Storage

Many of the technological requirements for a solar thermal bi-modal satellite have been previously investigated and feasible solutions appear to be readily available. However, the transition from using sensible heat thermal energy storage to a high performance latent heat system requires an extensive research effort. Existing latent heat thermal energy storage research is chiefly concerned with terrestrial applications and targets temperatures well below those required by a solar thermal system. To reach temperatures suitable for spacecraft use, a new class of high temperature latent heat storage materials must be identified and developed.

4.1   Phase Change Material Selection

Latent heat thermal energy storage utilizes the heat of fusion released during a phase transition (typically liquid to solid) as the primary energy storage mechanism. Extensive research has been performed for terrestrial application of latent heat materials and thousands of potential materials have been evaluated. Existing latent heat materials can be divided into three broad categories: paraffin waxes, fatty acids and hydrated salts [69]. These materials, whose properties are listed in

44

Table 4.1: Relevant properties of typical phase change materials [69, 70].

Class	T_{melt} [K]	ΔH_{fus} [kJ/kg]	k_{th} [W/mK]
Paraffin Waxes	317-379	72-214	0.19-0.75
Fatty Acids	268-344	45-210	0.14-0.17
Hydrated Salts	281-1170	115-492	0.46-5.0

Table 4.1, have melting temperatures far below what is required for STP as well as thermal conductivities and energy storage densities an order of magnitude below what is necessary. Even some of the highest temperature phase change materials under consideration, such as potassium carbonate, have melting temperatures only slightly above 1100 K and heats of fusion below 500 kJ/kg [70]. Furthermore, many of these materials suffer degradation after multiple thermal cycles. In order to apply latent heat thermal energy storage to a solar thermal bi-modal system, a new class of materials is required.

In the search for a new high temperature latent heat storage material, the primary considerations were the melting (operating) temperature and energy storage density. The melting temperature of the material defines the peak propellant temperature and thus the performance of the solar thermal rocket. For the bi-modal microsatellite proposed, ammonia propellant has been selected due to ease of handling and reasonable performance. Literature indicates that the optimal temperature for an ammonia rocket is around 2500 K which results in an I_{sp} in excess of 400 s dependent on the degree of ammonia dissociation in the system [35, 37, 39]. At lower exhaust temperatures around 1500 K, an ammonia rocket is still capable of achieving approximately 300 s I_{sp}, which is beyond what microsatellite scale monopropellant thrusters can provide. Using this temperature range as a guide, the potential phase change materials given in Table 4.2 were identified.

Silicon and boron have been selected as target high temperature phase change materials due to their exceptionally high heats of fusion, and melting temperatures that are ideally matched for use in an ammonia solar thermal rocket. Additionally, these materials are elemental, removing

45

Table 4.2: Potential high temperature phase change materials. Material specific references are given when applicable, otherwise, values are taken from [59, 67, 71]. Thermal conductivity values given in italics are the closest available measurement to T_{melt}.

Material	T_{melt} [K]	ΔH^o_{fus} [kJ/kg]	k_{th} @ T_{melt} [W/mK]
MgF$_2$ [72]	1536	940	3.8
Beryllium	1560	1312	*69*
Silicon [73]	1687	1785	20
Nickel	1728	292	*83*
Scandium	1814	313	*16*
Chromium	2180	394	48
Vanadium	2183	448	*51*
Boron	2350[1]	4600	*5-10*
Ruthenium	2607	381	*80*
Niobium	2750	290	*82*
Molybdenum	2896	375	*84*

concerns of material breakdown, and both exhibit adequate thermal conductivities. Both silicon and boron are considered in this work with silicon treated as a near term, moderate performance solution and boron being the ideal long term target.

4.2 Technological Comparison

The use of latent heat thermal energy storage appears immediately beneficial when comparing material properties. However, operational concerns and the effects of implementing this technology within spacecraft parameters must be considered. Switching to a latent heat medium is a significant technological undertaking and the benefits must be strong enough to support the needed development. Two technological comparisons have been made to demonstrate the benefits of switching to latent heat thermal energy storage. The first comparison considers the advantages

---

[1]The melting temperature given is for β-rhombohedral boron. Some sources list the melting temperature as 2573 K corresponding to amorphous boron, however, the phase change process will occur at the β-rhombohedral temperature [74, 75]. Sands and Hoard write that from the liquid state, boron will re-crystallize into the β-rhombohedral form and a later work notes that the α-rhombohedral form will irreversibly become β-rhombohedral at approximately 1773 K [76, 77].

46

of integrating latent heat thermal energy storage into an existing sensible heat based bi-modal design. The second comparison, performed in conjunction with the AFRL, proposes the performance impact of a boilerplate bi-modal solar thermal propulsion system on a microsatellite platform vs. competing conventional configurations.

4.2.1 Latent Heat Application to Existing Designs

A logical starting point for the analysis of latent heat thermal energy storage is to apply the technology to the heat exchanger designed for the Integrated Solar Upper Stage Program. The ISUS program is the most fully realized bi-modal solar thermal design to-date and even with sensible heat thermal energy storage it provided acceptable performance. However, if the sensible heat thermal energy storage (TES) were replaced with boron, the TES package could potentially see an almost fourfold increase in total energy storage density (versus the designed graphite ΔT of $600K$). It is also expected that a latent heat energy storage system will offer convective coupling advantages resulting in a more stable propellant output temperature during the course of a burn.

Since these assumptions are based purely on material properties, analysis is required to address the operational concerns of applying a latent heat thermal energy storage medium. Chief amongst these concerns is the ability of a latent heat medium to effectively transfer energy into propellant due to the relatively low thermal conductivity of solid high temperature PCMs near their melting point. A series of conjugate heat transfer models have been completed using the commercial multiphysics package STAR-CCM+ to quantify the effects of an ISUS like design using latent heat thermal energy storage

ISUS Approximation

In order to efficiently model the ISUS system, the heat exchanger at the core of the receiver-absorber-converter was modeled a single representative adiabatic heat exchanger passage. Published specifications for the ISUS RAC state that the assembly was manufactured from three parts:

47

two plenum end caps and a central graphite cylinder. This central graphite ring, shown in Figure 3.6, is the primary heat exchanger. The graphite ring is approximately 152 mm long with an inner diameter of 140 mm and an outer diameter of 300 mm. The graphite heat exchanger contained 195 flow passages with a diameter of 3 mm and was coated with 0.3 - 2.5 mm of CVD rhenium depending on location. From these values, it was calculated that the heat exchanger core contains approximately 15 kg of graphite and 10.1 kg of rhenium thermal energy storage.

For the STAR-CCM+ model, the macro properties of this central heat exchanger were divided by the total number of heat exchanger passages and the result was assigned to a single 152 mm long heat exchanger channel. The resulting model geometry, shown in Figure 4.1, consists of a 19.6 mm outer diameter, 3 mm inner diameter passage containing 129 g of total thermal energy storage mass. The inner surface of the package is coated with a 0.25 mm rhenium layer consistent with published coating values and the graphite bulk geometry was selected to evenly distribute the full design's 15 kg of graphite TES between 195 channels. Similarly, the outer surface of the channel is coated with an additional 0.22 mm layer of rhenium to account for the remaining CVD rhenium specified in the original system. Note that this geometry is an approximation due to the uneven distribution of the propellant channels in the ISUS design. However, results for this geometry demonstrate similar behavior as the macro system.

Solid properties were modeled as being fully temperature dependent and graphite properties were kept consistent with the TM grade POCO graphite used in the ISUS experiments. Hydrogen flow conditions were taken from published ISUS data which lists a total flow rate for the ISUS RAC at 1.78 g/s at 23.1 $psia$ with an inlet temperature of 500 K. For modeling a single heat exchanger passage, this corresponds to a modeled mass flow rate of 0.009 g/s. As with the sensible TES materials, hydrogen was modeled with temperature dependent material properties and flow was considered to be both viscous and turbulent. Disassociation of hydrogen was not considered and hydrogen was treated as an ideal gas.

All solid exterior boundaries were modeled as adiabatic. The ISUS RAC utilized an advanced multi layer insulation system with a calculated thermal loss of 4800 W at a cavity temperature of 2300 K [25]. Published hydrogren flow data, taken with a lower RAC cavity temperature of 2150 K indicates a peak convective power draw exceeding 36,000 W suggesting that total insulation losses are less than 15% and can be neglected for the purposes of this comparison.

The initial thermal condition for the solid TES region in the STAR-CCM+ model was isothermal at 2360 K. This temperature is slightly higher than the ISUS design specification (2200-2300 K) but allows a direct comparison to a molten boron based system. The STAR-CCM+ model was run as an 2-D axisymmetric simulation using the implicit unsteady solver after establishing an initial starting condition for hydrogen flow at zero seconds.

The transient temperature profiles of this sensible heat model are given in Figure 4.1 and the mass flow average hydrogen exit temperature vs. time is given in Figure 4.2. As expected from published ISUS data, Figure 4.3 shows an initial segment where the hydrogen output is relatively isothermal taking approximately 250 seconds to drop below 95% of the initial value. As discussed in Section 3.3.5, hydrogen reaches relative thermal equilibrium before exiting the heat exchanger and this equilibrium point moves upstream as the rear of the passage cools, maintaining a region of steady performance. For comparison, the published data for the ISUS program takes approximately 380 seconds to drop by the same amount. The steeper cooling seen in the STAR-CCM+ model is due to neglecting the graphite caps present in the ISUS experimental design resulting in the absence of an additional 5 kg of graphite and 5 kg of rhenium as well as the additional hydrogen flow length which supports higher output temperatures.

Figure 4.1: Modeling geometry and transient temperature profiles for the "ISUS Approximation" STAR-CCM+ model. Model geometry is axisymmetric and represents the red outlined region of the cylindrical heat exchanger passage. Hydrogen flow through the passage is from left to right and dimensions are given in millimeters.
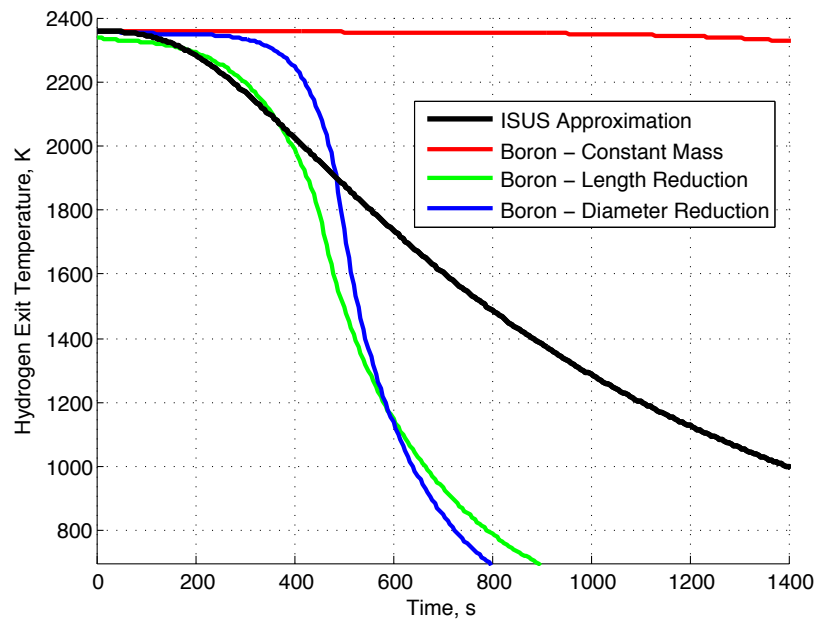
Figure 4.2: Mass flow averaged hydrogen exit temperatures for STAR-CCM+ heat exchanger simulations.
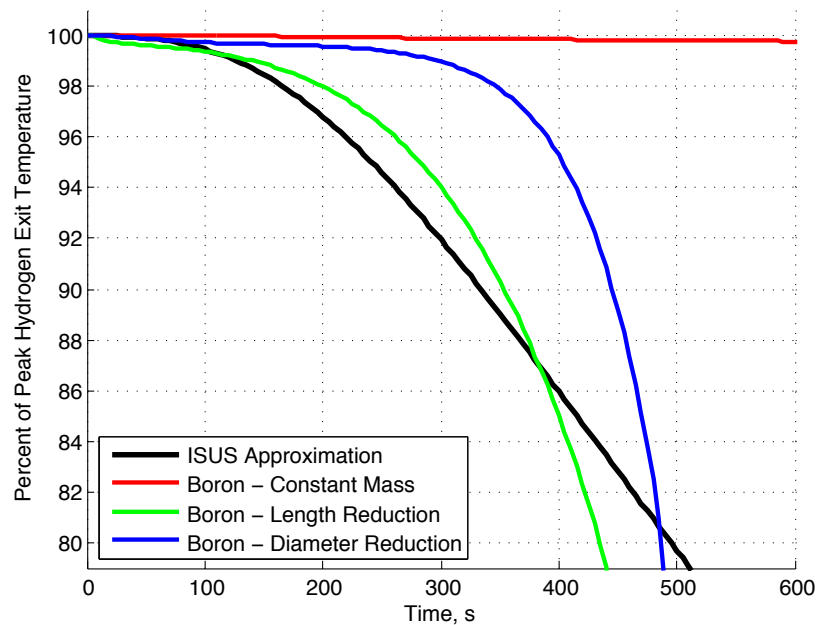
Figure 4.3: Mass flow averaged hydrogen exit temperature as a percentage of peak (initial) exit temperature for STAR-CCM+ heat exchanger simulations.

51

Boron Integration - Constant Mass

To see the effects of switching the sensible design to a boron based system, graphite TES was replaced with boron in the STAR-CCM+ model while keeping total system mass constant. Since boron has a higher density than TM graphite, the total diameter of the model was reduced to ensure that both the sensible and latent heat models both contained the same TES mass. Additionally, two 0.5 mm layers of boron nitride were included between rhenium layers and the boron TES to act as a suitable container for boron when it is liquid. The reasons for selecting boron nitride are discussed in Section 6.1. The overall geometry is given in Figure 4.4 and the total TES design contains 9.4 g of boron nitride, 52.6 g of rhenium, and 66.8 g of boron for a total system mass of 129 g.

The temperature transforming method was used to accommodate the latent heat release from the boron in the STAR-CCM+ model [78]. Boron was treated as a solid with a variable specific heat accounting for the latent heat release across a "mushy" zone of $\pm$ 2.5 K from the melting point (2350 K). Apart from this change, all model parameters and initial conditions were kept constant.

Figure 4.2 includes the hydrogen exit temperatures for this latent heat model ("Boron - Constant Mass") and demonstrates the effects of dramatically increasing the energy storage density of the TES system. In addition to prolonging the length of potential propulsive burns, the quasi-isothermal heat release during the phase change process produces an extremely stable output temperature which takes 1750 seconds to drop below 95% of the maximum. Thermal gradients, given in Figure 4.4, show that the freezing process takes in excess of 2000 seconds and that during phase change, propellant passage wall temperatures remain high.

Since I_{sp} varies with the square root of temperature, this dramatic increase in propellant output stability and longevity only effects total propulsive performance for long duration burns. For a single burn of 1400 seconds, the latent heat system delivers approximately 20% more ΔV than the sensible heat system. But, for burns less than 600 seconds, the latent heat system provides a ΔV
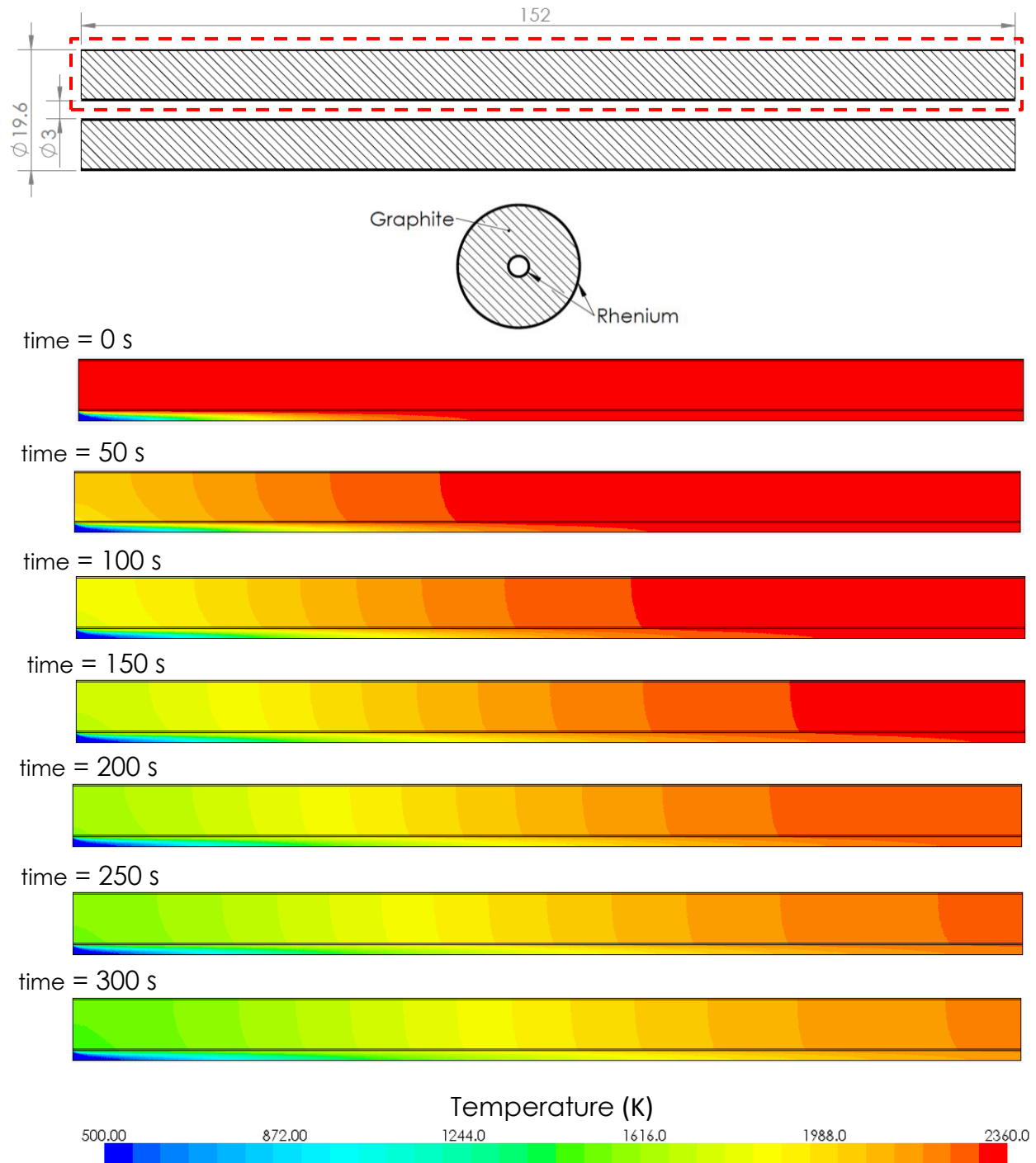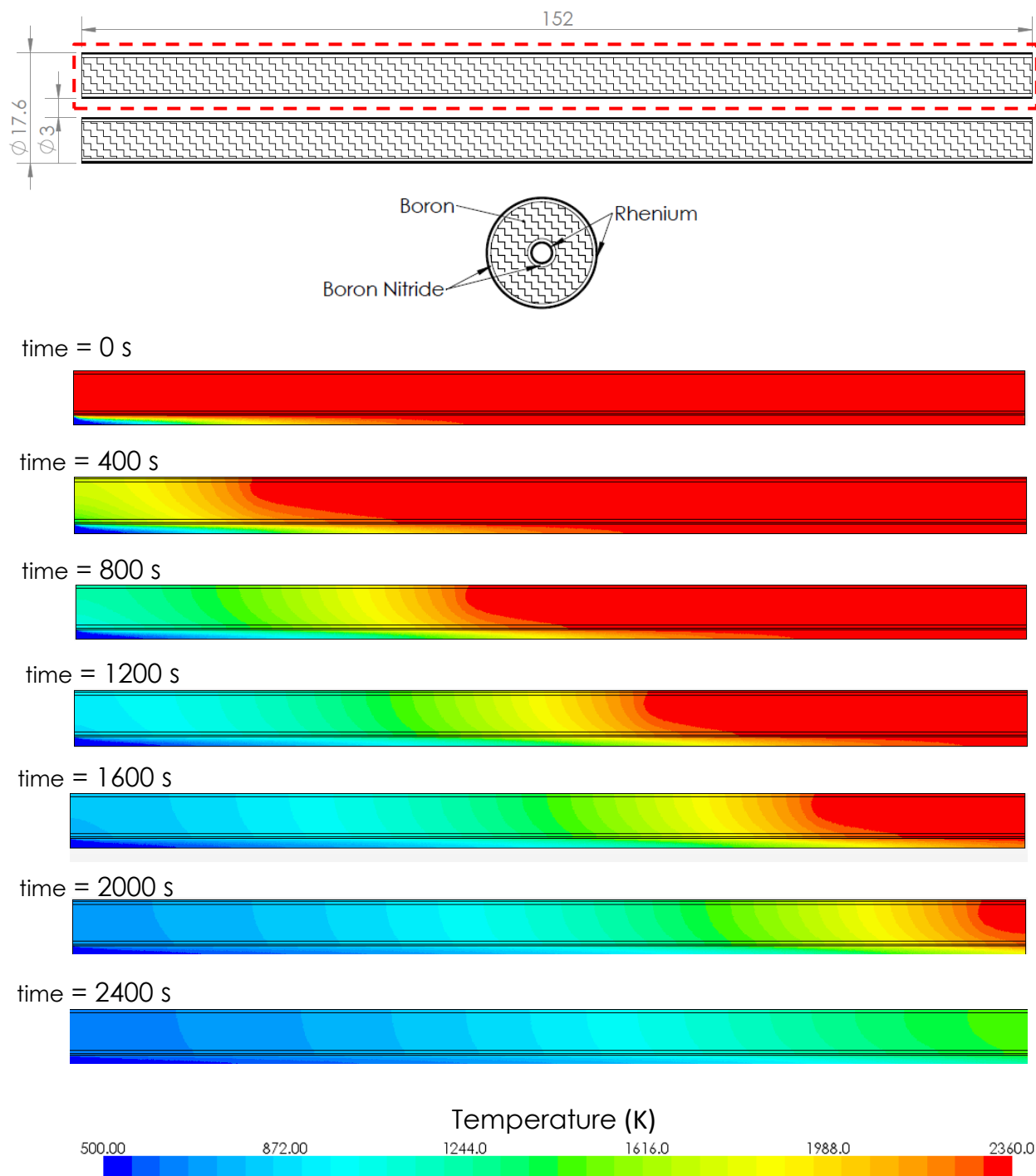
Figure 4.4: Modeling geometry and transient temperature profiles for the "Boron - Constant Mass" STAR-CCM+ model. Model geometry is axisymmetric and represents the red outlined region of the cylindrical heat exchanger passage. Hydrogen flow through the passage is from left to right and dimensions are given in millimeters.
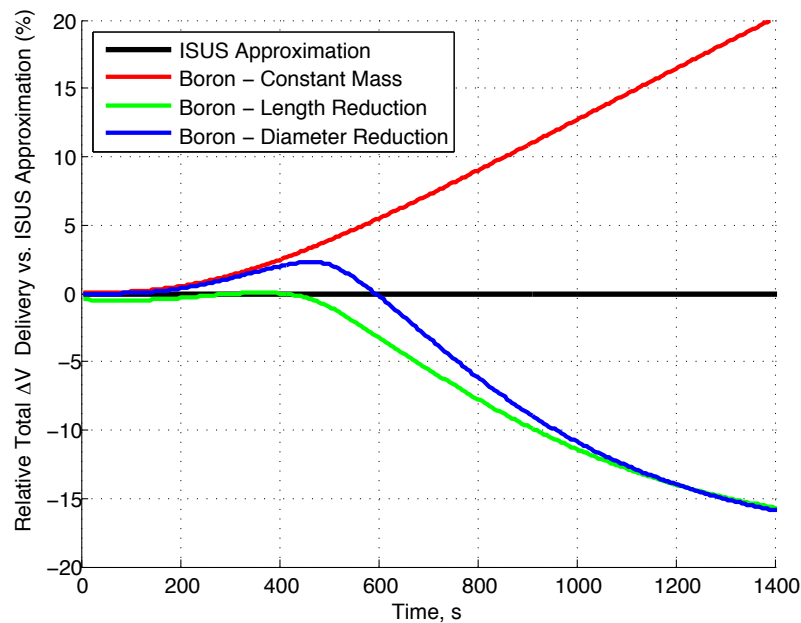
Figure 4.5: Relative ΔV delivery for representative heat exchanger models.

efficiency benefit of less than 5%. A comparison of relative ΔV for all STAR-CCM+ models is given in Figure 4.5.

Boron Optimization - Length Reduction

The dramatic improvement in temperature stability and burn longevity seen when switching from graphite to boron based TES is expected as the energy storage density of the system is increased more than fourfold due to the introduction of a latent heat component. However, if the performance of the sensible heat system is in fact adequate, an increase in energy storage density can be better used to optimize the system by reducing both total mass and volume of the heat exchanger. To examine this possibility, two models were created targeting either length or diameter reduction.

The first optimized system model attempted to replicate ISUS performance by taking advantage of convective coupling to a latent heat medium to reduce overall heat exchanger length. Both Figures 4.1 and 4.4 show that the initial convective coupling of the hydrogen propellant occurs

54

early within the channel. At approximately one third of the total heat exchanger length, propellant temperatures are within 5% of the target output temperature. At the midpoint of the heat exchanger, propellant temperatures are within 2% of this target value. It is proposed that this convective profile is advantageous in the design of a latent heat based system. If the latent heat PCM maintains a stable temperature profile during energy release, the total length of the heat exchanger can be cut in half reducing both mass and volume.

A new model heat exchanger passage was created to investigate this optimization method and the heat exchanger length was reduced to 76 mm from 152 mm. Total boron thermal energy storage mass was sized based on steady performance from the sensible heat model for which the output temperature remained within 5% of the maximum temperature for roughly 250 seconds requiring 67 kJ of energy delivery from the thermal energy storage (effective energy storage density of 0.52 MJ/kg). To maintain this output with a shortened heat exchanger, all of the energy must come from the boron phase transition which sets the total boron mass for the system at 14.6 g of boron vs. 77 g of graphite.

Other parameters for the model were held constant including rhenium coatings on the inner and outer surfaces as well as the inclusion of the 0.5 mm BN liners. The end geometry resulted in a total system mass of 38 g corresponding to a 70% reduction in mass vs. the full scale model. Additionally, total volume of the heat exchanger passage was reduced by 79%.

Transient thermal profiles for this optimized case are given in Figure 4.6 and mass flow averaged hydrogen exit temperatures are included in Figure 4.2 ("Boron - Length Reduction"). After an initial brief drop in temperature before the beginning of the phase change process, this optimized system maintains a steady output temperature for approximately 280 seconds, exceeding the performance of the sensible heat system and the design goal for the optimized configuration.

However, it must be noted that after this initial period of stability, the exit temperature for the length optimized system rapidly drops in temperature. The reasons for this are twofold; first, the system is almost entirely reliant on latent heat energy storage due to the dramatic reduction in

55

mass. Once this latent heat is exhausted, there is comparatively little sensible heat which can be drawn from the system to maintain output temperatures.

Second, the extremely low thermal conductivity of solid boron (approximately 5 W/mK near the melting point) allows dramatic thermal gradients to form within the system supported by the remaining still liquid PCM. When the phase change is complete, the slow diffusion of thermal energy within the thermal energy storage medium results in maintained high temperature regions near the exit of the heat exchanger. Convective coupling to this thermal environment is very inefficient since the propellant stream does not see a high wall ΔT until shortly before exit.

Boron Optimization - Diameter Reduction

Another route to optimization simply reduces the mass of the system while leaving the heat exchanger channel length the same. For this model, the amount of boron was sized as a direct replacement for the graphite TES while maintaining the same convective coupling length.

The sensible heat ISUS model reaches 1 MJ/kg of effective energy storage density approximately 500 seconds into the burn. Targeting this energy storage capacity requires only 13.2 g of boron to replace the 77 g of graphite used in the sensible case. The boron mass calculation includes both the latent heat and the sensible heat contributions across the assumed ΔT. Due to boron's relatively high specific heat, the sensible component accounts for 20% of the total energy storage.

All model parameters are kept the same as the "Boron - Constant Mass" case apart from reducing the total amount of boron. Rhenium coatings and BN protective layers are still included which brings total exchanger mass to 51 g corresponding to only a 60% reduction over the sensible case. Total passage volume is reduced by 75%.

Transient thermal profiles for this optimized case are given in Figure 4.7 and mass flow averaged hydrogen exit temperatures are given in Figure 4.2 ("Boron - Diameter Reduction"). This configuration yields a steady output temperature for 425 seconds exceeding both the sensible

56

Figure 4.6: Modeling geometry and transient temperature profiles for the "Boron - Length Reduction" STAR-CCM+ model. Model geometry is axisymmetric and represents the red outlined region of the cylindrical heat exchanger passage. Hydrogen flow through the passage is from left to right and dimensions are given in millimeters.

design case as well as the length optimized case. It also must be noted that in the relative ΔV data, this optimized case provides slightly better performance over 500 seconds.

Because of the increased passage length, boron is spread throughout the system and as large thermal gradients form, the propellant is still able to couple to high temperature regions later in the channel. However, much like the length optimized case, the reliance on latent heat energy storage results in a sharp drop off in propellant temperatures after the phase change process completes.

Summary

Modeling a representative conjugate heat transfer system has shown that integrating latent heat materials into a heat exchanger design is theoretically feasible and that the high performance of boron as a latent heat thermal energy storage material can be used to either dramatically increase system performance or reduce total system mass.

It must be noted, however, that latent heat systems behave differently than a sensible heat system and optimization must take into account the burn times required by the target mission. Modeling results indicate that comparisons between sensible and latent heat systems are more complex than the purely material property based comparisons found in the existing literature. ΔV delivery comparisons in Figure 4.5 show that similarly sized latent heat systems only provide propulsive benefits for long duration burns, and the dramatic mass reductions created through optimization are only able to match performance for certain burn durations. Certainly, any system designed specifically for latent heat thermal energy storage will take these operating characteristics into account.

Mass and volume are primary constraints on a microsatellite platform and the dramatic improvements in both metrics demonstrated by switching to latent heat materials yields significant advantages against sensible heat configurations. When targeting an aggressive ΔV budget on a microsatellite the mass and volume of sensible heat systems render them infeasible and thus
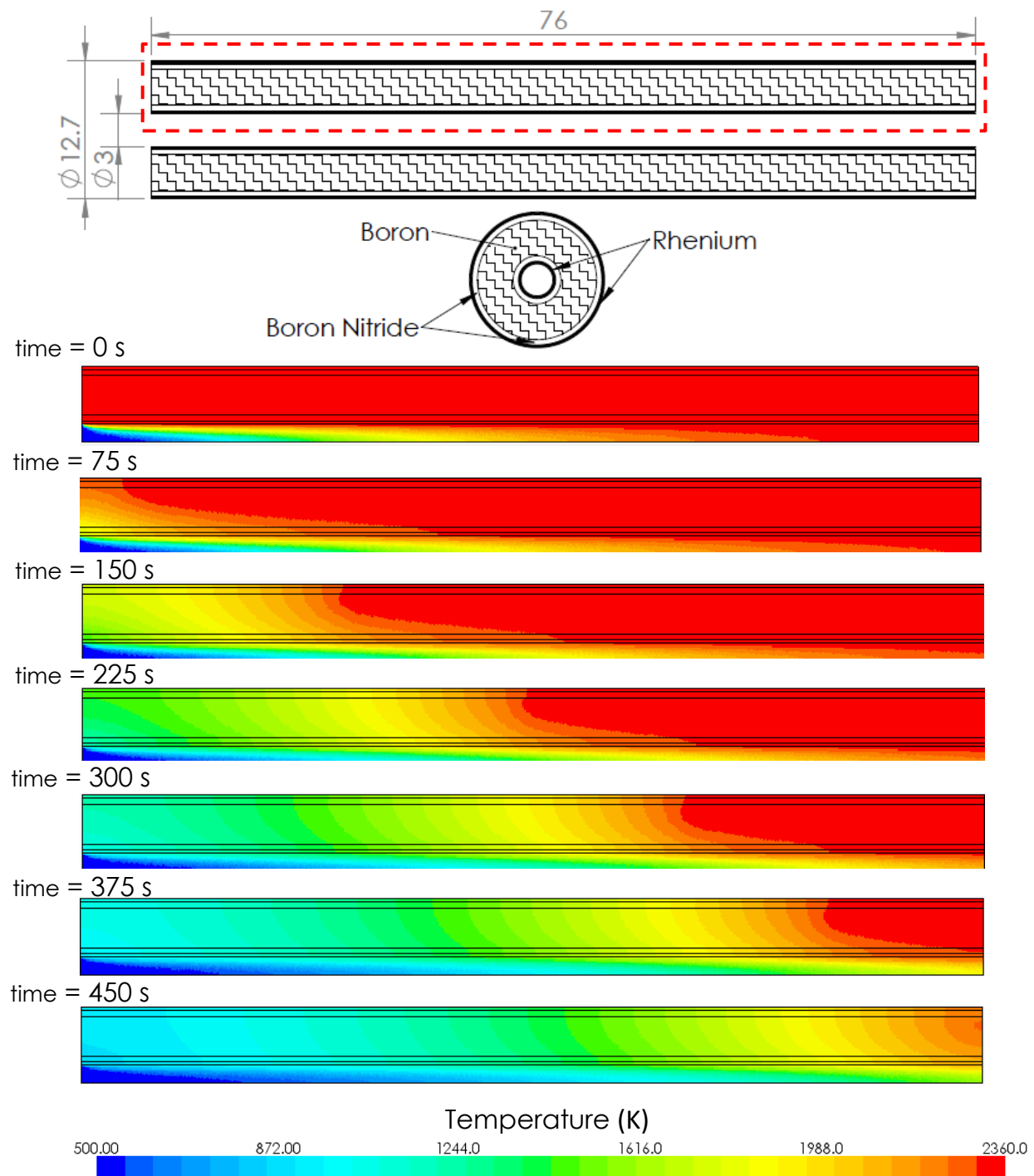
58
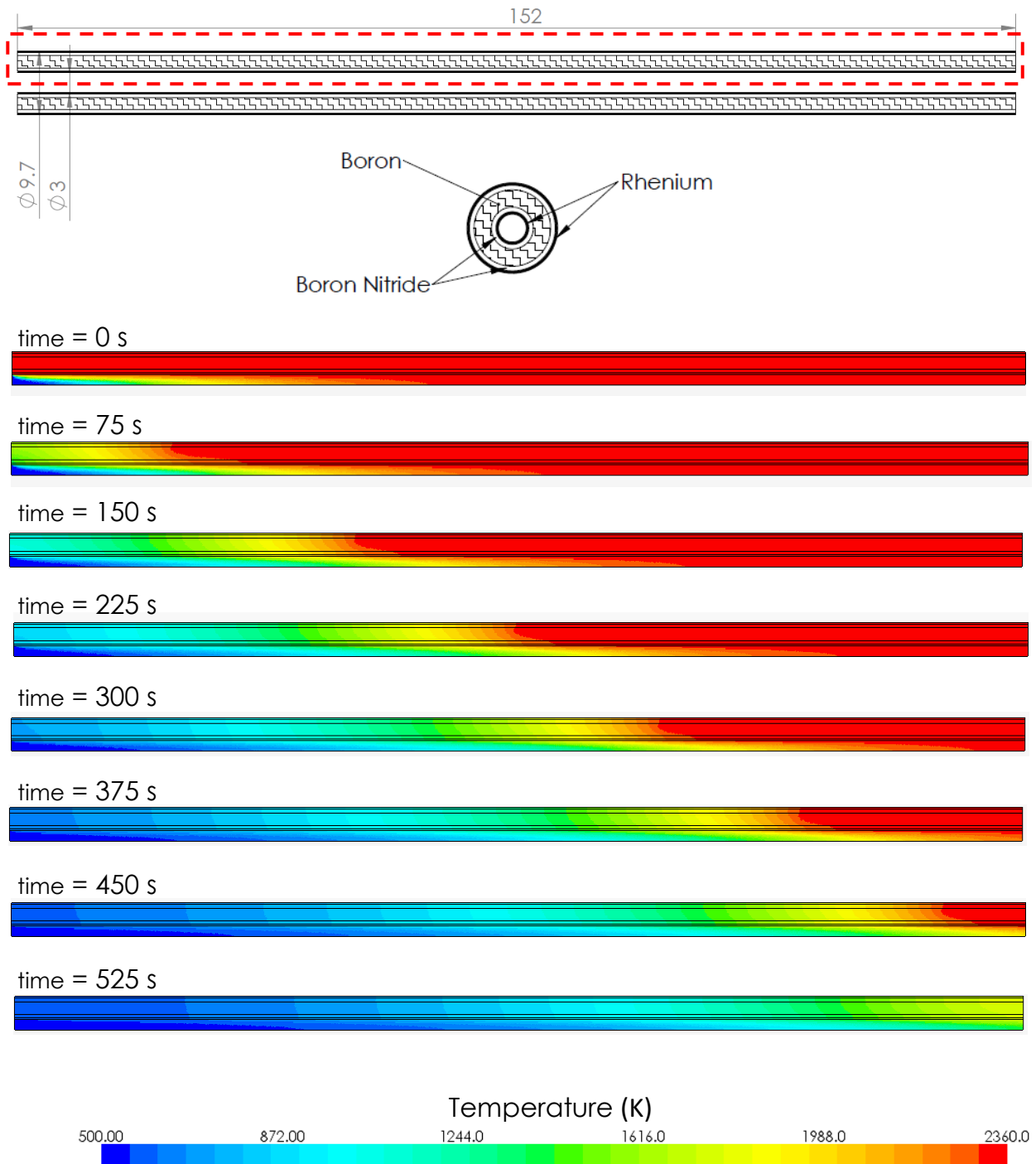
Figure 4.7: Modeling geometry and transient temperature profiles for the "Boron - Diameter Reduction" STAR-CCM+ model. Model geometry is axisymmetric and represents the red outlined region of the cylindrical heat exchanger passage. Hydrogen flow through the passage is from left to right and dimensions are given in millimeters.

latent heat thermal energy storage is an enabling technology. The following comparison seeks to determine the impact of an implemented latent heat based system on a microsatellite platform.

4.2.2 Microsatellite Performance Impact

An initial systems level analysis has been performed with the AFRL to compare the proposed bi-modal STP system against existing propulsion technologies [79]. Theoretical bi-modal solar thermal systems were sized using a variety of parameters (i.e. propellant budget, desired ΔV, phase change material, etc.) and compared against current conventional capabilities. It has been shown that, even when using conservative assumptions, the development of silicon and boron as PCMs can have a strong impact on microsatellite performance.

A sample bi-modal STP system was sized for a 100 kg microsatellite with a 1500 m/s ΔV capability to target the high-performance microsatellite category. Energy storage and conversion subsystems for the baseline spacecraft were required to simultaneously provide 100 W of full-time electrical power and 100 W of thermal propulsive power in a low Earth orbit (LEO) using silicon as the PCM. These requirements are similar to a proposed space demonstration study that was to follow the ISUS program. The proposed mission was to launch from a Pegasus XL rocket and place a 207 kg satellite into LEO with a buss power output of 100 W, a ΔV capability of approximately 1600 m/s and a propulsion and power mass fraction of 61% [80].

The sizing of the bi-modal STP system, including all power and propulsion components, was based upon previous research and readily-achievable technological solutions [1, 34, 61, 81, 82]. Parameters of interest during the mass budgeting process included the weight of the solar concentration system (fiber optics, primary concentrator and support structure), thermal energy storage mass (PCM, container and insulation), power system weight (TPV, radiators, electronics) and the weight of an ammonia STP propulsion system (tankage, flow system, engine and propellant weight). Total thermal efficiency of the propulsion and power unit was approximately 17.5% assuming 70% thermal collection efficiency, storage losses of 25% per orbit, and 20% thermal

60

electric system efficiency. Calculations also assumed that thruster firing would only occur for 5% of the mission duration at 20-times the average power (i.e. near apogee and perigee of maneuver orbits for efficiency) to approximate an impulsive burn strategy.

The base system was sized to produce $1500 \, m/s \, \Delta V$; calculations showed that this ΔV could be delivered in under 23 days with a combined propulsion and power mass budget of just over $58 \, kg$ utilizing silicon as the PCM and essentially "proven" system components documented in the literature.

Holding the propulsion and power mass fraction of 58% constant (i.e. assuming systems for comparison must have an identical mass budget for the payload and other non-propulsion and power systems on a $100 \, kg$ microsatellite), system budgets and capabilities were calculated for competing technologies published in the literature, including a $1 \, N$ Hydrazine thruster [83], a $20 \, N$ hydrazine thruster [84], a standard (non-bi-modal) STP system and a $100 \, W$ Hall Effect Thruster [85]. It was assumed that all of these technologies included photovoltaic panels and batteries suitable to meet the same $100 \, W$ electrical power draw while propulsion systems were active.

The results of these calculations, along with the results for the silicon bi-modal system, are presented in Figure 4.8. As with the bimodal system sizing, the relative weights of power systems, tankage and thrusters were determined primarily through previously established sizing metrics [86, 87]. NASA's year-2020 target for photovoltaic power density was used to size the traditional power systems, saving mass relative to current available technologies [88]. Additionally, it should be noted that for chemical and electrical propulsion cases, it was assumed that the thrusters fired continuously to deliver the desired ΔV. This would result in orbit-change inefficiency, and a smaller orbit change relative to the ΔV imparted. Alternatively, if the same 5% firing time was enforced on these thrusters as the proposed STP systems, the maneuver times would have been increased by a factor of 20, pushing the comparative system response significantly higher.

In spite of this analysis being bent to favor the competing technologies, Figure 4.8 shows the unique position occupied by the STP systems. The standard STP option already occupies a performance gap between chemical and EP systems, allowing a slightly higher ΔV than the chemical systems without the years-long maneuver time of the hall thruster. When the silicon thermal energy storage system is added and the thermophotovoltaics and batteries are replaced by a bi-modal system, the response time drops slightly and ΔV capability shows a 10% advantage over chemical systems due to an increase in propellant mass and propulsive efficiency.
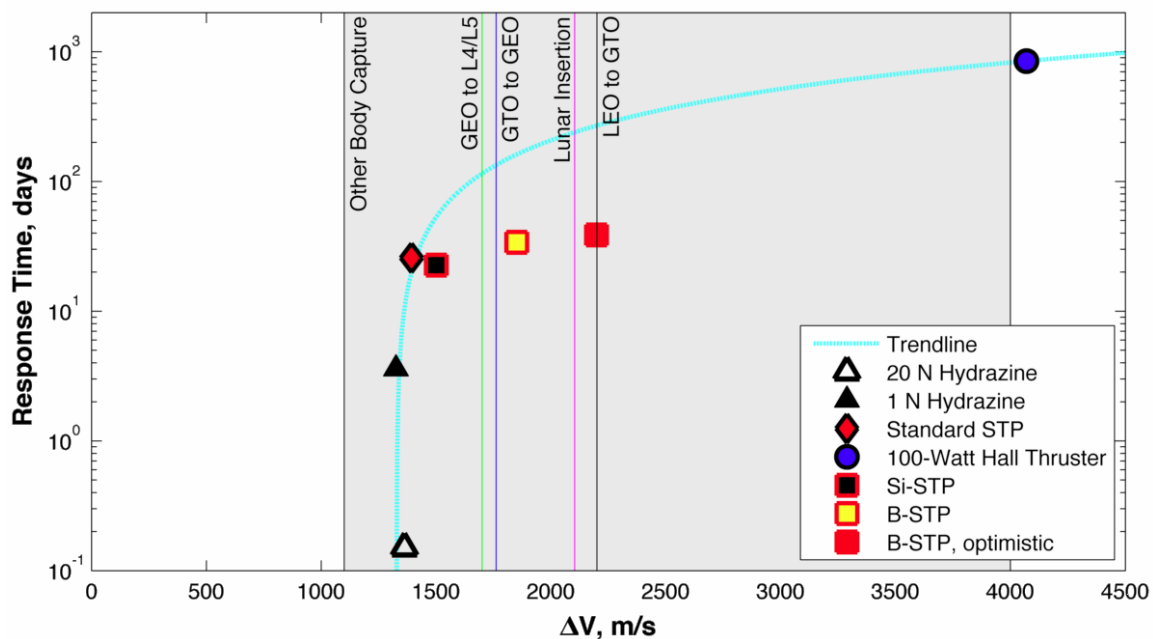
Figure 4.8: Systems comparison of the proposed bi-modal solar thermal system versus competing technologies. Vertical lines indicate specific mission ΔV requirements and the blue trendline indicates the trade off between mission duration and ΔV typical of conventional propulsion concepts.

Replacing the silicon PCM with boron reduces the amount of PCM required, allowing for slightly more propellant within the power-and-propulsion mass budget. Simultaneously, the boron based system operates at a higher temperature, yielding higher I_{sp} (but slightly decreasing the thrust and increasing the response time. This is consistent with the assumption that average propulsive thermal power draw remains constant). With this change, and still sizing other power and

62

propulsion components via published readily-achievable technology, the response time increases slightly to 34 days, but the total available ΔV increases to over 1850 m/s. The boron system has a 35% ΔV advantage over chemical rockets while still providing a highly-responsive architecture.

Making more optimistic estimates for system components (i.e. increasing the TPV plus radiator power efficiency from currently-available 15 W/kg to 30 W/kg and cutting fiber optic mass from 5 to 2.5 kg) yields an advanced bi-modal boron-STP system with a response time of under 40 days and a total ΔV approaching 2200 m/s. At this level, the STP system can provide a ΔV that cannot be reasonably considered using chemical systems, while remaining several orders of magnitude more responsive than an EP system at the same ΔV (2200 m/s in > 500 days).

Since microsatellites can be delivered into orbit at relatively low cost by piggy-backing on the launch vehicles of larger satellites, the ability to rapidly reposition into a drastically different orbit (i.e. the desired orbit for the microsatellite mission) can significantly enhance the utility and frequency of microsatellite launches. Additionally, note the sample maneuvers marked via the vertical lines and shaded areas on Figure 4.8 [34]. Development of the proposed bimodal STP technology could provide for a microsatellite platform that can not only piggy-back on the launch of a conventional satellite and reposition itself accordingly, but could also result in microsatellites capable of transferring into Lagrange Point orbits or even inserting into lunar or asteroid orbits.

4.3 Existing Literature

In the solar thermal propulsion literature, the use of high temperature phase change materials for thermal energy storage has been mentioned briefly in the context of broad conceptual studies. Silicon or boron are often proposed as promising thermal energy storage candidates based on their material properties and then consequently rejected in favor of sensible heat options due to operational and programmatic concerns. For example, the ISUS program stated that latent heat storage materials would increase energy density and simplify both the design and testing of the thermionic system due to a narrow thermal cycling range. However, the use of phase change

63

materials was rejected before the design phase of the program due to the extremely low TRL level of existing research and an ambitious project schedule.

Kennedy's microsatellite work similarly selected sensible heat thermal energy storage due to simplicity of design and "moderate but acceptable performance levels" [34]. Kennedy states that complications in phase change energy storage systems stem from void formation and containment structure bursting. However, the papers referenced only discuss the former in the context of $LiF - CaF_2$ based energy storage systems [22, 89]. Kennedy does briefly mention boron and silicon as potential storage materials and cites their material properties. But, like the ISUS program, Kennedy's work rejects the use of phase change materials before the design phase and makes no estimates of their performance [3].

An early assessment from the AFRL of a bi-modal solar thermal system assumes the use of silicon as a thermal energy storage material and makes basic estimates of system performance [17]. The paper states that a bi-modal configuration using silicon thermal energy storage would offer a flexible and responsive spacecraft architecture. However, it appears that silicon properties were simply used for top level analysis [17]. A contemporary paper from Rocketdyne is the first paper to discuss boron as a thermal energy storage medium for solar thermal propulsion beyond a simple listing of material properties [11]. Shoji's analysis states that a boron based thermal energy storage system would actually raise the propulsion subsystem mass. But, his analysis does not consider a bi-modal configuration and thermal energy storage is only seen as a means for reduction in solar concentrator area keeping with the findings proposed by Ethridge a decade prior [4].

In 2001 Ontario Engineering Int. proposed a tri-modal satellite bus with the potential for silicon thermal energy storage. The study again only looked at broad material properties and noted that the technology would be of interest in comparison with graphite [90]. Most recently a study funded by ESTEC/EADS in 2003 looked at the possibility of a solar thermal upper stage to reduce launch mass and overall costs [91]. The spacecraft targeted in this study did not consider bi-modal operation, and much like in Shoji's analysis, determined that the addition of TES system would

64

reduce available payload mass using silicon or graphite. Interestingly, it was stated that boron was an exception. However, later analysis utilized graphite based storage.

Recently, there has also been a renewed interest in nuclear thermal bi-modal spacecraft systems. Researchers at the Center for Space Nuclear Research at the Idaho National Laboratory have proposed a bi-modal propulsion and power bus to allow interplanetary exploration of the solar system using small satellites [92]. To increase the specific power that can be achieved with a radioisotope thermal generator, a thermal capacitor system has been proposed to allow for high power propulsive burns and burst generation of electrical power for communications through the use of closed Brayton cycle dynamic thermoelectric conversion. High performance sensible heat thermal energy storage along with boron and silicon based TES were considered with the program ultimately settling on using silicon as the primary TES. This research is currently ongoing and many of the concerns raised about molten silicon thermal energy storage parallel those raised in the early stages of this research effort.

The body of available literature considering boron and silicon based thermal energy storage for terrestrial applications is similarly narrow. Furthermore, there is very limited research into molten boron itself, let alone its use as a PCM. Terrestrial research into high temperature phase change materials is primarily associated with thermophotovoltaic development projects. Woodall, in a patent assigned to IBM in 1982, is the first to mention silicon specifically as a potential energy storage material [93]. Intended as a buffer for a TPV emitter, silicon was proposed along with other materials meeting temperature, thermal conductivity, and energy density requirements which included iron, manganese and chromium. Woodall also proposed potential container materials such as boron nitride and aluminum oxide and went on to melt silicon in pyrolitic BN crucibles to confirm the latent heat value. However, experiments ended here and the proposed buffer-storage system was never built.

The most substantive research into the use of using molten silicon as a thermal energy storage material was first presented by Chubb, Good and Lowe in 1995 as part of thermophotovoltaic

65

Figure 4.9: Diagram of of the silicon freezing model proposed in Chubb et al [5]. Note the large reciever area (A_s) and small emitter are (A_E) which are intended to smooth thermal gradients during the freezing process.

development at what was then McDonnell Douglass [5]. Similar to Woodall's proposal, silicon was to be a thermal energy storage material for a terrestrial TPV system and would allow for continuous operation. In addition to selecting silicon as a PCM, a 1-D model for PCM solidification was presented in a conical enclosure. As shown in Figure 4.9, this model assumed a large receiver (A_S) and smaller emitter (A_E) which would result in higher energy flux at the emitter during silicon solidification and a lower temperature drop between the receiver and emitter during "on-sun" operation. This model was not silicon specific and could be applied to any PCM based system. Multiple large assumptions were also made, including perfectly insulated walls and the neglect of volumetric expansion effects in the PCM. The paper concluded that silicon would make an "ideal" thermal storage material for TPV systems but no experiments were performed. This research was granted a patent in 1999 and the combined TPV reciever and storage system was estimated to have a combined thermal-electric conversion efficiancy of 27-51% [94].

In 2013, a paper published by Datas, Chubb and Veeraragavan revisited the 1-D PCM model originally proposed in 1995 to perform further analysis on the TPV buffer concept [95]. Datas initially looked at the steady state performance of a system using the same conical geometry and adiabatic wall assumptions stated in Chubb's paper with the intent of mapping steady state on-sun performance of the system and optimizing geometric factors for maximum thermophotovoltaic efficiency. A follow-up paper in 2014 by Verraragavan, Montgomery, and Datas applied a transient model to the conical PCM geometry to gauge night time performance of a silicon based system and concluded that high energy storage density of silicon produces sufficient storage durations to be feasible [96]. The authors intend to refine the PCM model beyond that originally proposed by Chubb and include factors such as, 2-D phase front treatment, insulation losses, natural convection in the PCM and reservoir orientation and make no mention of future experiments.

In summary, within the existing literature concerning both silicon and boron as phase change materials there is broad agreement that their outsized energy storage densities could have significant impact on energy systems operation. However, considering the low TRL level of high temperature phase change thermal energy storage both materials have been either neglected, as with solar thermal propulsion research, or relegated to side projects and white paper studies in the case of terrestrial applications.

4.4   Research Goals

The use of high temperature latent heat thermal energy storage has been in the background of both solar thermal and terrestrial thermophotovoltaic research projects for the past two decades. Simple technological comparisons have proposed broad operational and capability advantages if the technology were available. However, to-date there has been no motivation to begin a thorough investigation.

This work proposes that the benefits of solar thermal propulsion can be amplified by implementing a bi-modal system on a microsatellite platform and technological comparisons presented

here demonstrate that significant performance gains are in-fact possible. Such a satellite would be more than just a long awaited technology demonstration of solar thermal propulsion, it would be a high performance microsatellite platform unrealizable with conventional systems.

The component technologies required for a viable bi-modal microsatellite have all reached sufficient technological maturity with the exception of high performance latent heat thermal energy storage. It is the goal of this study to determine the basic feasibility of this enabling technology and facilitate the development of a bi-modal solar thermal microsatellite.

Specifically, this work seeks to perform the first substantive experiments targeting silicon as an energy storage material. An experimental approach is being taken to uncover the practical design concerns which are currently absent from the literature. Concentrated sunlight will be used to generate liquid silicon in the laboratory to evaluate potential container materials and uncover major technological challenges. Additionally, experimental results will be used to evaluate the modeling fidelity required to capture macro system behaviors.

Experiments and analysis target silicon as opposed to boron due to the lower melting temperature effectively reducing project costs by an order of magnitude when considering solar furnace and custom material requirements. Additionally, silicon research and facility development have broad applications when considering terrestrial potential of the technology.

Chapter 5

Solar Furnace Development

A new solar furnace facility has been constructed at the University of Southern California in order to create molten silicon in the laboratory and evaluate the practical concerns associated with using high temperature latent heat materials. Using a solar furnace to drive experiments forces designs to accommodate a single-point energy input and provides correlation with potential spacecraft applications. Solar furnace construction was also driven by a desire for a facility which could support future thermophotovolatic research due to the broad terrestrial applications of a silicon based energy storage system.

The USC solar furnace has progressed through multiple iterations and makes ample use of commercial off the shelf (COTS) and surplus components resulting in a low-cost design. The furnace is capable of peak solar concentration ratios in excess of 4000:1 and an average power delivery of approximately 800 W.

5.1 Initial Designs and Diagnostic Development

Construction of a new solar furnace facility at USC required the simultaneous development of both the solar concentration system as well as relevant diagnostics. To support this process, a simple solar furnace was constructed using a surplus Fresnel lens as the primary concentrator. While this

69

furnace exhibited a total system efficiency of only 25%, it did succeed in supporting diagnostic development, evaluation of experimental methods, and the first round of solar furnace experiments.

Not included in the discussions of solar furnace development are attempts to produce a large scale solar concentrator through metalization of a commercially available fiberglass parabolic antenna [48]. This effort ultimately proved unsuccessful after a multi-month fabrication process due to difficulties associated with an even application of metalization chemicals across a large surface using the SpectraChrome process.

5.1.1 Fresnel Lens Based Development Furnace

The first iteration of the USC solar furnace facility consisted of a heliostat and a large acrylic Fresnel lens diagrammed in Figure 5.1. The testing chamber, diagnostics and concentrator are fixed with respect to the lab and the heliostat mirror is the only moving component. The heliostat compensates for solar motion throughout the day by maintaining a reflected sunlight vector normal to the Fresnel lens. This configuration simplifies design at the expense of additional reflection losses compared to single stage designs requiring motion of both the solar concentrator and the testing chamber.

Fresnel Lens and Vacuum Chamber

The primary concentrator during development of the solar furnace was an acrylic Fresnel spot lens originally used in a rear-projection television. The 1.1 m by 0.84 m lens, shown in Figure 5.2, has a focal length of approximately 1 m. The lens was framed and mounted on rails to allow for the position of the focal point to be shifted with respect to the testing chamber.

The testing chamber is a 15.2 cm (6 in) CF cross coupled to a larger vacuum chamber via an extension in order to place vacuum pumps and electrical feeds outside of experimental area. Sunlight enters the testing chamber through a 15.2 cm diameter, 0.64 cm fused quartz window which is held onto the chamber via an o-ring seal and the pressure differential between the chamber
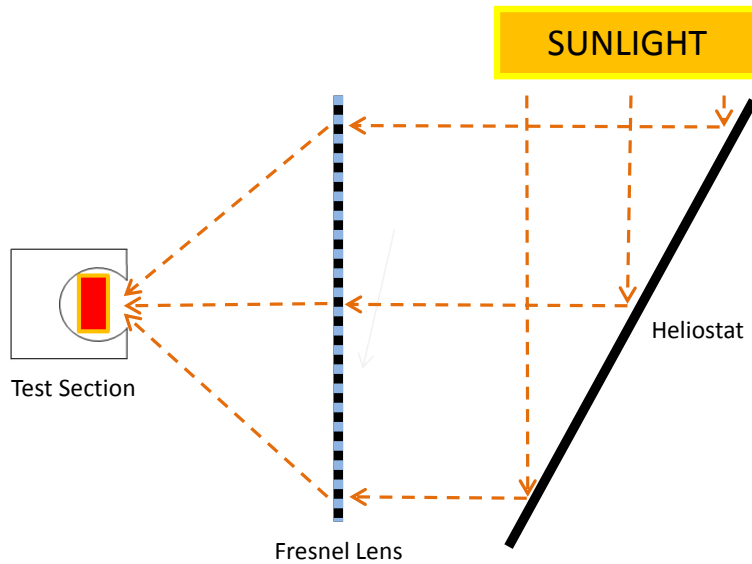
70

Figure 5.1: Path diagram for the Fresnel lens based solar furnace.

and ambient. This design allows for low cost quartz blanks to be used as opposed to integrated vacuum chamber viewports and facilitates easy removal for cleaning.

The fresnel lens based solar furnace was capable of delivering approximately 200 W into a 19 mm diameter spot. This power level was insufficient to reach silicon melting temperatures. However, the development furnace enabled evaluation of heliostat performance and diagnostic development.

Heliostat Drive

An altitude-azimuth heliostat drive was obtained as surplus from the AFRL and was previously used in the AFRL solar thermal research facility during the 1980s and early 1990s. The tracking drive, shown in Figure 5.3, had been stored outdoors for over a decade and required a complete rebuild of the drive motors, replacement of all control electronics, the creation of new tracking software, and the installation of a new mirror assembly.
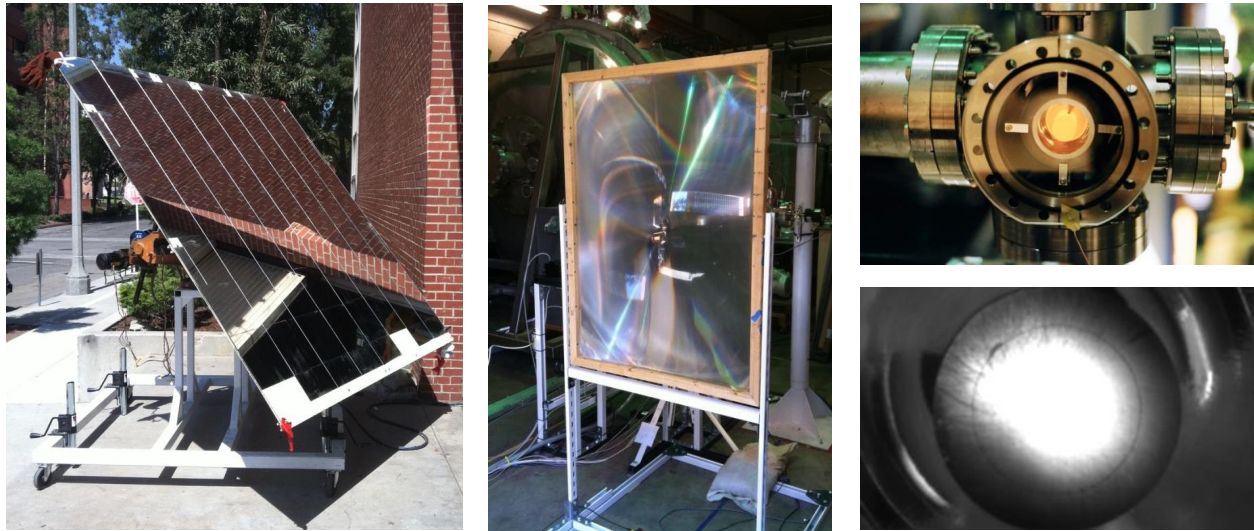
71

Figure 5.2: Photographs of the Fresnel lens based solar furnace including the first iteration of the heliostat, the Fresnel lens, the testing chamber showing a glowing test article after furnace power is removed, and an infrared image of the Fresnel lens output on the face of a 0.75" diameter graphite test section.

The heliostat is driven by two AC gear motors with speed further reduced by the altitude and azimuth tracking hardware. Control for each motor is handled via a variable AC motor controller capable of accepting digital on-off control signals as well as an analog programing signal for motor speed. Even with speed control and considerable gearing reduction, the heliostat's minimum constant slew rates (32 arcseconds per second for azimuth and 52 arcseconds per second for altitude) are too fast to provide constant rate tracking of the sun. As an alternative to constant rate tracking, a minimum reliable motion step was established considering spin-up and spin-down times for the AC motors and gear trains to implement discrete tracking control. The minimum reliable movement increment for the heliostat was established as $0.036°$ and $0.026°$ for the altitude and azimuth drives respectively. Since the recommended and calculated total heliostat pointing accuracy is between $0.1°$ and $0.25°$, this is sufficient for operation with minimal manual intervention [4, 97].

Heliostat control is implemented in National Instruments (NI) LabView software and is run on a standard desktop PC. Analog and digital control signals are provided using an NI PCI-6281
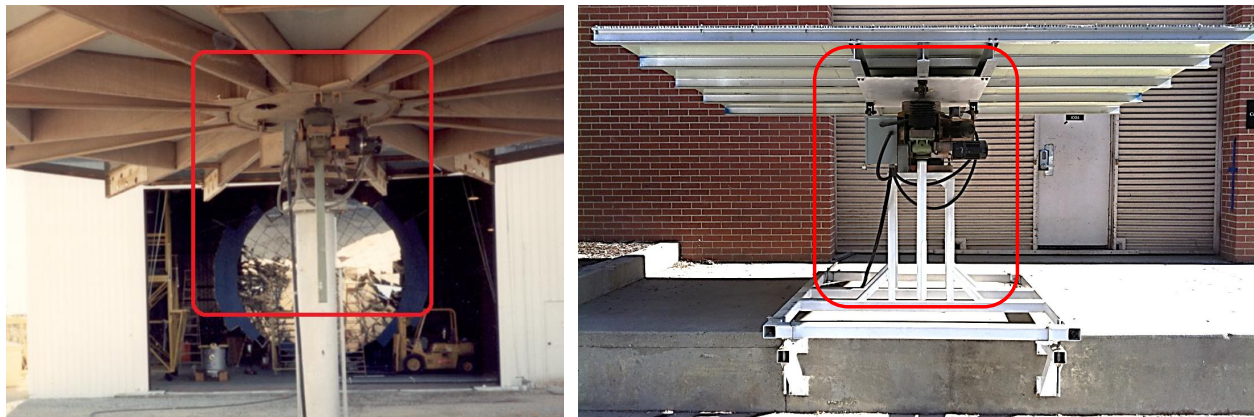
72

Figure 5.3: Surplus heliostat tracking unit shown installed at the AFRPL solar facility (left) and at the current USC solar furnace facility (right). The unit received a full rebuild before being installed at USC.

multi-function DAQ via a tether to the AC motor controllers which are mounted on the Heliostat body. The control software is capable of providing slewing capability as well as automated open-loop solar tracking.

Automated tracking control uses published algorithms to calculate the local solar position in real time as well as the rate of solar motion [98, 99]. The calculated local solar vector, a supplied known target vector, and the heliostat position are then used to calculate the mirror orientation required to provide a normal incoming solar vector to the concentrator after reflection. The algorithm uses this information to calculate the necessary mirror movement rates to maintain a normal solar vector and uses the established minimum control increments and known step time to reproduce the required motion.

An open-loop tracking configuration is advantageous since it only requires an accurate assessment of the heliostat location, target vector and initial placement of the solar vector on the test section. Not relying on the absolute position of the heliostat for closed loop control was particularly beneficial during these early stage tests since the heliostat arrived pre-configured with rheostats for angle sensing. The minimum angular increment of these sensors was found to be approximately $0.3°$ which is insufficient for closed-loop operation.

73

The final component of the heliostat requiring restoration was the heliostat mirror panel. The heliostat drive arrived at USC with a small circular mirror attached that originally served as a hub for a large spoked mirror panel which can be seen in Figure 5.3. Two 1.2 m by 1.4 m aluminum honeycomb panels were fixed to the top of the existing circular mirror to create a mounting surface and 30.5 cm square mirror panels were adhered to create the new mirrored surface. To protect the mirrored surface, the heliostat was stored inside the lab and rolled outside on rails when in use.

5.1.2 Commercial Diagnostics

The USC solar furnace relies on commercial diagnostics for measuring ambient solar conditions, characterizing total solar power delivery by the furnace, and the measurement of experimental temperatures.

Ambient solar conditions are characterized by measuring the direct normal insolation which is defined as the power per unit area at the surface perpendicular with the solar vector. This measurement, given in W/m^2, excludes diffuse radiation and represents the sunlight available for reflection by the heliostat. Measurements of the local solar insolation are performed by an Eppley Normal Incidence Pyreheliometer. This instrument is considered a "secondary standard" and comes from the factory with a supplied calibration and stated error of less than 1%. Since the pyreheliometer must maintain alignment with the solar vector, the instrument has been mounted to an automated commercial telescope tracking mount. The signal output for the pyreheliometer is recorded during testing in real time using a 24 bit NI DAQ due to the low signal levels (typically 4-8 mV).

Total power delivery by the solar furnace is characterized using a commercial thermopile based laser power meter. The Newport 818P-3KW-60 is capable of sustained measurements of up to 3 kW into a 60 mm diameter aperture with an uncertainty of approximately $\pm5\%$. By combining measurements from the power meter and the pyreheliometer, a relationship between the measured insolation and total delivered solar furnace power can be obtained. This is used during testing to estimate power delivery as a function of time.

74

Experimental temperatures are recorded by Type C and Type K thermocouples. Type K thermocouples are logged by a 16 channel NI thermocouple specific DAQ (NI-9213). Type C thermocouples are displayed by OMEGA thermocouple controllers which output a linear voltage signal proportional to the temperature measurement range. This signal is used to log Type C temperatures through a 24-bit NI DAQ. All thermocouple channels are calibrated and verified using an OMEGA thermocouple calibrator.

5.1.3   CCD Flux Mapping

Complete characterization of the solar furnace system requires accurate mapping of the solar flux at the focal plane in addition to total power delivery. Accurate flux maps are used to determine total and peak concentration ratios for the furnace and can also be used to characterize heliostat panel alignment and concentrator performance vs. simulations.

To provide the required flux maps for the USC solar furnace, a CCD camera based flux mapping technique was developed similar to those described in the literature. A typical flux mapping system consists of a CCD camera, a lambertian surface, and a means of calibration. When taking measurements, the solar furnace output strikes the lambertian target. The reflected image is captured with the CCD camera and the local pixel intensity of the image is ultimately converted to incident solar flux at the imaged location using a calibration factor.

Existing systems produce this calibration factor using either a flux gauge installed within the target [100] or a point radiometer [101, 102] to provide a real time flux value for a given location. In contrast, the USC system utilized a bench-top black body source to provide a fixed CCD calibration factor for a given camera and lens assembly. This simplified the experimental set up but required a fixed system geometry and fixed components throughout testing.

Two CCD camera assemblies were used for the USC solar furnace to provide two different fields of view and two different focal lengths. The cameras used were monochromatic CCDs using the Sony ICX445 CCD sensor coupled to a 12 bit ADC and were selected for both CCD

linearity and sensitivity at the IR wavelengths of interest. Each camera was fitted with a 35mm lens and a 980 mm bandpass filter to both reduce total intensity and avoid wavelengths affected by atmospheric absorption. The lenses were locked at an aperture of f/22 and focal lengths were fixed at 0.43 m and 1.40 m for the "short" and "long" CCD assemblies respectively. The "short" CCD provided a field of view of 57 mm by 43 mm and the "long" CCD provided a field of view of 53 mm x 71 mm. Images were taken with constant camera settings, except for exposure time, and the 1296 x 964 pixel output of the CCD chip was down-sampled to record 640 x 480 pixel images.

Calibration

Each camera was calibrated by imaging a blackbody cavity across multiple temperatures. Cameras were set up so that the aperture for the blackbody cavity was at the designated focal length with distance confirmed by imaging a reference grid and comparing the result against the desired field of view. Once this was established, multiple images were taken of the black body cavity across a range of temperatures from 900 to 1200 $°C$ ensuring sufficient time for the blackbody to reach equilibrium at each temperature and scaling the exposure time of the CCD to ensure that images were unsaturated.

Calibration images were processed by masking the location of the blackbody aperture and determining the average pixel intensity per microsecond of exposure time ($counts/\mu s$). At each temperature, the black body radiation emitted from the cavity was calculated to get an estimated irradience value at the target wavelength of 980 nm. This irradiance value and the pixel intensities across multiple temperatures were then combined to produce a final calibration factor for the CCD of $counts/\mu s$ vs. spectral irradiance (W/m^2-nm).

It is important to note that since the geometry of the problem is fixed, the calibration factor for the CCD is simply chip response vs. estimated intensity at the blackbody surface at pre-determined wavelength as opposed to a quantification of energy actually striking each pixel of the
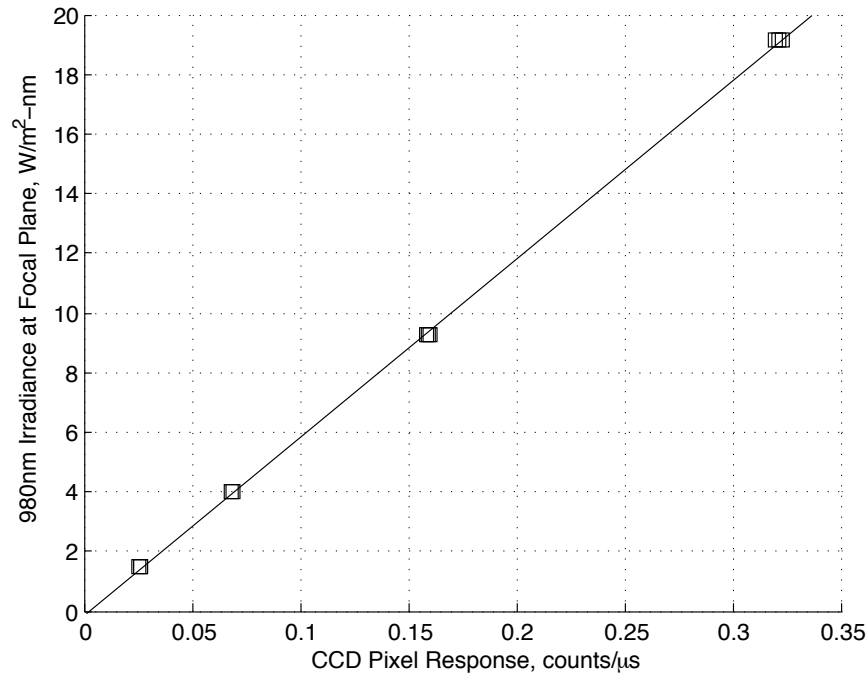
76

Figure 5.4: Calibration data for the "long" CCD produced from 36 calibration images at black body temperatures between 900 and 1200 $^\circ C$. The calibration results in a calibration factor of 59.7 $counts/\mu s/W/m^2\text{-}nm$

CCD. Calibration data for the "long" camera assembly is given in Figure 5.4 and demonstrates the expected linear relationship between CCD response and irradiance at the imaged location.

Flux Calculation

Flux map images were taken by placing a quasi-Lambertian target at the plane of interest and capturing an image of reflected sunlight using one of the previously calibrated CCDs. The measured distance between the focal plane and the camera assembly were confirmed by imaging a grid pattern to check the camera field of view. Camera settings were also kept identical to those used the calibration process. Image exposures were set to ensure that no regions of the CCD were saturated.

The first step in processing flux map images is to convert the intensity of each pixel to an approximate blackbody spectral irradiance at 980 nm for that location using the $counts/\mu s$ vs.

77

spectral irradiance (W/m^2-nm) factor determined during the calibration process. This results in an intensity map for a specific wavelength with an assumed black body source.

Since the actual image is produced by reflected solar spectrum, this intensity map must be converted. The blackbody irradiance values at 980 nm are compared to the irradiance at 980 nm of the ASTM G-173 reference solar spectral irradiance provided the National Renewable Energy Laboratory (NREL). This spectrum represents the average the solar radiation intensity per wavelength at an approximate solar insolation of 900 W/m^2.

The black body intensity map is divided by the ASTM G-173 reference value of 0.57 W/m^2-nm at 980 nm yielding a pixel by pixel map of reflected sunlight measured in "suns". For example, if a given pixel measured a black body spectral intensity of 57 W/m^2-nm, comparison with the ASTM G-173 spectrum would result in local intensity of 100 "suns" in the region imaged by that pixel. Since a single "sun" represented in the ASTEM G-173 spectrum has a total power of 900 W/m^2, the intensity of each pixel is multiplied by this value giving the desired solar flux map at the lambertian target in units of W/m^2. Finally, the flux map image is divided by a reflectivity value to account for reflection losses in the lambertian target yielding the final flux map for the system.

The reflectivity used for the lambertian target is set at 71% matching total power measurements in the flux map data to those recorded by the commercial power meter. The lambertian target was created by covering an aluminum sheet in multiple layers of matte white commercial spray paint so this reflectivity is within the range of expected values. Noting the uncertainty of power meter measurements, it is expected that flux mapping calculations have a minimum uncertainty of ±5%.

The flux mapping system was initially tested using the Fresnel lens-based development furnace to both quantify the performance of the heliostat and find the optimal location for experimental performance. The two flux maps given in Figure 5.5 show the output profile of the furnace at both the geometric focus of the lens and at the region of peak intensity approximately 3 cm closer to the lens. Flux maps at the geometric focus show low total concentration ratios as well as two separate
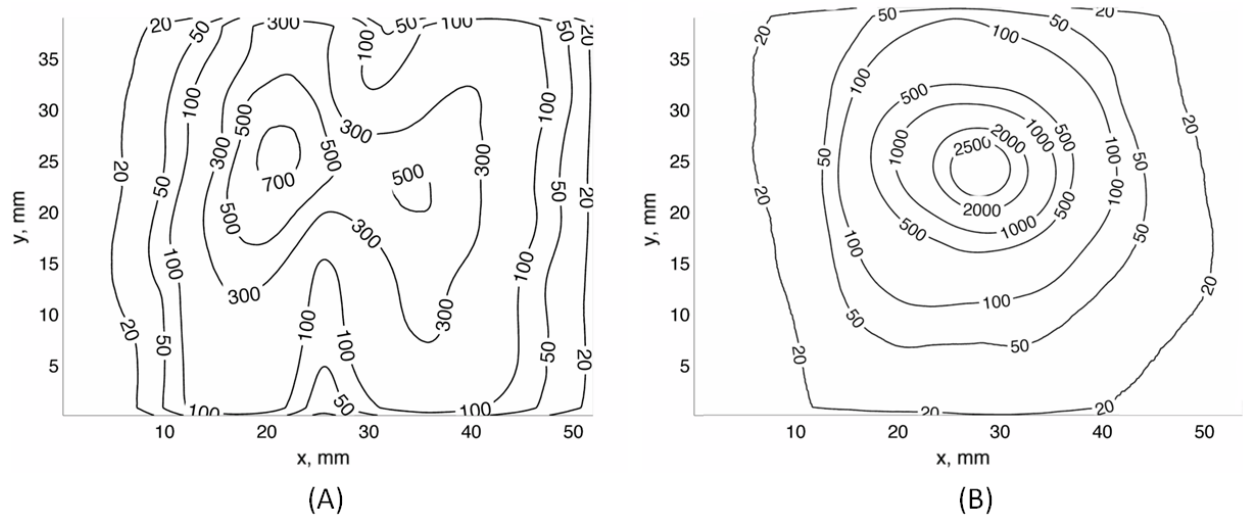
78

Figure 5.5: Solar flux profiles taken for the Fresnel Lens solar development furnace at the (A) geometric focus and (B) the location of peak performance. Note that at the geometric focus, misalignment of the heliostat panels is visible effectively creating two images. Units displayed on the contours are the number of suns which is equivalent to the concentration ratio.

approximately rectangular lobes. These regions are a result of misalignment in the heliostat panel assembly and were ultimately eliminated by adding more bracing to the panels and ensuring that they were co-planar.

The flux profile in the region of peak intensity demonstrates the performance gains that can be achieved with accurate flux mapping at various distances from the lens. Due to aberrations and alignment inaccuracies, the geometric and "visual" focus points are often not the best performing region. A series of images mapping the output of the Fresnel lens ultimately showed peak regions with concentration ratios exceeding 2500:1 representing a more than three fold increase in peak concentration ratio vs. the geometric focus.

79

5.2   Final Design

Transitioning to molten silicon experiments required total power delivery and concentration ratio improvements over the existing Fresnel lens based development furnace. Initially, a custom manufactured solar concentrator was targeted using either a single large glass parabolic mirror or a large segmented array approximating an ideal parabolic concentrator. However, it was found that custom manufactured optics on the scale required (concentrator area $> 1\ m^2$) were both cost and schedule prohibitive resulting in a search for COTS solutions. Ultimately, a modular spherical mirror supplied by Display and Optical Technologies Incorporated (DOTI) of Georgetown, Texas was used as the primary concentrator and provided sufficient performance for molten silicon testing despite losses from spherical aberrations.

The USC solar furnace is a two stage design, diagrammed in Figure 5.6. In addition to developing a new primary concentrator, improvements in the heliostat were required to both increase coverage for the larger concentrator and reduce flatness errors witnessed during CCD flux mapping development.

5.2.1   DOTI Solar Concentrator

The primary concentrator for the USC solar furnace is an array of four spherical mirrors that are arranged to form a single spherical concentrator with an effective diameter of $1.78\ m$ and radius of curvature of $3.15\ m$. The concentrator assembly was manufactured by Display and Optical Technologies Incorporated (DOTI) due to their expertise in creating large reflectors and their existing production capability. While parabolic concentrators are ideal for solar furnace applications, tooling costs for new optics were cost prohibitive and spherical reflectors were required in order to gain sufficient scale using existing inventory. The individual mirrors that make up the concentrator were sourced from DOTI's Wide Angle Collimated (WAC) display program and are a standard component manufactured for use as high performance flight simulator displays. Adapting these
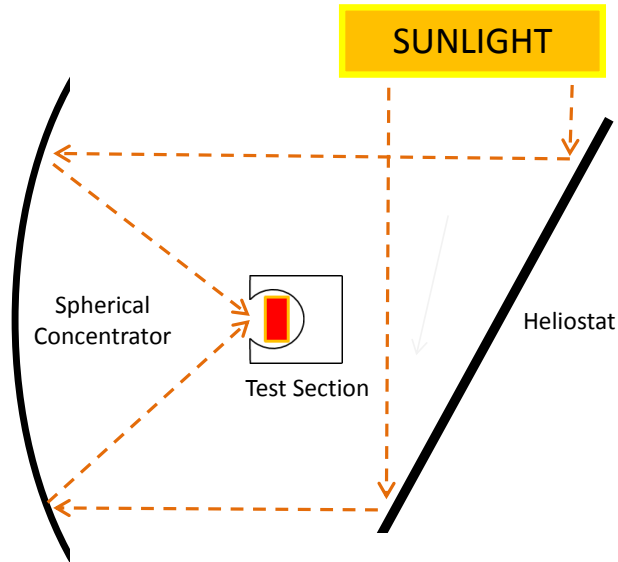
80

Figure 5.6: Path diagram for a two stage solar furnace using a spherical concentrator.

readily available mirrors into the final USC solar concentrator produced significant cost savings as the only custom design work was the fabrication of the mounting structure.

Each concentrator facet is an approximately $1\ m$ x $1\ m$ square aluminized first surface mirror on $13\ cm$ thick glass substrate. The mirrors are specified with a mean slope error of $180\ arcseconds$ from ideal and a proprietary silicon dioxide based coating results in a reflectivity approaching 90% when weighted against the solar spectrum. Mirrors were shipped with steel mounting rings cemented to the rear surface containing three threaded rods used for both mounting and alignment.

The steel mounting structure was custom manufactured by DOTI and included a rail system allowing for the entire mirror assembly to translate along the optical axis. The center of the mounting structure contained a small optical plate to mount diagnostics. After mounting rails were installed and aligned, a diode laser was installed on this optical plate to define the optical axis of the solar furnace assembly. This optical plate was also used to mount CCD flux mapping diagnostics as well as a standard video camera with an attached neutral density filter to image the experimental area during testing.
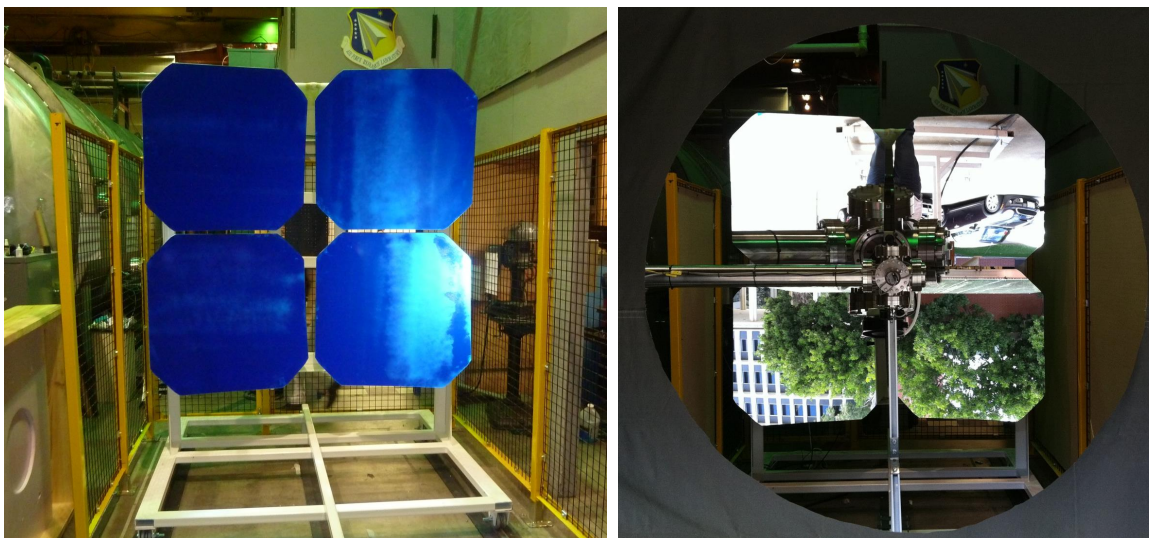
81

Figure 5.7: Photographs of the mirror array during construction (left) and as seen through the 70 inch aperture curtain. The mirrors are blue during construction due to a protective plastic film applied before shipment. Note the testing chamber seen in the middle of the concentrator array in the photograph on the right.

The completed mirror array, shown in Figure 5.7, was aligned using a point source placed at the radius of curvature along the central optical axis. Each mirror was adjusted so that its reflected image collapsed onto the point source resulting in a single unified optic.

Due to the influence of spherical aberrations, it was necessary to create an aperture for the solar concentrator. At the extremes of the mirror array, sunlight is reflected with an effective concentrator radius of over 1.4 m and the resulting aberrations are unmanageable. Currently, a curtain has been installed with an aperture of 1.78 m (70 in) resulting in a usable concentrator area of approximately 2.3 m^2 when taking into account the central area used by the diagnostic mount and blockages by the testing chamber.

5.2.2 Heliostat Improvements

To accommodate the new larger solar concentrator, the heliostat was expanded and a new 2.4 m by 3.7 m mirror panel was constructed. The original central mirror mount was removed from the

Figure 5.8: Photograph of the USC heliostat mirror array.

heliostat and a new framing assembly was built using aluminum I-beams and a central steel plate mounted to the heliostat drive components. This framing system can be seem in Figure 5.3. Three 2.4 m x 1.4 m aluminum honey comb panels were fixed to to the aluminum mirror frame and the assembly was adjusted to be co-planar. Finally, six 2.4 m x 2.4 m second surface float glass mirrors were mounted to the honeycomb panels using spray adhesive to produce the finished panel in Figure 5.8. The larger individual mirrors reduced flatness errors compared to the mirror tiling used in previous heliostat iterations.

The total size of the new mirror array was a trade between concentrator requirements and available experimental space. The optical axis laser from the concentrator array was used to properly locate the center of the heliostat drive and the heliostat was permanently mounted outside the building to accommodate the larger mirror panels. The location of the heliostat ($34.020116°$, $-118.287748°$) was determined using a high accuracy GPS with a radial uncertainty of $1.3\ m$.

The final upgrade to the heliostat was replacement of the existing rheostat based angle sensors with digital angle encoders, improving tilt sensing uncertainty to $0.0045°$ on both axes. To align
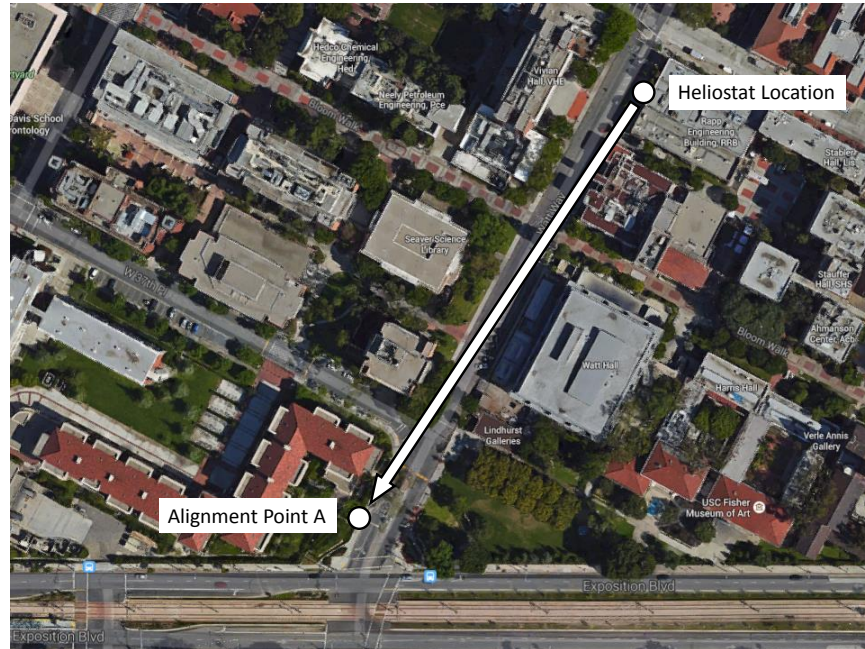
83

Figure 5.9: Satellite photograph (Google Maps) of the USC campus illustrating the heliostat location as well as the azimuth alignment vector.

the azimuth axis of the heliostat, a second location on the USC campus ("Point A") was determined within an uncertainty of 20 cm via GPS. An azimuth vector was established between the heliostat and "Point A", as shown in Figure 5.9, with an uncertainty of $0.27°$. A laser was shone from "Point A" to the heliostat and the heliostat mirror panel was used to reflect the laser back upon the source. The heliostat was then considered aligned to the reference azimuth vector.

Next, the azimuth vector for the solar concentrator was set by rotating the heliotat and reflecting the optical axis laser installed within the concentrator back upon itself. The relatively large uncertainty in the azimuth vector is due to the uncertainty of the heliostat location. The surrounding buildings result in a weak GPS signal and the accuracy of this measurement can be improved by using a GPS device capable of simultaneously referencing the GPS and GLONASS systems. The current accuracy, however, is sufficient due to the use of open-loop control. The altitude axis of the heliostat was calibrated using a machinist's level.
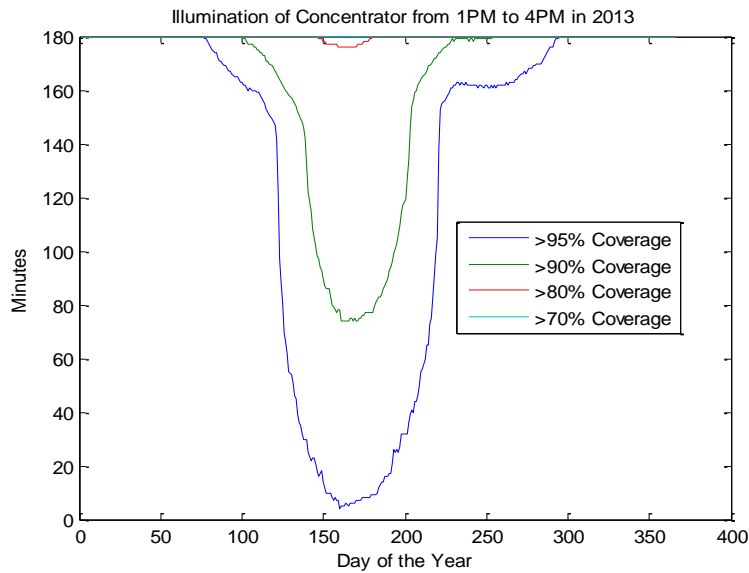
Figure 5.10: Solar concentrator coverage as a function of day of the year. Heliostat size and placement limitations result in reduced coverage from May-July. Coverage is still sufficient for year-round experimental operations.

The reflected sunlight from the heliostat is effectively a projection of the tilted mirror assembly onto the plane of the concentrator and the heliostat is unable to provide full coverage during instances of extreme tilt due to total size limitations. Additionally, the placement of the solar furnace facility in an urban campus only allows for approximately 4 hours of sunlight coverage per day. Figure 5.10 shows the differences in coverage vs. time during the year and shows that with the current design, winter testing is ideal. However, there are still windows of full coverage during the summer.

5.2.3 Characterization and Current Performance

The current solar furnace facility was characterized for total output power as a function of solar insolation and individual component efficiencies. Because the DOTI solar concentrator array is
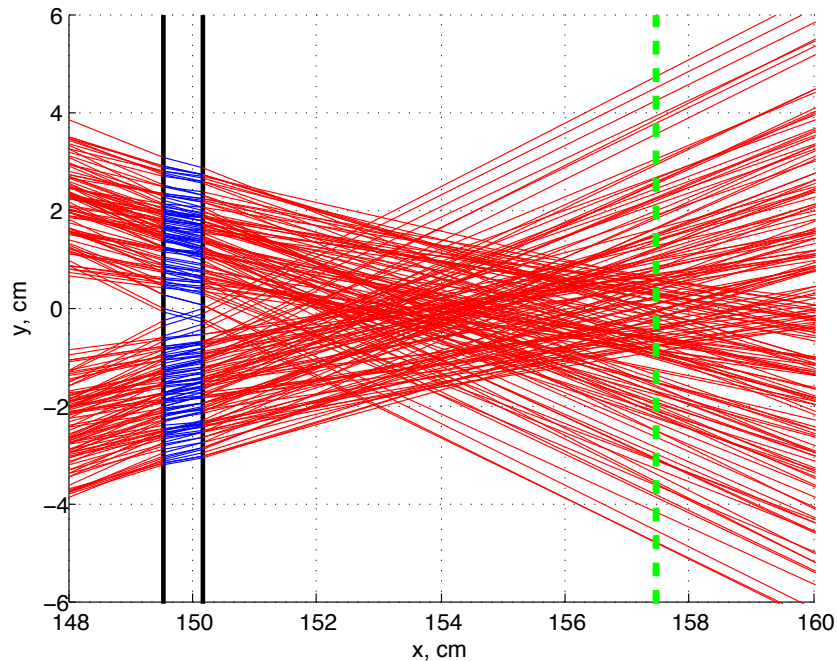
85

Figure 5.11: Ray trace simulation (with only 200 rays for visibility) of the focal area for the DOTI mirror array. Note the inclusion of the quartz window at an axial distance of 149.9 cm and the geometric focal length at 157.48 cm as noted by a dotted green line.

spherical, special attention must be given to the effects of spherical aberrations. A ray trace program (2-D with weighting to approximate 3-D performance) was written in-house to provide a predictive model for concentrator output and determine the optimal location for experiment placement. This program takes into account the random slope error of the reflector, heliostat pointing and flatness error, incoming solar angle distribution, blockage from the test chamber, and the influence of the quartz window.

Figure 5.11 shows the incoming ray profile of the solar furnace near he geometric focal point with a 1.78 m aperture. It can be seen that due to spherical aberrations and manufacturing errors, the effective spot size at the geometric focus is approximately 9 cm in diameter. At different locations however, there are areas of increased flux density which can allow for reasonable concentration ratios provided that peripheral rays are neglected.
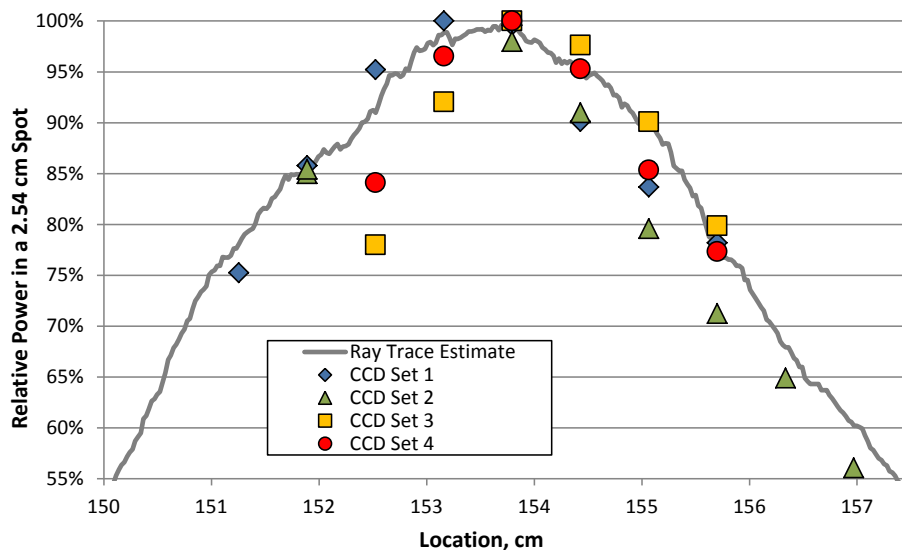
Figure 5.12: Relative power delivered to a 2.54 cm diameter spot vs. distance from the solar concentrator as predicted by ray tracing and experimentally measured via CCD flux mapping. Note that the ideal location, both predicted and measured, is approximately 3.8 cm back from the geometric focus at 157.5 in.

To determine the optimal experimental location, the power delivered into a 2.54 cm spot was simulated and experimentally recorded using the CCD flux mapping technique for multiple focal planes in the region shown in Figure 5.11. Figure 5.12 gives the relative power vs. distance for the concentrator and indicates that the optimal experimental location is approximately 3.8 cm back from the geometric focus noting that the predicted and experimentally measured locations coincide. At this location of best performance, flux maps given in Figure 5.13 indicate peak concentration ratios in excess of 4000:1 and approximately 90% of total power at the plane included within a 2.54 cm diameter spot.

The end-to-end system efficiency of the USC solar furnace is relatively low at approximately 40%. Table 5.1 lists the individual component efficiencies for the furnace and their relevant contributing factors. The heliostat and the quartz chamber window are the least efficient components of the system since they suffer from both transmission and reflectance losses. The heliostat, which

87
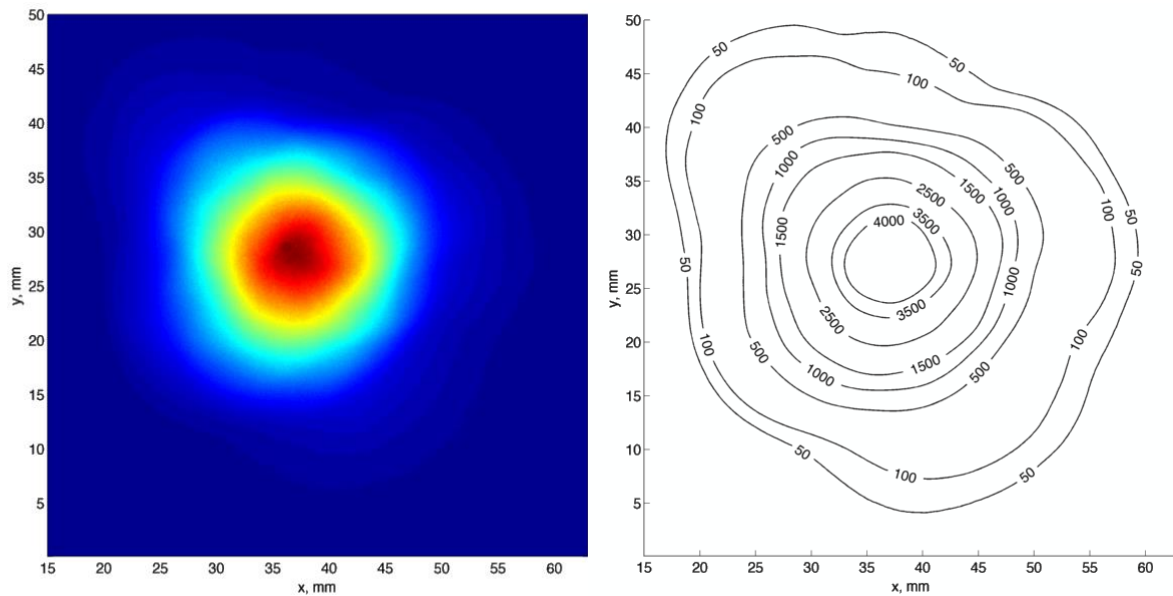
Figure 5.13: Flux maps taken at the experimental location for the USC solar furnace. Iso lines are given in number of suns.

uses commercial second surface soda-lime glass mirrors, is not optimized for solar reflection and represents the weakest component in the system. The quartz window is also a major loss contributor despite a high transmittance in the solar spectrum due to reflection losses brought on by the relatively steep incident angle of rays from the solar concentrator. For future testing, it is possible to substantially raise the performance of the furnace facility by replacing the heliostat mirrors with higher cost first surface mirrors and employing a secondary concentrator to achieve higher concentration ratios.

Despite the low total system efficiency, power levels sufficient for molten silicon experiments are possible with the current furnace design. Figure 5.14 gives the power delivery to a test section vs. local direct-normal insolation and acceptable spot size. This data has been confirmed utilizing commercially available high flux laser power meters and scaled against measurements from an Eppley Pyrheliometer.

Table 5.1: Component efficiencies of the USC solar furnace

| Component	Approx. Efficiency	Contributing Factors
Heliostat Mirrors	68%	Reflection Losses
		Transmission Losses
		Weathering
		Solarization
		Surface Imperfections
		Dirt
Concentrator Mirrors	90%	SiO_2 Coating Transmittance
		Aluminum Reflectivity
Quartz Window	73%	Reflection Losses
		Transmission Losses
1" Acceptance	90%	Spherical Abberations
		Experimental Design
Total	**40**%	
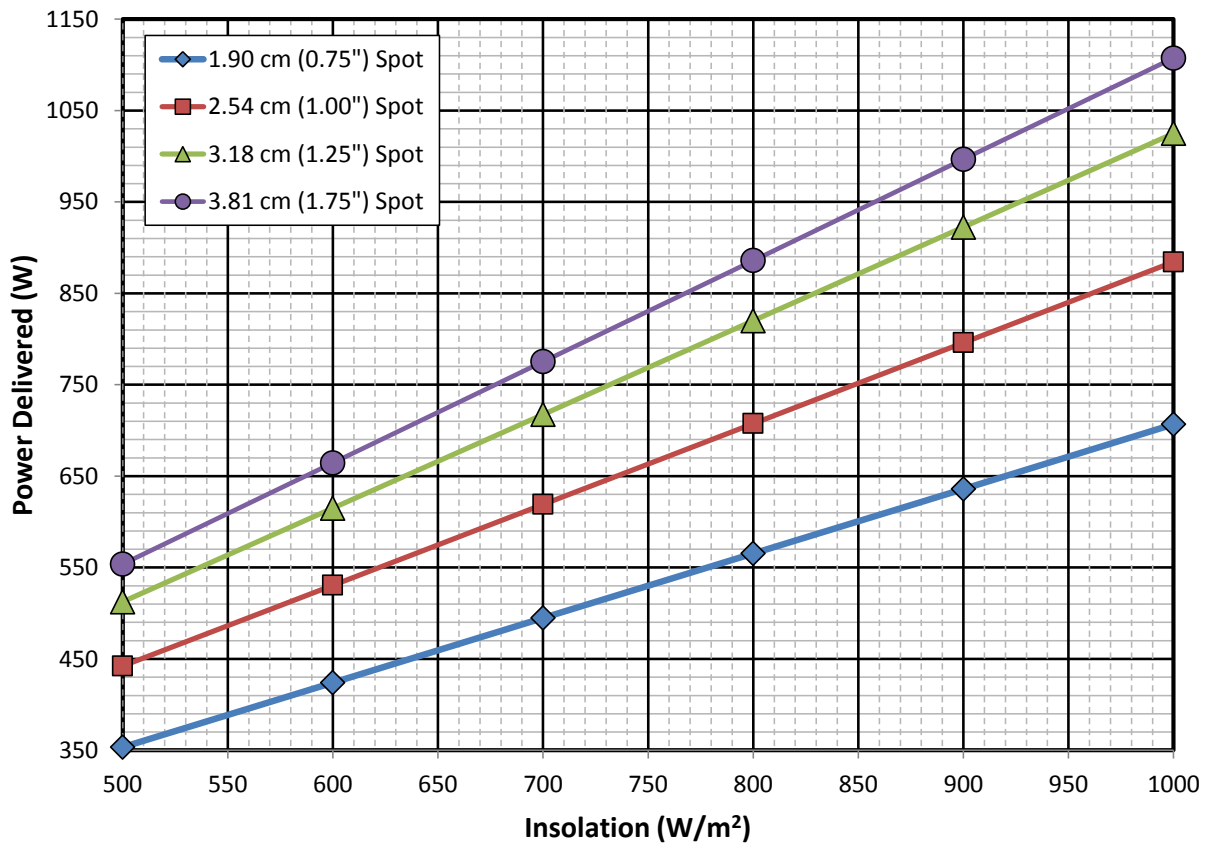
Figure 5.14: Power delivery vs. insolation for the USC solar furnace as a function of acceptable spot size. Values include losses from the quartz chamber window. Typical insolation at the facility is between 750-950 W/m^2 depending on atmospheric conditions.

<div align="right">

Chapter 6

</div>

Material Studies and Initial Experiments

Material studies and initial solar furnace experiments were performed concurrently during solar furnace development to identify a reliable experimental condition for melting silicon. A literature review of material compatibilities succeeded in identifying potential container materials for both silicon and boron. Tube furnace tests were conducted validating the short term compatibility of molten silicon with boron nitride and graphite. Early solar furnace tests were designed using a 0-D thermal model for a test article in a radiation shielding cavity. The results of these tests did not produce molten silicon. However, they did drive the creation of an in-house 2-D axisymmetric model leading to the ultimate solar furnace experimental series using cylindrical crucibles.

6.1   Material Studies

The use of latent heat phase change materials requires storage containers that are both chemically compatible and structurally sound at the PCM melting temperatures. Identifying suitable containers for molten silicon is simplified due to the relatively large quantity of industrial research from the manufacture of silicon wafers. In contrast, experiments to-date studying liquid boron have been primarily concerned with simply creating the material as opposed to thorough investigation of long term material compatibilities. Even though boron experimentation is out of the scope of

this research, material compatibility information is still included here for completeness and for the reference of future experimental designers.

6.1.1 Boron Compatibility

A literature review has indicated that molten boron has been created in the presence of refractory metals, graphite and various ceramics. In the case of refractory metals, specifically tungsten and tantalum, direct contact with molten boron has resulted in limited success during effusion cell testing for vacuum vapor deposition [103, 104, 105]. These studies measured contamination in the thin films themselves as opposed to the bulk boron sample, but it can be inferred from published results that molten boron actively attacked tungsten cells and that the purity of films produced using tantalum cells was a function of favorable vapor pressures for pure boron versus tantalum boride contaminants [106, 107]. Molybdenum has not been used in experimental molten boron testing but contamination is likely due to the instability of molybdenum borides well below the melting point of boron [108]. Boron sample contamination when using a refractory container appears probable, however it is unclear if certain high temperature borides might produce a protective layer preventing further contamination (as in the case of aluminum oxide on aluminum) or allow for further degradation with time (as with rust on iron).

Graphite was used experimentally as a molten boron crucible material by Stout, et al. [109]. This testing yielded heavy boron carbide contamination of the bulk sample, indicating that solid boron carbide did not remain at the boron-graphite interface, but rather moved through the molten boron mass. It is important to note that the contamination process began only when the boron was in the liquid state, providing an example of increased reactivity after phase change.

Due to contamination issues with graphite and the refractory metals, ceramics, particularly boron nitride (BN), emerge as the predominant crucible material for containing molten boron. Multiple studies cite negligible contamination of a boron sample melted in contact with BN, which

92

is attributable to BN's low reactivity at high temperatures and a resistance to attack in a boron-rich environment [109, 110, 111, 112]. Additional experimental considerations, however, must be made when using BN due to its strong tendency towards dissociation into liquid boron and nitrogen gas at temperatures above 2300 K [113]. Dissociation can be prevented by maintaining a system pressure above the equilibrium pressure of dissociated nitrogen and it is estimated that this pressure will be between 0.1 and 10 $torr$ (13-1300 Pa) [114, 115]. Previous experimental efforts have maintained a suitable system pressure by operating in inert gas environments, or in the case of Stout et al., by sealing the boron nitride in a graphite vessel and allowing dissociated nitrogen to pressurize the container and prevent further decomposition. As an alternative to BN, Holcombe et al. reported the use of halfnium diboride containers with no mention of contamination issues. Due to the extent of reported BN use with favorable results, this work suggests BN as the container material for a future molten boron system.

6.1.2   Silicon Compatibility

Using molten silicon as a PCM also requires careful selection of a container material. However, a large body of research exists due to industrial silicon processing. Molten silicon is routinely handled in the semiconductor industry using silica (SiO_2) crucibles for single crystal silicon production and graphite crucibles for the industrial manufacture of large solar grade multicrystaline silicon ingots. In the Czochralski process for producing single crystal silicon, molten silicon reacts with the SiO_2 crucible to produce SiO which then evaporates from the bulk material [116]. While this is acceptable during the relatively short crystal pulling process, the Si-Si0_2 reaction prevents the use of SiO_2 for long-term storage applications. In the case of graphite crucibles, minimum sample contamination is reported when operating in an inert environment provided that the graphite meets certain porosity requirements to prevent wetting. Ciszek and Schwuttke state that carbon contamination on the order of 20 ppm is possible using graphite crucibles provided that the graphite density is > 1.75 g/cc and that the graphite grain size is < 50 μm [117].

93

BN also appears to be an acceptable molten silicon container providing synergy with future molten boron testing and removing concerns about high temperature graphite reacting with other system materials. Drevet et al. states that molten silicon in contact with BN will react to form a thin layer of silicon nitride (Si_3N_4), but this reaction is self limiting, likely due to boron saturation of the liquid silicon bulk [118]. It is expected that a small amount of boron within the silicon sample will have little effect on solidification. Wang et al. states that for boron concentrations below 2%, defect free silicon crystals are expected with boron substitutions which should minimally affect the latent heat release [119]. It is important to note, however, that these assumptions are based on relatively small molecular dynamics models. In addition to BN, Si_3N_4 is used as a release agent for silicon processing and may be a usable crucible material itself. However, a lack of machineability makes its use impractical in this work.

Initial tube furnace experiments were performed with molten silicon in both graphite and BN crucibles to ensure experimental compatibility. The first set of tests used both bare graphite and BN lined crucibles loaded with 99+% pure, 325 mesh amorphous silicon powder that were then placed in the tube furnace and held at 1550 °C for approximately 12 hours under an argon purge. After sectioning the crucibles, it was seen, contrary to expectations, that the silicon had formed into multiple smaller beads as opposed to a single silicon mass. It was believed that this behavior was due to contamination of the silicon powder by SiO_2. Since the particles were small (44 μm and smaller), the thin SiO_2 layer formed on the outer surface of the particles was significant with respect to the total silicon mass. A second round of testing alleviated this problem by switching to 99.9999% pure 1-3 mm silicon chips. These tests, shown sectioned in Figure 6.1, were similarly held at 1550 °C for 12 hours and the behavior of the molten silicon was as expected. Significant wetting is shown in the bare graphite crucible which is in line with predictions made by Ciszek about graphite suitability. The NAC-500 graphite used in these tests has a grain size well above that suggested and an average density slightly below the requirements for non-wetting behavior. In the case of the BN lined crucible, there was minimal wetting of the BN surface. For both test sections
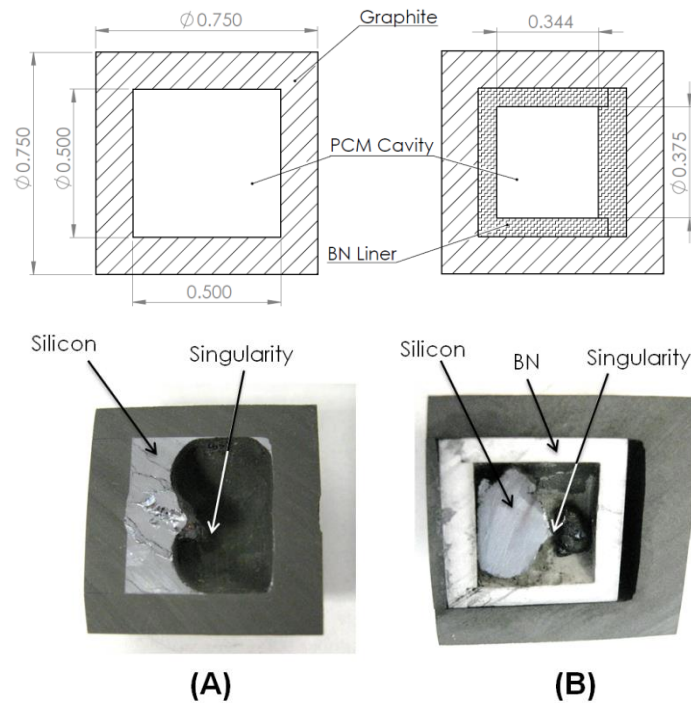
94

Figure 6.1: Cut-away diagrams and photographs of (A) a bare graphite crucible and (B) a graphite crucible with a BN liner as tested in a high temperature tube furnace. The photographs were taken after heating silicon chips for 12 hours at 1550 $^\circ C$. Note that the grey contamination inside the BN sleeve is a result of coolant flow during the cut-away process. Dimensions given in inches.

there appears to be no evident short term damage, but longer duration tests will be required in the future to assess behavior across multiple cycles. These tests were originally scheduled and test articles were created, however, budget cutbacks prevented the completion of any long term testing.

It also must be noted here that Figure 6.1 shows the formation of freezing point singularities in the re-solidified silicon. These semi-conical structures are produced by the combined effects of surface tension and volumetric expansion during freezing [120]. Silicon is unique in that is is one of the few materials that expands during freezing and the resulting volume change of approximately 10% poses significant challenges if silicon is to be used as a PCM [121]. In the existing literature

concerning silicon as a thermal energy storage media, there is no mention of this expansion issue. As a result, this was not a design driver until late in this research campaign.

6.2   Preliminary Solar Furnace Tests

The first series of experiments were performed using the Fresnel lens based development furnace with the goal of simply producing liquid silicon using concentrated sunlight. The design driver for these tests was a paper published in 1990 by Steinfield and Fletcher which presented a closed form solution for the temperature of a solid spherical solar furnace test article in a reflecting spherical cavity [122]. Steinfeld's paper calculated receiver temperature by performing a radiation balance between a centrally located test section, a truncated spherical radiation shield, and a circular entrance aperture. A diagram of the modeling geometry is reprinted in Figure 6.2 and shows that for modeling purposes, the centrally located receiver was divided into "front" (A_{1f}) and "back" (A_{1b}) sections effectively dividing the system into four regions. Surface to surface radiation was considered in the model and the paper contained Monte-Carlo ray trace results supplying view factors for the receiver regions after reflection in the spherical radiation shield.

Steinfeld suggested the use of graphite for the test section and aluminum for the radiation shields. Due to high thermal conductivity of both materials, all regions of the model were assumed to be isothermal meaning that the front and back temperatures of the central receiver were identical. Additional assumptions in the model state that all incident incoming solar radiation strikes the receiver directly on the surface A_{1f} and that surface A_{1b} is positioned so it is hidden from the aperture resulting in a a view factor $F_{3-1b} = 0$. For the mathematical formulation of the model and the supplied solution, the reader is directed to the original paper.

An experimental apparatus was constructed in an attempt to achieve molten silicon temperatures by approximating the configuration in Steinfeld's model. Figure 6.3 shows the overall system geometry including a "bullet" shaped test section, spherical aluminum radiation shields, support
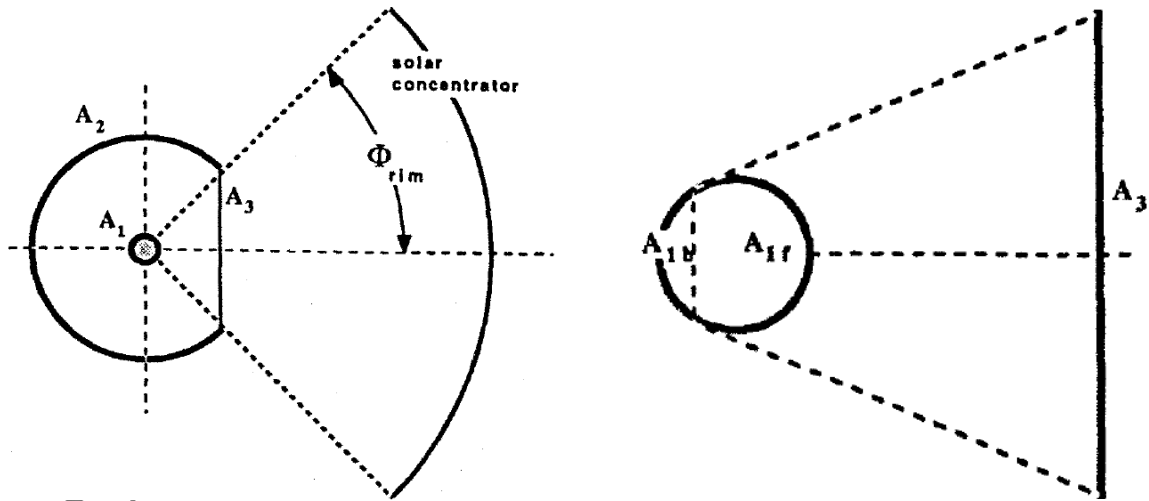
96

Figure 6.2: Basic three body modeling geometry for an isothermal spherical test section in a spherical radiation shield. Note that the isothermal test section is broken into two sections to aid in the formulation of the radiation balance. Diagrams reprinted from Steinfeld and Flecther [122].

structure, and the tantalum sheathed Type C thermocouple which served as a the primary temperature diagnostic and sting mount for the centrally located test section. Since the Steinfeld model required that all incident solar radiation strike the receiver, the minimum reliable spot produced by the Fresnel lens set the test section diameter at 0.75 in. "Bullet" shaped crucibles were used as opposed to spherical due to the limits of in-house machining capability.

The outer diameter of the radiation shielding was determined by the availability of aluminum hemispheres since model results were invariant with respect to shield size provided the entrance angle remained constant. Three inch diameter aluminum hemispheres were sourced and polished in-house using a lathe to create the necessary reflective surface. Rough sanding was first performed with sand paper ranging from 400-2500 grit in 200 grit increments. The sanded aluminum surface was then wet polished using 3M Zona polishing paper decreasing in grit size from 15 - 1 microns. Finally, a finishing pass was performed using Mother's Billet Aluminum Polish. The entrance rim angle of 40° was also set by the Fresnel lens input geometry and was created by sectioning a
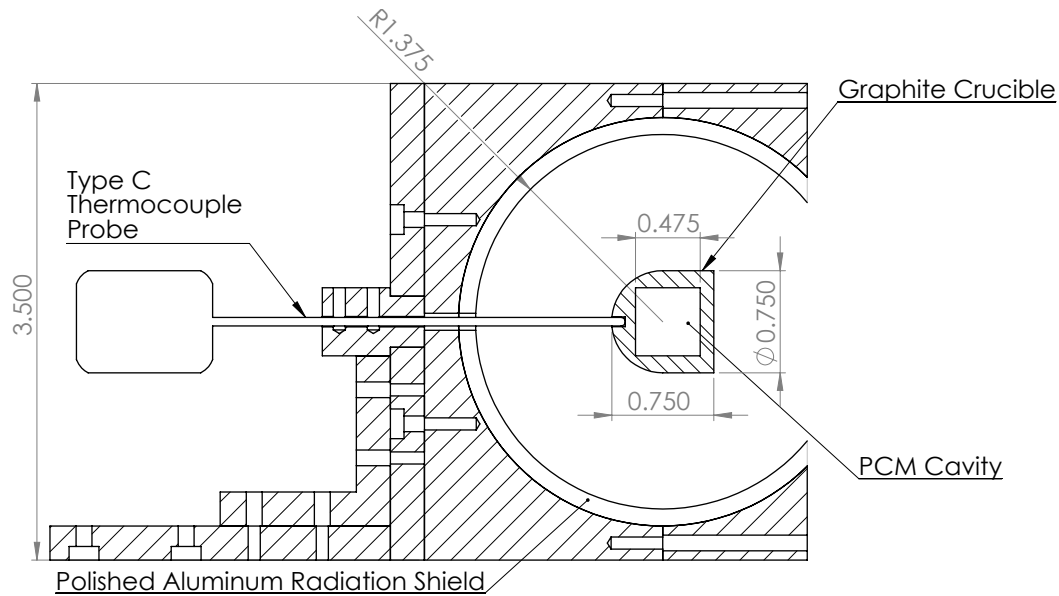
97

Figure 6.3: 2-D cutaway schematic of the initial solar furnace test assembly showing the spherical radiation shield, support structure, thermocouple sting mount and "bullet" style crucible. Note that for pure graphite tests, the PCM cavity was removed and the thermocouple was placed in the center of the test section. Dimensions given in inches.

completed hemisphere. Figure 6.4 shows the completed radiation shield along with the rest of the test apparatus.

With the Fresnel lens furnace and the shielding system discussed above, test articles made from solid graphite (no PCM cavity) were able to achieve molten silicon temperatures with an estimated power input of 240 W. This power input includes both the estimated direct input to the crucible surface as well as sunlight that initially misses the crucible yet enters the shielding cavity agreeing with the Fresnel lens characterization values for the observed solar insolation within 5%. Cooling curve analysis of the experimental results suggested a 55% reduction in radiation losses via the radiation shielding.

The results of these tests showed that molten silicon temperatures could be reached. However, they were not in agreement with model predictions. Steinfeld's model suggested a 70% reduction in radiation losses (with a shield reflectivity of 0.8) and a minimum required power of 188 W to
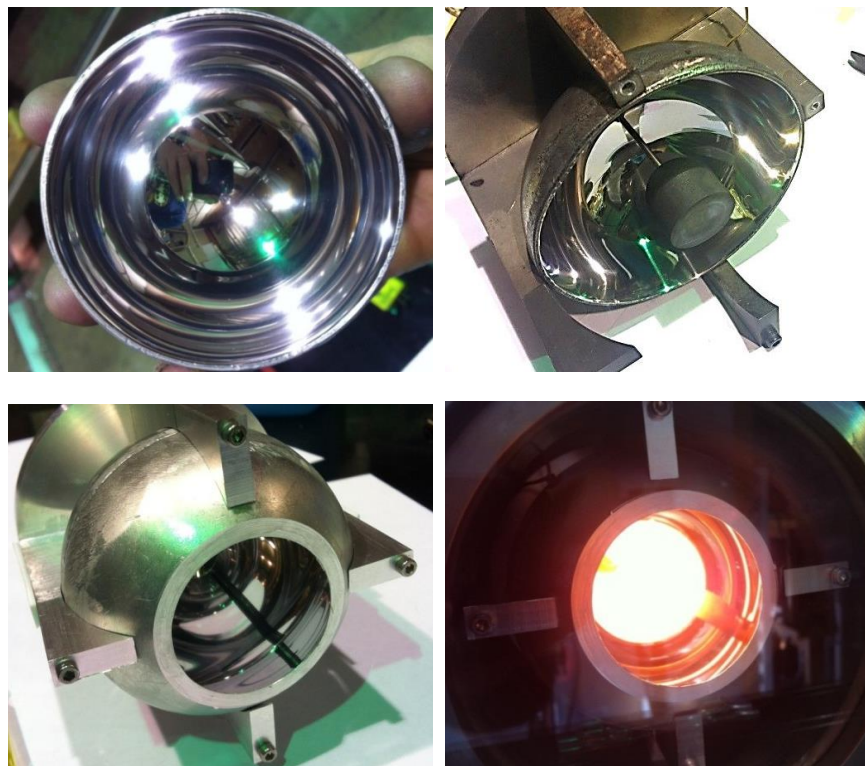
Figure 6.4: Photographs of the radiation shielding test assembly. Clockwise from top left: Radiation shield half after polishing, graphite test article mounted on thermocouple sting mount, assembled test article, crucible immediately after removing solar furnace power.

reach 1680 K. It was expected that the experiment would require more power and exhibit reduced shielding efficiency since the experimental test sections have 22% more surface area and are non-spherical. This geometry increase suggests that 83% would be required over that predicted by Steinfeld's model. However, experiments demonstrated molten silicon temperatures with only a 28% power increase.

Despite disagreement with Steinfeld's predictions, experiments with this geometry continued since molten silicon temperatures had been experimentally confirmed. Crucibles were hollowed to create the PCM cavity shown in Figure 6.3 and small BN containers loaded with silicon chips were inserted. Throughout multiple tests, silicon within the PCM cavity showed no evidence of melting even though thermocouple measurements indicated temperatures above 1680 K. Later inspection

revealed that during these tests, a combination of thermocouple bead placement within the probe and focusing of scattered sunlight by the radiation shields was inflating true measured temperature of the crucible.

All design and testing during this series relied on Steinfeld's modeling assumption that the crucible would be an approximately isothermal body. Once a PCM and a PCM container were added to the crucible, modeling results, pyrometer and updated thermocouple data demonstrated crucible thermal gradients of 100's of K which prevented PCM melting. As a result, this series of tests was halted in order to construct an accurate multidimensional model of the system to aid in test section design.

Predictive Model

After completing initial solar furnace testing using simplified formulations to solve for experimental temperatures, disagreement with experimental values highlighted the need for a full multi-dimensional and transient solution for test section performance. Thus, an in-house model was written in MATLAB to predict test section heating and cooling. In addition to serving as a predictor for test performance, the model was also intended to assess the fidelity required in freezing kinetics models to capture essential system behaviors.

7.1   Model Geometry

The MATLAB model is a cylindrical, axisymmetric 2-D (r,z) simulation. A cylindrical geometry was selected for both ease of calculation and ease of manufacture for eventual experimental test sections. A concession was made in both the design of the model and subsequent experiments by utilizing a flat plate solar absorber as opposed to a radiation cavity. While this significantly reduced computational difficulty, it similarly reduced the thermal efficiency of test articles.

The geometry shown in Figure 7.1 gives the general scale of test sections and was initially set by using SolidWorks Simulation Professional to determine maximum experimental size. Also

shown in Figure 7.1 are the 14 adjustable regions in the model which are used to set the geometry of individual test section components as well as their materials.

Each material is modeled with fully temperature dependent properties using values primarily taken from the TPRC Data Series [123]. This is required to accurately represent the thermal inertia of the system and is especially important when considering the rapid decrease in thermal conductivity of the PCM as it transitions from liquid to solid. Further assumptions in the MATLAB model include a neglect of thermal contact resistance and thermal expansion.

7.2   Solution Method and Boundary Conditions

A fixed-grid, energy balance method is used to solve for the temperature profile as a function of time [124]. Heat trasnfer between adjacent nodes is assumed to be conduction only and the relevant conduction equations are described in Appendix A. The resulting solutions are 2-D axisymmetric transient temperature profiles.

The modeling geometry shown in Figure 7.1 is represented by a 25 x 37 grid of nodes in the r and z directions respectively at the coarsest setting. It is possible to independently set the grid spacing for each of the 14 geometry regions provided that each region contains a minimum of three nodes in both the r and z directions to accurately resolve material boundaries. Time steps are on the order of 1 millisecond resulting in a total solution time of 6-8 hours for a full heating and cooling cycle in the model. To produce the models shown in this paper, the grid was increased to 50 x 74 nodes for higher resolution in temperature maps and the time step was reduced to 0.2 milliseconds to maintain stability. Thermal performance at monitoring locations between the two models was identical showing that the coarse settings are sufficient to predict overall system behavior.

To account for the phase change process in the PCM, the "enthaply method" is used in a similar formulation to that presented in Elgafy et. al [125]. For computational nodes containing the PCM, a latent heat value is assigned and treated as a source or sink when that node is in a temperature
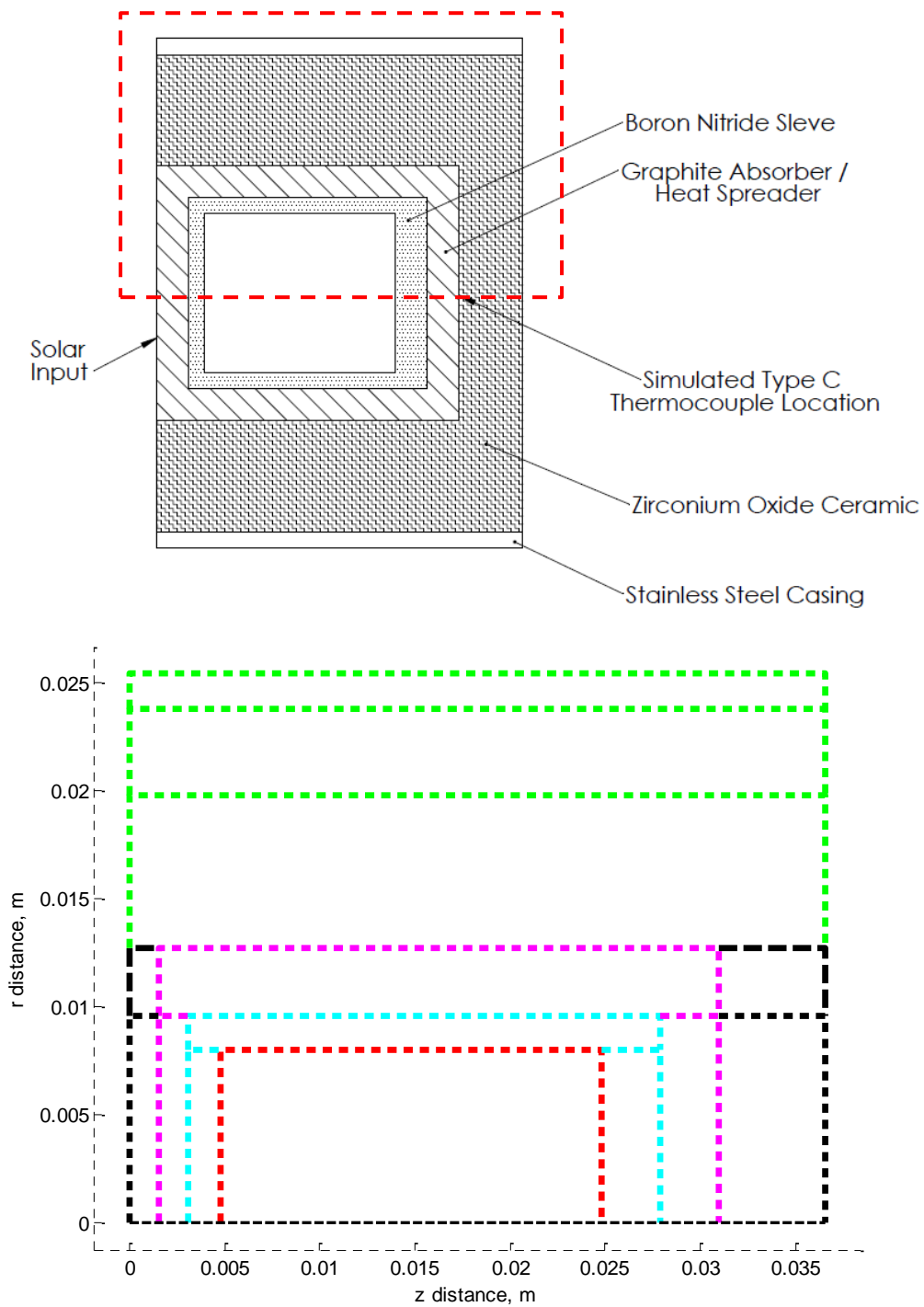
102

Figure 7.1: MATLAB modeling geometry showing both a 2D cutaway of a nominal cylindrical experimental test section and the geometric representation for antisymmetric computations. Dimensions, node spacing, and material properties can be independently set for each of the fourteen regions shown in the lower figure.

range known as the "mushy" zone. Once a node enters the "mushy zone", currently defined as $T_m \pm 0.1$ K, all energy leaving or entering the node is assigned to the phase change process and the node remains at a constant temperature. When a particular node exhausts the assigned latent heat energy during cooling, the temperature is allowed to change and sensible heat cooling resumes.

Since the model formulation is a fixed grid with fixed control volumes, motion of the PCM when in the liquid state is neglected. Additionally the model assumes a 100% fill factor at all times and ignores effects from density change during melting a freezing. Thus, this simplified treatment of the phase change process does not consider convective heat transfer within the liquid PCM.

When modeling the cooling process, neglecting convection is justified due to low thermal gradients with the liquid PCM. Sensible heat quickly dissipates from the PCM when solar furnace power is removed from the system and thermal gradients within the test section re-orient. Once the PCM reaches the melting temperature, all thermal gradients are supported by the quasi-isothermal phase change process and the remaining liquid PCM maintains a constant temperature within the "mushy zone." This very stable temperature environment and a low Prandlt number (≈ 0.02) result in Rayleigh numbers less than 10^3 denoting conduction dominated heat transfer.

For heating models, it is important to consider convection effects within the liquid PCM as this will increase the effective heat transfer rate leading to both shorter melt times and higher temperatures in the rear of the test section. For the geometry considered here, temperature gradients within the liquid PCM can be in excess of 100 K when the system is in equilibrium with the solar furnace input power. These large thermal gradients correspond to Rayleigh numbers of approximately 10^5 and it is expected that buoyancy driven flows will be established.

However, in the context of this experiment and the ultimate goal of operating in a microgravity environment, it is also reasonable to neglect convection during heating for the purposes of the MATLAB model. For the geometry considered here, increasing or decreasing the effective thermal conductivity of the liquid PCM by a factor of two results in only a <2% increase or decrease in bulk PCM temperatures. Furthermore, after the heat source is removed, the phase change process

104

dominates and container temperatures are established relative to the melting temperature of the PCM.

At the outer surfaces of the model, a radiative and convective boundary condition is applied. The natural convection boundary condition accounts for operation in the 150 $torr$ argon testing atmosphere and is approximated by published empirical heat transfer coefficient correlations for cylindrical bodies [126]. Operating in this argon atmosphere is required to prevent reaction of experimental materials as described in Section 8.1 and convection effects account for $< 10\%$ of total heat losses.

The radiation boundary condition is calculated to account for the small shielding effect provided by the vacuum chamber. Integrating radiation shielding into the model required the calculation of node to node view factors as well as integrating radiosity calculations into the finite difference solutions at the boundary.

7.2.1 Radiation Shielding Integration

Radiation shielding was included in the model with the option to model either a cylindrical or spherical shield. Radiation shielding calculations are performed via a radiation energy balance on each exterior node in a manner similar to that described in Steinfeld and Fletcher [122]. All surfaces are considered opaque grey bodies.

For all exterior nodes 1 through n, the radiosity per unit area B_n is calculated as

$$B_n = \epsilon_n \sigma_n (T_n^4 - T_{amb}^4) + \rho_n H_n \tag{7.1}$$

where ϵ is the emissivity, σ is the Stefan-Boltzmann constant, T_n is the node temperature, ρ_n is the local reflectivity and H_n is the total radiation incident on the node per unit area. The first term on the right represents the local thermal emission and the second term represents the portion of incident radiation that is reflected off of the node surface.

105

The total radiation incident per unit area H_n is calculated as

$$A_n H_n = \rho_{shield} A_n B_n F_{nrn} + \rho_{shield} \sum_{i=1}^{m} A_m B_m F_{mrn} \tag{7.2}$$

where A_n is the area of node n, F_{nrn} is the view factor from node n to node n after reflection in the radiation shield, and ρ_{shield} is the reflectivity of the radiation shielding. The first term on the right represents the portion of radiation emitted from node n which is reflected back onto itself. The second term is a summation representing the total incident radiation after reflection from all other nodes and view factor F_{mrn} corresponds to the view factor from node m reflected in the radiation shield to node n.

Calculating B_n and H_n for all nodes yields the following system of equations

$$B_1 = \epsilon_1 \sigma_1 (T_1^4 - T_{amb}^4) + \rho_1 H_1$$

$$B_2 = \epsilon_2 \sigma_2 (T_2^4 - T_{amb}^4) + \rho_2 H_2$$

$$\vdots$$

$$B_n = \epsilon_n \sigma_n (T_n^4 - T_{amb}^4) + \rho_n H_n$$

$$H_1 = \rho_{shield}(A_1 B_1 F_{1r1} + A_2 B_2 F_{2r1} + \ldots A_n B_n F_{nr1})/A_1 \tag{7.3}$$

$$H_2 = \rho_{shield}(A_1 B_1 F_{1r2} + A_2 B_2 F_{2r2} + \ldots A_n B_n F_{nr2})/A_2$$

$$\vdots$$

$$H_n = \rho_{shield}(A_1 B_1 F_{1rn} + A_2 B_2 F_{2rn} + \ldots A_n B_n F_{nrn})/A_n$$

which can be solved for each B_n and H_n. The net energy flux at each node can then be calculated simply as the difference between power leaving the node and power incident upon the node.

$$q_n = A_n(B_n - H_n) \tag{7.4}$$

106

All of the terms given in Equations 7.3 can be easily obtained with the exception of the node-to-node view factors after reflection. Thus, a ray trace code was written by Dr. David Scharfe at the AFRL in order to produce the required nxn matrix of view factors. The view factor code accepts the test section and shield geometry and then pseudo-randomly launches 50 million rays distributed by total area. Rays are tracked, logging both their source and end points, and taking into account rays requiring multiple reflections within the radiation shield to either strike the crucible or exit the shield via the entrance aperture. The result of this ray trace code, illustrated in Figures 7.2, 7.3 and 7.4, yields a matrix of point to point view factors in the format

$$
\begin{bmatrix}
F_{1r1} & F_{1r2} & F_{1r3} & \dots & F_{1rn} \\
F_{2r1} & F_{2r2} & F_{2r3} & \dots & F_{2rn} \\
F_{3r1} & F_{3r2} & F_{3r3} & \dots & F_{3rn} \\
\vdots & \vdots & \vdots & \ddots & \vdots \\
F_{nr1} & F_{nr2} & F_{nr3} & \dots & F_{nrn}
\end{bmatrix}
\tag{7.5}
$$

With view factors calculated, Equations 7.3 can then be solved. At each time step, energy balances must be recalcualted so the solution to Equations 7.3 is reduced to a series of matrix operations to speed computations. The first step in finding the solution is to substitude all the B_n terms in Equations 7.3 to get a system of equations solely in terms of H_n. Each equation for H_n then takes the form of

$$
H_n = (\rho_{shield}/A_n) \sum_{i=1}^{m} A_m F_{mrn} \epsilon_m \sigma (T_m^4 - T_{amb}^4) + A_m F_{mrn} \rho_m H_m
\tag{7.6}
$$

Multiplying both sides of Equation 7.6 by (A_n/ρ_{shield}), moving all H_n dependent terms to the left and all other terms to the right yields the following series of equations

107

$$(F_{1r1}\rho_1 - 1/\rho_{shield})A_1H_1 + A_2F_{2r1}\rho_2H_2 + \ldots A_nF_nr1\rho_nH_n = -A_1F_{1r1}\epsilon_1\sigma(T_1^4 - T_{amb}^4)$$

$$-A_2F_{2r1}\epsilon_2\sigma(T_2^4 - T_{amb}^4)\cdots - A_nF_{nr1}\epsilon_n\sigma(T_n^4 - T_{amb}^4)$$

$$A_1F_{1r2}\rho_1H_1 + (F_{2r2}\rho_2 - 1/\rho_{shield})A_2H_2 + \ldots A_nF_nr1\rho_nH_n = -A_1F_{1r2}\epsilon_1\sigma(T_1^4 - T_{amb}^4)$$

$$-A_2F_{2r2}\epsilon_2\sigma(T_2^4 - T_{amb}^4)\cdots - A_nF_{nr2}\epsilon_n\sigma(T_n^4 - T_{amb}^4)$$

$$(7.7)$$

$$\vdots$$

$$A_1F_{1rn}\rho_1H_1 + A_2F_{2rn}\rho_2H_2 + \ldots (F_{nrn}\rho_n - 1/\rho_{shield})A_nH_n = -A_1F_{1rn}\epsilon_1\sigma(T_1^4 - T_{amb}^4)$$

$$-A_2F_{2rn}\epsilon_2\sigma(T_2^4 - T_{amb}^4)\cdots - A_nF_{nrn}\epsilon_n\sigma(T_n^4 - T_{amb}^4)$$

It is now possible to solve for all H_n values via matrix operations in MATLAB by converting the above system of equations into the following

$$\begin{bmatrix} \\ \\ LHS \\ \\ \\ \end{bmatrix}\begin{bmatrix} H_1 \\ H_2 \\ H_3 \\ \vdots \\ H_n \end{bmatrix} = \begin{bmatrix} \\ \\ RHS \\ \\ \\ \end{bmatrix} \tag{7.8}$$

where each row n of the LHS matrix is in the format

$$\begin{bmatrix} A_1F_{1rn}\rho_1 & A_2F_{2rn}\rho_2 & \ldots & (F_{nrn}\rho_n - 1/\rho_{shield})A_n \end{bmatrix} \tag{7.9}$$

108

noting that terms along the diagonal are of a different form to accommodate an additional $1/\rho_{shield}$ term and each row n of the RHS matrix is defined as

$$[-A_1 F_{1rn} \epsilon_1 \sigma(T_1^4 - T_{amb}^4) \quad -A_2 F_{2rn} \epsilon_2 \sigma(T_2^4 - T_{amb}^4) \quad \ldots \quad -A_n F_{nrn} \epsilon_n \sigma(T_n^4 - T_{amb}^4)] \quad (7.10)$$

Only the RHS matrix is temperature dependent. Thus, the LHS matrix can be pre-calculated before running the time dependent simulation. Additionally, all non-temperature dependent terms in the RHS matrix can also be pre-calculated and supplied in a matrix format to quickly build RHS for each iteration.

Once all H_n values have been found, B_n values can be calculated via Equations 7.3 and the net energy flux from radiation of each node can be calculated using Equation 7.4. These energy flux values are then inserted into the finite difference calculations at each exterior node.

The current radiation shielding geometry is an open topped cylinder which approximates the stainless steel testing chamber and neglects potential reflections from the quartz window. Calculations indicate an approximately 20% drop in radiation losses by including shielding effects in the model.

7.3   Results

Cooling behavior was simulated for a test section with the same geometry as that given in Figure 7.1 after bringing the test section to thermal equilibrium with a simulated solar furnace input power of 740 W. Figure 7.5 show the approximate freezing profile of the silicon PCM and it can be seen that the freezing profile is highly asymmetric. Note that this deviates from the symmetrical, adiabatic wall treatment of silicon as a PCM in the existing literature. With "real-world" boundary
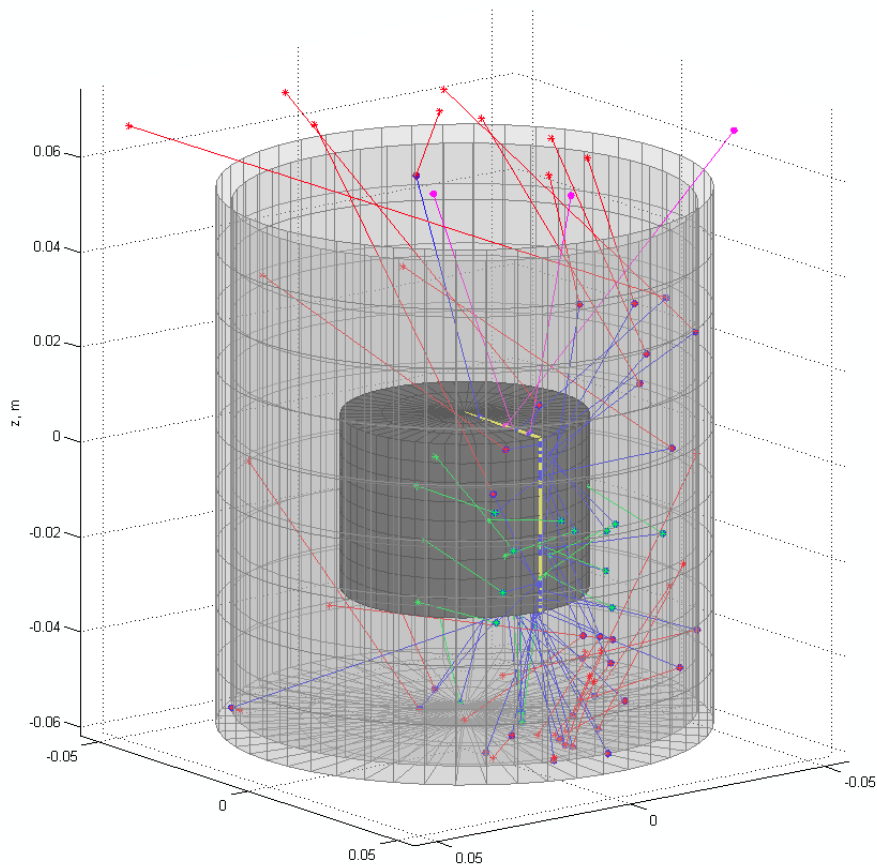
Figure 7.2: Example ray trace plot for view factor calculation using only 50 rays for visibility. Rays are launched from the "line of nodes" indicated in yellow and are tracked as they interact with the open topped cylindrical radiation shield. Rays leaving the crucible are in blue, rays returning to the crucible are in green, rays leaving the shield after one reflection are given in red, and rays leaving the shield after no reflections are given in pink.

conditions, heat loss from all parts of the container results in a multi-dimensional phase front ultimately leading to regions of molten silicon encased in solid silicon. As will be discussed in Chapter 8, the expansion of this trapped liquid silicon results in high stress concentrations and the potential for container damage.

It was also determined using the MATLAB model that the elimination of the cast ZrO_2 ceramic insulation from test sections as opposed to polished radiation shields would only result in minor
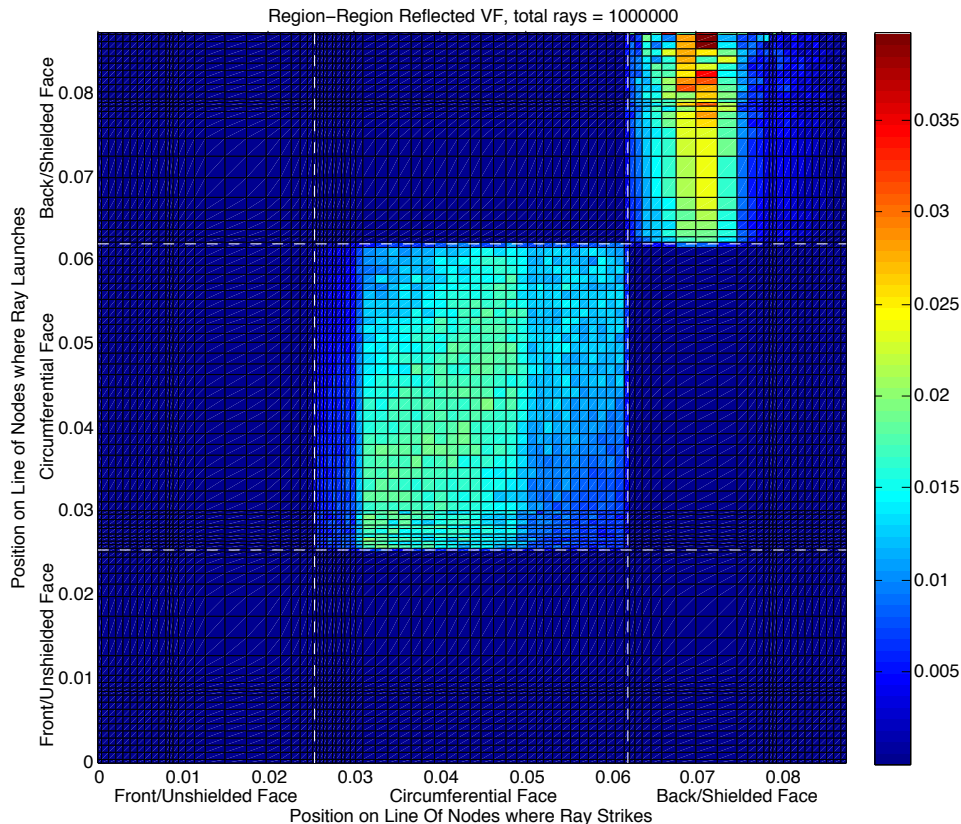
110

Figure 7.3: Ray trace results for a 1,000,000 ray calculation illustrating the magnitude of node to node reflected view factors within the modeled geometry. Because the radiation shield is modeled as an open top cylinder, the largest node to node view factors after reflection are calculated for nodes at the back/shielded face. Note that the scale has been set to highlight the relatively low view factor values.

performance gains in both experimental scale and maximum achievable temperature. Using cast ceramic as the primary insulation is less labor intensive than the radiation shield polishing process described in Chapter 6. Thus, future experiments eliminated any radiation shielding component beyond that provided by the testing chamber.

A control simulation was also performed for a graphite only test article. This test, which is diagrammed in Figure 7.6, maintains the same geometry but eliminates both the PCM and the
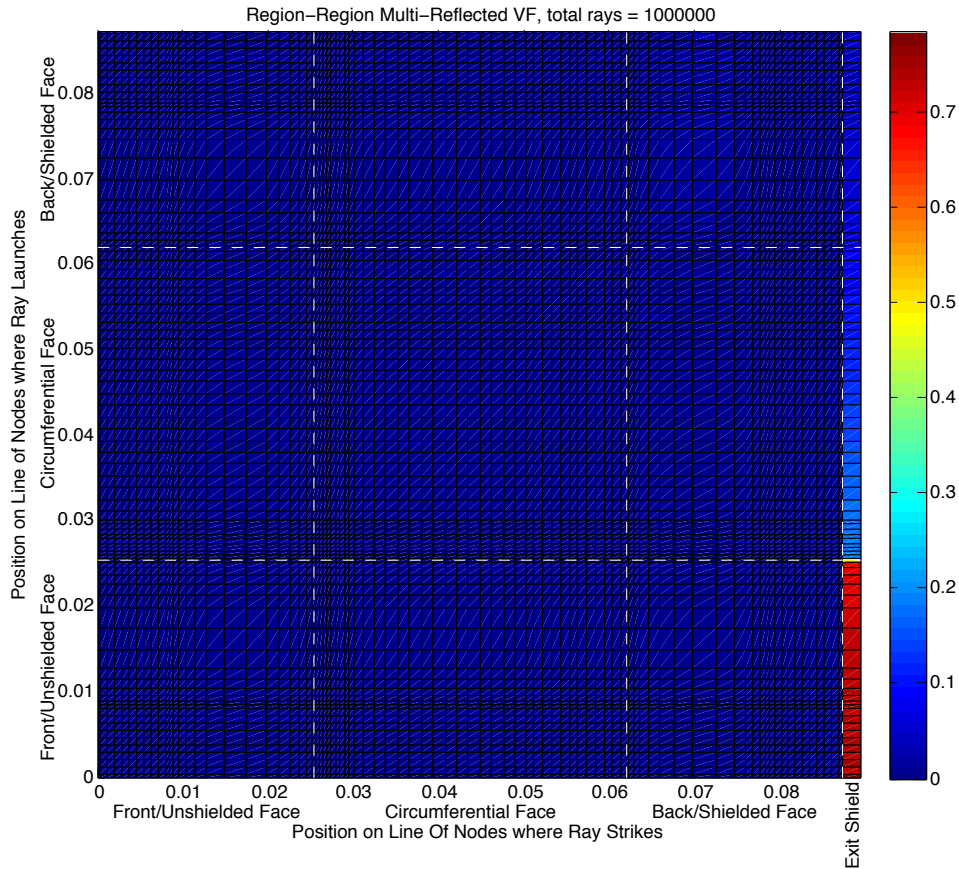
111

Figure 7.4: Ray trace results for a 1,000,000 ray calculation illustrating the likelihood of rays exiting the radiation shielding. Because the radiation shield is modeled as an open top cylinder, the majority of rays from the front/unshielded face escape the shield. Note that the results given in Figure 7.3 are obscured by the large scale.

PCM container. Control results for a simulated rear-mounted type C thermocouple are given in Figure 7.7 and compared against those for a test article containing silicon PCM.

The graphite-only case initially shows a higher temperature at the simulated thermocouple due to the elimination of liquid silicon and BN container from the test section core which both have a relatively low thermal conductivity compared to the bulk graphite. As expected, the graphite-only case exhibits a smooth cooling curve as sensible heat is removed from the system. In contrast, the test section containing the silicon PCM begins at a lower temperature and demonstrates a region of relative temperature stability due to energy release during the phase change process. Note in
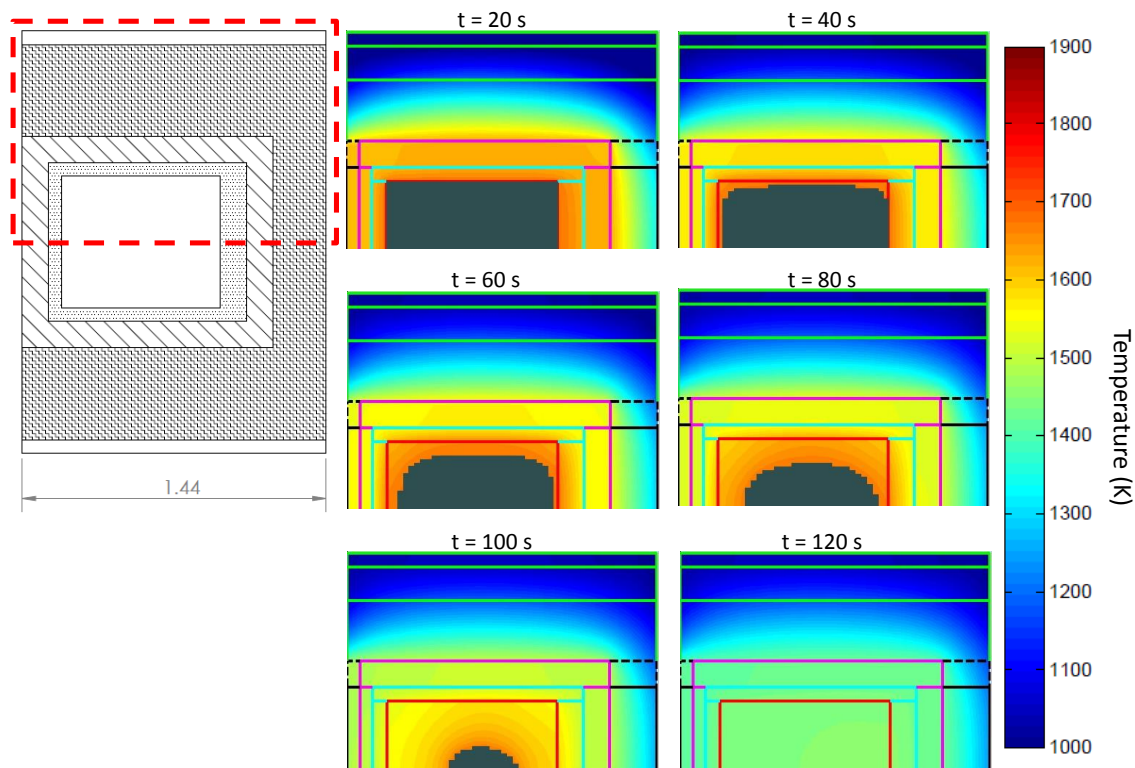
112

Figure 7.5: Thermal profiles as a function of time calculated by the in-house MATLAB model for the test section given in Fig. 7.1. Note that the model is axisymmetric so the red outlined region of the cutaway drawing is the region represented by the thermal maps. Also note that grey is used in the thermal maps to represent liquid silicon and it is apparent that liquid silicon will become trapped during the freezing process.

both curves that there is a roughly 10 second region of temperature stability after simulated solar furnace power is cut while thermal gradients within the test section re-orient.

The mean surface temperature of the exposed graphite surface on the front of the test section is also affected by the phase change process. However, it must be noted that before the phase change window, the thermal performance of the PCM under-performs the graphite only case. Calculated mean temperature curves given in Figure 7.7 show that the silicon based case quickly drops below the sensible heat case before being supported by latent heat release. Since the thermal conductivity

113
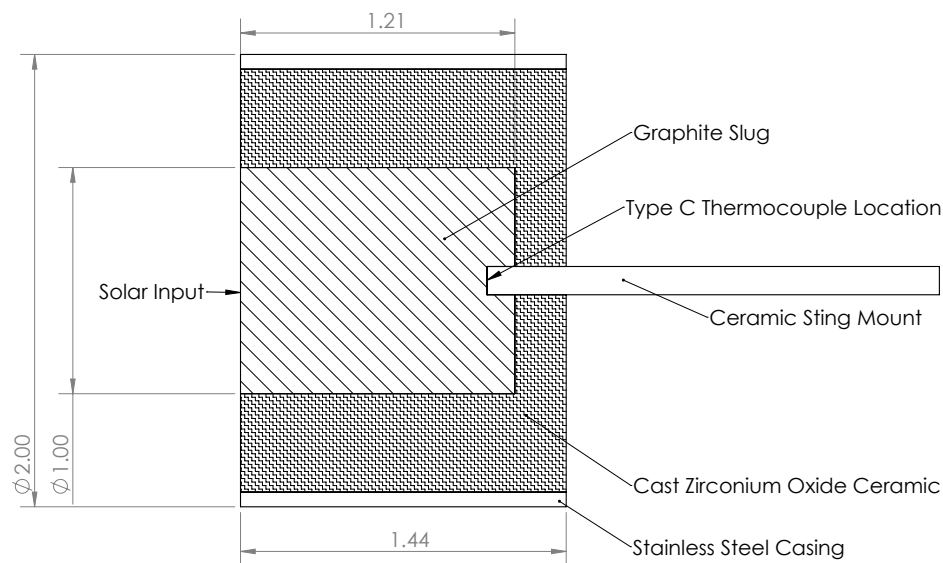
Figure 7.6: Cut-away diagram of a graphite only cylindrical test article. Dimensions given in inches.
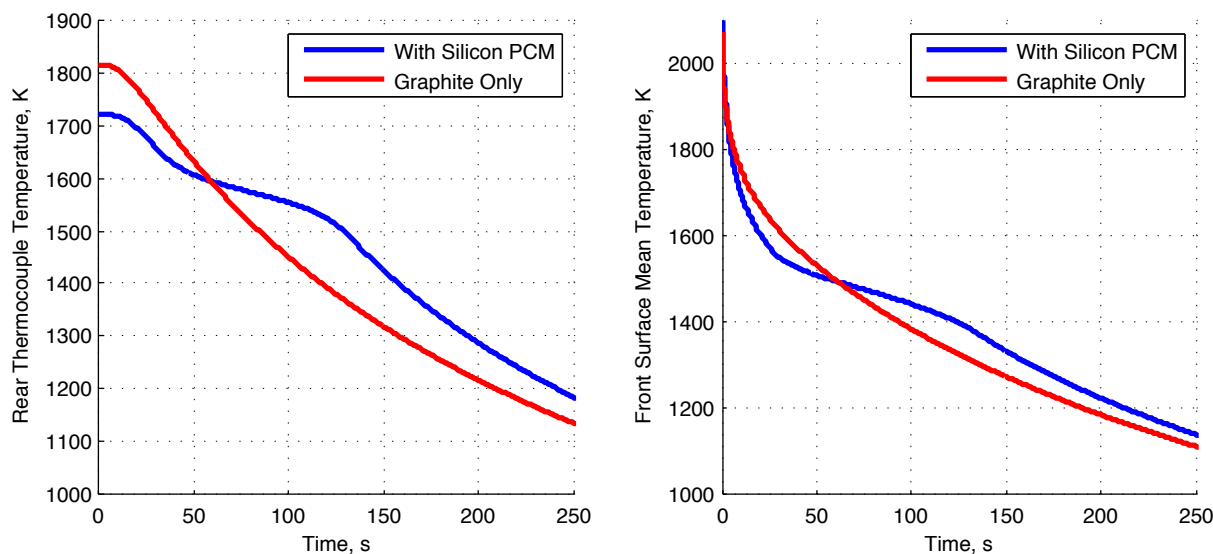
Figure 7.7: Temperature predictions for both the test section shown in Figure 7.1 and a pure graphite test section shown in Figure 7.6. Both test sections were bought to equilibrium with a simulated solar furnace input power of 740 W and furnace power was cut at time zero. The figure on the left gives temperatures for a simulated rear mount Type C thermocouple and the figure on the right gives a mean surface temperature for the exposed graphite surface on each test section.

114
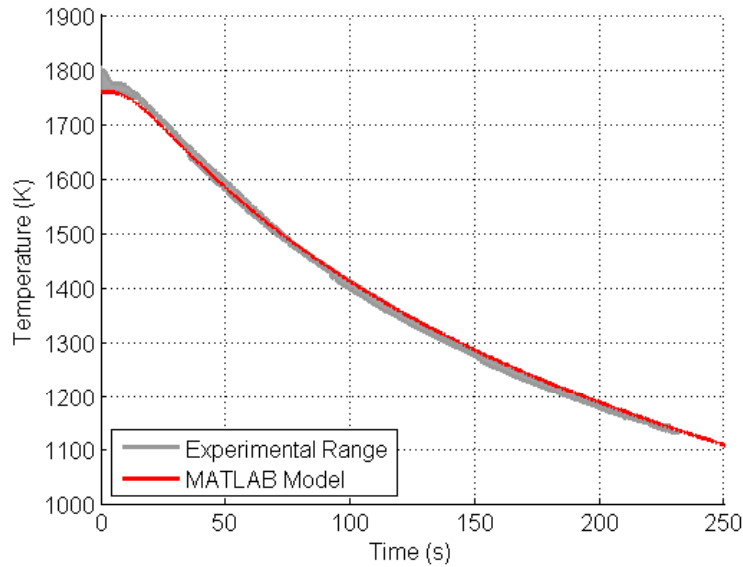
Figure 7.8: Comparison of experimental and MATLAB data for graphite only test sections using the geometry given in Figure 7.6. Note that experimental and simulated temperature traces match within $\pm 2\%$

of the PCM is low, the relatively isolated graphite on the front surface is able to cool quickly without being able to draw heat from the remainder of the system.

The USC solar furnace was used to produce experimental data for the graphite only test sections with the same geometry as those shown in Figure 7.6. Comparison of model and experimental data, given in Figure 7.8, shows that during the cooling process, temperatures for a rear mounted Type C thermocouple match within $\pm 2\%$ indicating that the sensible heat calculations within the in-house MATLAB model are correct. Validation of the latent heat components of the MATLAB model required molten silicon testing which is described in detail Chapter 8.

115

Molten Silicon Testing

The completion of the USC Solar Furnace and the advent of accurate prediction capabilities enabled a series of tests which produced molten silicon in the laboratory. The intent of these tests was to uncover practical concerns with using molten silicon as a phase change energy storage material that thus far had been neglected in the literature which consists primarily of simple, material property based comparisons. Additionally, molten silicon experiments were used to validate the results of the in-house MATLAB model and demonstrate that macro scale results relevant to a thermal energy storage system could be obtained with relatively simple handling of the phase change process. While experiments were limited to small quantities of silicon, they succeeded in highlighting multiple design concerns and proposed potential solutions for future molten silicon based designs.

8.1   Test Design and Procedure

Molten silicon tests were performed with cylindrical test sections keeping geometry consistent with that of the models discussed in Chapter 7. The primary design drivers for solar furnace test sections were ease of in-house manufacture and consistency with modeling capability as opposed

116

to maximum thermal efficiency. As a result, final test sections lack a cavity receiver in lieu of a flat plane absorber.

Test sections contain approximately 9 g of silicon and were limited in scale by the affordability of commercial silicon rod stock in addition to total solar furnace power. Test sections were designed with a minimum solar furnace input of 750 W and models identified potential geometries supporting over 30 g of molten silicon during the design phase. However, these geometries required the use of silicon chips or powder for loading and early solar furnace testing demonstrated that these packing methods yielded maximum fill factors (actual silicon volume vs available PCM container volume) of approximately 60%. To achieve a 100% fill factor, silicon rod was required and 1.6 cm diameter rod was sourced within budget. Test sections were designed around this material which fixed the diameter of the PCM container. Figure 8.1 shows a cutaway diagram of an experimental test section identifying the overall geometry and individual test section components.

Test section construction begins by loading a silicon rod into a cylindrical HBC grade BN container. HBC boron nitride was selected for all BN components since it lacks a boric oxide binder which can precipitate at high temperatures [3]. The BN container is sealed with a press fit BN lid and the finished PCM container is then inserted into a graphite sleeve. The graphite sleeve serves as both the solar energy receiver and primary emitter for the test section. Additionally, the inclusion of graphite helps to spread heat within the test section due to the relatively low thermal conductivity of solid silicon and BN. The graphite sleeve is capped with a friction fit lid containing a hole allowing a bare wire Type C thermocouple, sheathed in a dual bore Al_2O_3 tube, to be in direct contact with the inner PCM container. Ultimately, the Al_2O_3 thermocouple sheath is used as a sting mount to support the test section in the testing chamber.

To complete construction of each test section, the inner BN and graphite assembly is placed in a stainless steel mold and potted using commercially available Rescor 760 castable ceramic compound. This ZrO_2 ceramic product is low cost, easy to cast, and has an acceptably low thermal
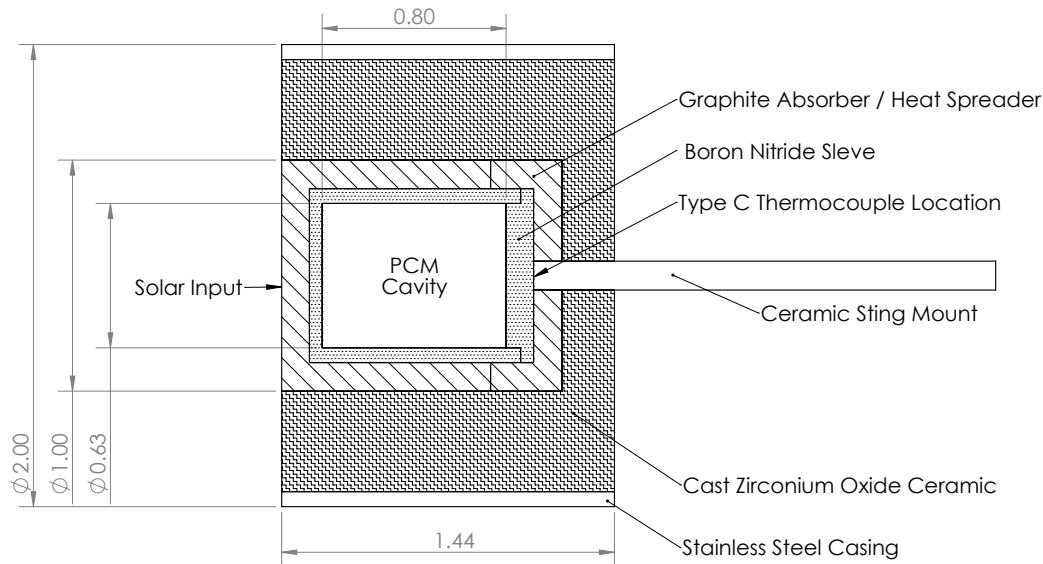
117

Figure 8.1: Cut-away diagram of a cylindrical test article sized for 9 g of silicon showing materials, components, and overall experimental geometry. Dimensions given in inches.

conductivity (approximately 0.93 W/mK dependent on mixing ratio and curing procedure [62]). However, the use of ZrO_2 ceramic in contact with graphite places limits on the experiment due to reactivity at elevated temperatures. ZrO_2 and graphite react at temperatures as low as 1400 K and with peak experimental temperatures exceeding 2000 K, the equilibrium pressure of the reaction is approximately 40 $Torr$ [127]. Before this reaction was identified, solar furnace tests resulted in irreversible contamination of the quartz vacuum chamber entrance window. To prevent contamination, at the expense of convection losses, current tests are operated in an environment of 150 $Torr$ of argon resulting in an approximately 10% increase in heat loss due to convection. Testing using a pure BN system would allow for low pressure operation without quartz window damage. However, the high cost and relatively low thermal conductivity of BN compared with graphite makes this approach impractical.

During the Rescor 760 casting process, additional Type K thermocouples are placed within the ceramic to monitor insulation temperatures. Test sections are allowed to dry in ambient conditions
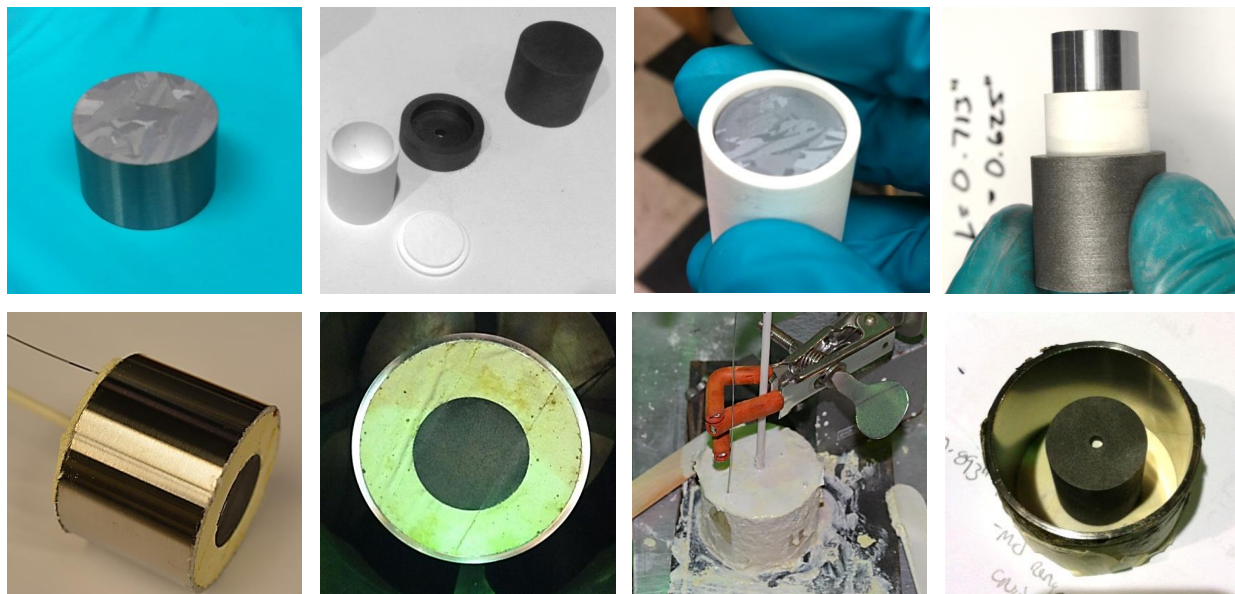
118

Figure 8.2: Montage of test section construction photos. Clockwise from top-left: Silicon rod sample, inner components after machining, silicon placement in BN sleeve, inner components supported via slip-fit before compression into place, assembly before ceramic casting, wet ceramic casting showing clamps for thermocouple support, completed test section face, completed test section body.

for 24 hours and then loaded into the solar furnace. Photographs of the test section construction process are given in Figure 8.2.

After test section construction, the first step in the furnace testing procedure was to bake out new test sections under vacuum at approximately 500 K using a 1000 W spot lamp. This process evaporates proprietary water based binders from the Rescor 760 compound which can fog the quartz vacuum chamber window and decrease power delivery. After an 8 hour bake out, the testing chamber was opened, a freshly cleaned quartz window was installed and the chamber was re-evacuated to approximately 10 $mTorr$. The solar furnace is then used to re-heat the test section to 600 K prior to vacuum pump shut down and an argon backfill to 150 $Torr$ is applied in order to suppress ZrO_2-C reaction during testing [127]

119

After bake out, solar furnace power was gradually increased in approximately 25% increments via an aperture curtain until the test article reaches molten silicon temperatures. Once thermal equilibrium has been achieved, a shutter curtain was used to cut power to the solar furnace and the cooling curve for the test section is recorded. If solar conditions permit, repeated cycles can be performed on each test section. All thermocouple and solar furnace power data was recorded during testing at a rate of 2 Hz using the instrumentation described in Chapter 5.

8.2   100% Fill Factor Testing

The first round of molten silicon testing was performed on sections with a 100% silicon fill factor. Silicon rods were precision cut to be an exact fit for the BN PCM container leaving no voids or gaps in the test articles and maximizing energy storage potential. Figure 8.3 shows experimental data taken during one such test. The phase change process occurs from approximately t = 30 s to t = 120 s and demonstrates the relative temperature stability expected from a latent heat system. The curves "Cycle 1" and "Cycle 2" are taken from the same test section across two back-to-back cycles.

Note that "Cycle 1" exhibits a temperature spike at t = 108 s. This spike corresponded with cracking of the test section due to asymmetric expansion of liquid silicon trapped within the partially frozen silicon bulk. Expansion results in both increased contact pressure within the container and a shift in container geometry producing higher recorded temperatures. Repeated tests also demonstrated similar temperature profiles and cracking behavior. Figure 8.4 shows photographs taken during the testing process for a 100% fill factor test section illustrating container failure. In the existing literature concerning silicon as a potential phase change material, volumetric expansion is neglected and as a result it was not a primary concern in both modeling and experimental efforts until this damage was observed.
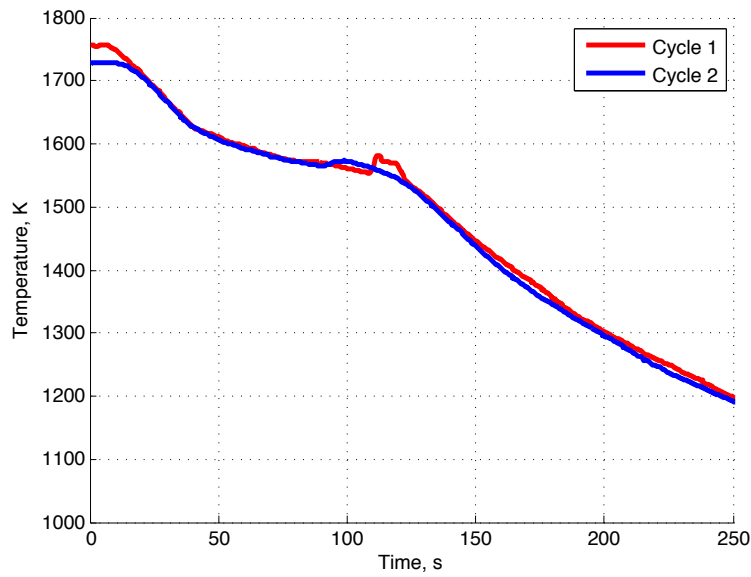
120

Figure 8.3: Experimental data taken with a Type C thermocouple as labeled in Fig. 8.1. Both traces are from the same test section in back to back cycles. Note that "Cycle 1" has a temperature spike at approximately t = 108 s corresponding to the rapid freezing of trapped silicon.

In addition to demonstrating the difficulties posed by silicon expansion, 100% fill factor testing illustrated other operational concerns. During test section heating, a rapid jump in temperature is apparent when the rear of the test section approaches 1500 K. A temperature curve during the heating process is given in Figure 8.5 which illustrates this temperature spike in the absence of increasing solar furnace power. This temperature spike corresponds to the phase transition of the silicon bulk and the rising rear temperature is a function of a step change in silicon's thermal con-ductivity from approximately 18.5 W/mK at the melting point to 51 W/mK once liquid [128]. In order to account for this change, thermal designs must consider the lower thermal conductivity value to ensure sufficient heat conduction throughout. In this testing series, relatively small reduc-tions in total solar furnace power have produced incomplete melting when the system was unable to overcome this thermal conductivity barrier.

A total of three 100% test sections were successfully brought to molten silicon temperatures and a composite of their cooling curves is presented in Figure 8.6. This plot also contains the results
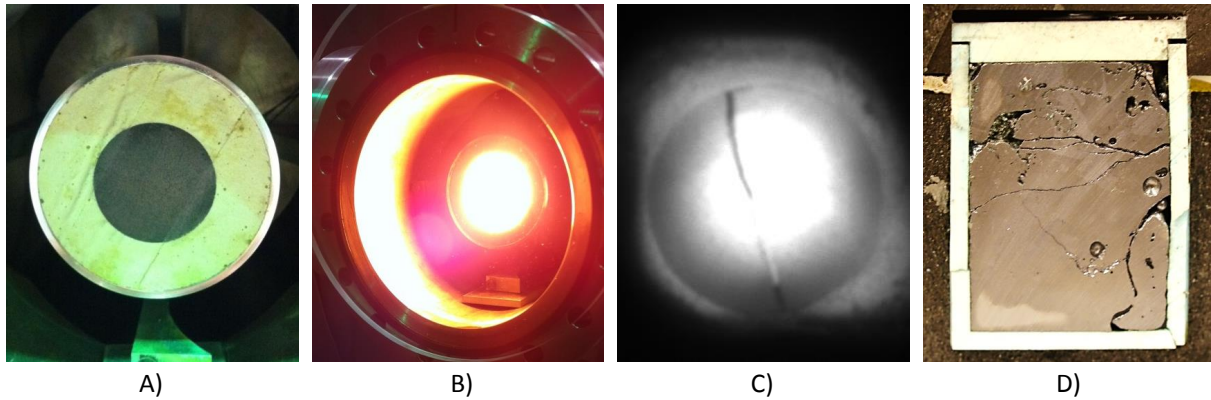
121

Figure 8.4: Photographs taken during 100 % fill factor tests. A) Test section before heating. B) Test section immediately after power cutoff. C) Infrared photograph taken during solar heating showing a large crack formed in the test section during the previous cooling cycle. Note the relative size and intensity of the solar furnace input. D) Image of the interior of the crucible after being cut in half showing decreased silicon density post testing.

of the in-house MATLAB model and demonstrates its ability to predict representative test section performance despite the relative simplicity of phase change calculations. It is important to note that the thermal conductivity of the boron nitride liner was reduced by an order of magnitude (3 vs. 25 W/mK) in the model to provide an adequate fit. Since the model neglects thermal contact resistance and the machining process does not yield perfect mating of parts, this reduction can be justified. Additionally, the area-averaged receiver (exposed graphite) temperature only varies by a maximum of 3.5% when reverting the boron nitride back to the literature value. Relative insensitivity of global parameters to this thermal conductivity value indicates that variation of this material property primarily accounts for ineffective coupling of the Type C thermocouple to the experimental system.
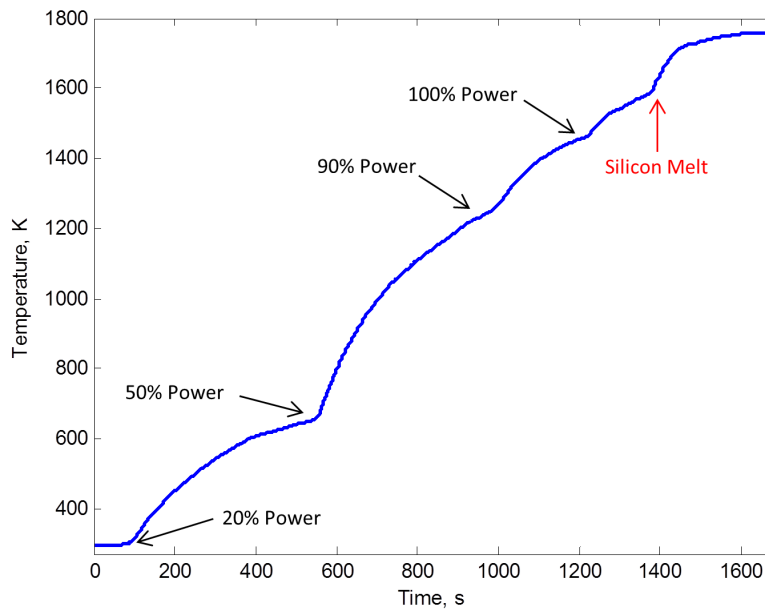
Figure 8.5: Initial experimental heating curve for a test section at a 100% silicon fill factor. Note the four distinct heating regions as solar furnace power was gradually increased and a 5th rapid rise in temperature corresponding to complete melting of the silicon PCM.

8.3 Expansion Damage Mitigation

Despite being neglected in the majority of extant literature concerning silicon as a PCM, the issue of volumetric expansion presents the greatest difficulty for realizing an effective system. Silicon is one of the few materials that expands during freezing and the relatively large volume increase of approximately 10% poses a significant challenge [121]. The majority of phase change materials currently in use expand when melting (including boron) and this is typically resolved by incorporating an expansion area to accept and drain back the additional liquid volume during thermal cycling. Water is the only other material currently considered as a commercial PCM which undergoes freezing expansion and it is typically held in either open or flexible containers to prevent system damage. In the case of a silicon based system for satellite applications, a flexible or open topped container is likely not possible. When using a sealed and filled container, perfect
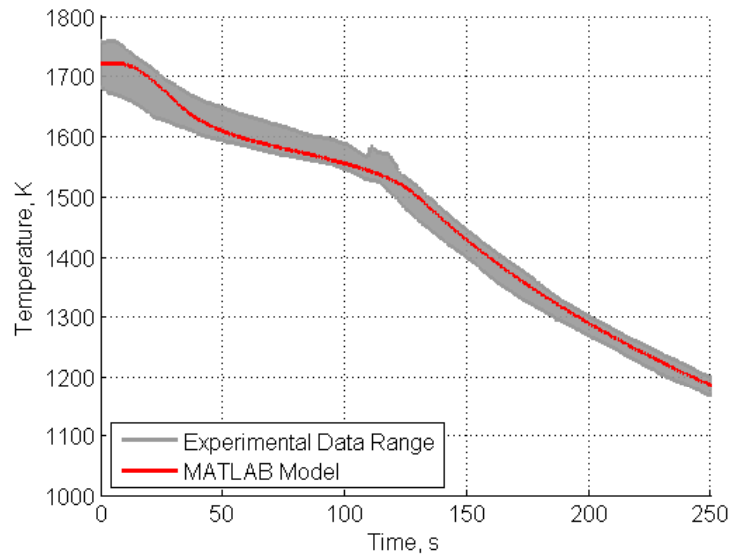
123

Figure 8.6: Comparison of experimental and MATLAB data for 100% fill factor testing using the geometry given in Fig. 8.1. The experimental data range includes data across three test sections and 4 thermal cycles. The temperatures given are at the Type C thermocouple location shown in Fig. 8.1.

re-solidification could theoretically return the silicon to the original shape. However, in practice asymmetrical freezing will lead to voids, trapped liquid volumes, and a decreased effective density.

In industrial applications, the difficulties of asymmetric silicon freezing are alleviated via precision control of thermal gradients leading to an approximately 1-D freezing front [129, 130]. In the case of a thermal energy storage system, this approach is impractical as multiple heat paths out of the silicon container will yield multiple freezing locations. In order to prevent container damage when freezing, a silicon based latent heat system will have to employ a reduced fill factor, precise geometry to control heat flow, safeguards to prevent complete solidification or, more likely, a combination of all three.

8.3.1 Reduced Fill Factor

Following 100% fill factor testing, experiments were performed in the hope of establishing a reliable testing configuration that would allow for repeated testing without test section failure. The

124

first step in this investigation was performing a series of tests utilizing the same geometry as in Fig. 8.1 with gradually reduced fill factors. Tests were conducted with fill factors between 100% and 80% decreasing in 5% increments.

During this testing series, no test sections with fill factors less than 100% showed the macro-scale damage seen during 100% fill factor trials. But, audible cracking during the phase change process provided an indication of internal test section damage. Once fill factors were reduced to 80% there was only a single instance of audible cracking during the phase change process across 15 thermal cycles and three test sections. However, when cut open and examined, it was seen that small cracks had still formed in the internal boron nitride liners.

When sectioned, 80% fill factor test articles consistently indicated an interesting silicon freezing behavior. Since silicon is non-wetting to the BN sleeve, the liquid silicon forms a "bead" within the test section upon melting. Due to the reduced fill factor and increased liquid density, this "bead" does not make contact with the upper ends of the container. The shape of silicon after testing, as shown photographed in Fig. 8.8, suggests that during the freezing process the front of the liquid "bead" freezes first as the receiver side of the test section is responsible for the majority of heat loss. Once this freezes, the remainder of the liquid "bead" is isolated from the front of the PCM cavity. This causes freezing silicon to completely fill the rear of the test section until pressure caused by volumetric expansion cracks the front of the "bead" and the remaining liquid silicon is extruded into the front void.

The composite cooling curve for all cycles using this testing condition is given in Fig. 8.7. As with 100% fill factor testing, this plot also gives MATLAB model results. In order to approximate the effects of a lower fill factor, the latent heat available to the MATLAB model was reduced by 20% while other parameters were kept constant. Despite this simplistic approach, the MATLAB model similarly follows experimental results.
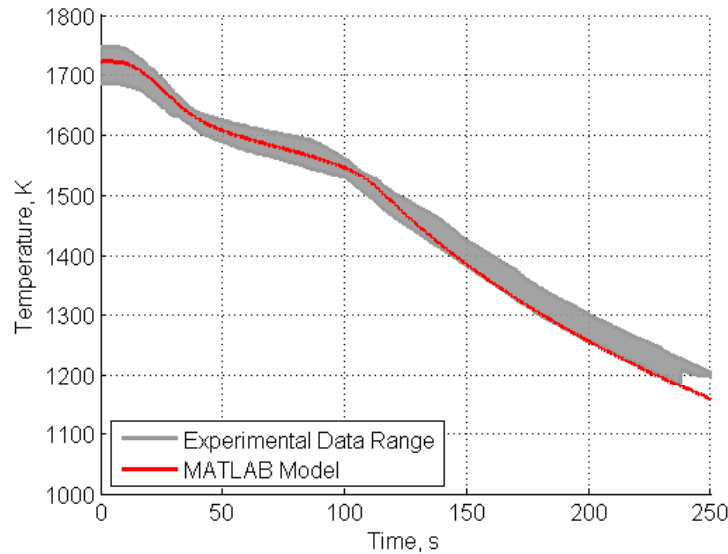
Figure 8.7: Comparison of experimental and MATLAB data for 80% fill factor testing using the geometry given in Fig. 8.1. The experimental data range includes data across three test sections and 15 thermal cycles. The temperatures given are at the Type C thermocouple location shown in Fig. 8.1.

8.3.2 High Density Graphite

After 80% fill factor tests repeatedly demonstrated damage only limited to the internal BN liners, a solution was sought to eliminate this component from the system. In response to the successful use of pure graphite crucibles during early tube furnace tests, solar furnace test articles were constructed with a bare graphite PCM container. While eliminating synergy with potential molten boron experiments, bare graphite containers for liquid silicon are common in the industrial production of large silicon ingots. Literature on the casting of silicon indicates that non-wetting behavior and carbon contamination in the silicon bulk on the order of $< 20\ ppm$ is possible using graphite crucibles provided that the graphite density is $> 1.75\ g/cc$ and that the graphite grain size is $< 50\ \mu m$ [117].

Figure 8.9 shows the design of bare graphite test articles. The PCM cavity was integrated into the graphite absorber and heat spreader with a press fit lid sealing the container at the top. SIC-6 grade graphite was sourced from Graphite Machining Services Inc (GMSI) to construct the

126

graphite components. SIC-6 graphite has a density of 1.85 g/cc and a grain size of 10 μm which is within the published requirements for low contamination and non-wetting behavior. A BN disk is included at the top of the test section to protect the tip of the type C thermocouple at high temperature. The remainder of test section construction is identical to those shown in Fig. 8.1 and an 80% fill factor condition was maintained for all test articles.

Test sections constructed using SIC-6 graphite exhibited no audible cracking and showed no damage after multiple freezing cycles. However, test sections exhibited behavior indicating wetting by liquid silicon which is in contrast to predictions made in the literature. An additional test section was constructed substituting B325 industrial graphite which is outside the recommended specifications for density and grain size. Test section performance and silicon behavior for this lower density graphite was qualitatively identical.

Figure 8.10 shows the interior of a SIC-6 test section after melting in the solar furnace. Like the previous tests using BN liners, there were voids apparent in the silicon bulk. However, it was evident that in these tests silicon had been wicked into the corners of the test article indicating wetting behavior. While the contamination of the silicon bulk has yet to be investigated, this wicking behavior could be beneficial in a spacecraft system. Unlike BN lined tests which formed a central mass of liquid silicon, pure graphite containers could keep liquid silicon and the subsequent freezing process along the walls of the container. This would aid in overall heat transfer and maintain a central void to take up silicon expansion.

The composite cooling curve for all cycles using pure graphite PCM containers is given in Fig. 8.11. MATLAB model results are also included. Note the relatively large experimental temperature spread of $\pm 4\%$ which is a result of both differing grades of graphite as well as a 10% variation in input power.

127

8.3.3 Partial Freezing

Another potential method for mitigating test section damage is to only allow for partial freezing of the silicon by re-introducing power to the system before complete solidification. This was attempted using a test section with a 100% fill factor and power was returned to the test section after 50, 60, and 70 seconds with temperature data given in Figure 8.12. All three of these intervals were successful and the test section indicated no audible cracking or physical container damage. Since it is estimated that the phase change process begins approximately 30 seconds after cutting solar furnace power, the longest 70 second freezing interval represents roughly 45% of the total phase change process length and the total energy storage achievable in the test section is reduced accordingly. Further testing is required to determine the ultimate level of solidification possible.

This method has potential for flight systems, provided the duty cycle can be matched to the eclipse period on orbit. However, it proves problematic for solar furnace ground demonstrations. Since crucible failure is assured when the experiment is terminated, a limited number of cycles is possible with each test section. This is further constrained by the limited experimental time afforded by the placement of the USC solar furnace facility.

8.4 Summary

Testing performed using the USC Solar Furnace successfully produced samples of molten silicon via concentrated sunlight. These experiments ultimately highlighted the asymmetry of the silicon freezing process and identified the management of freezing expansion as the primary technological hurdle in the design of a molten silicon based energy storage system. Multiple methods for mitigating freezing expansion damage in a cylindrical container were explored and satisfactory results were obtained by reducing the total PCM cavity fill factor to 80% and constructing test sections from high density graphite. Experiments were also used to validate the in-house MATLAB model

and showed that using the temperature transforming method along with other simplifications can accurately predict macro-scale thermal behavior of a molten silicon based system.

129
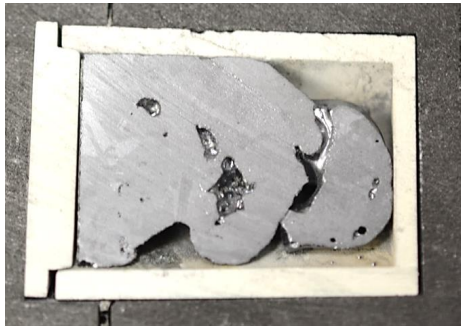
Figure 8.8: Photographs taken after sectioning an 80% fill factor solar furnace test article. The graphite absorber / heat spreader, boron nitride liner, and silicon are shown. Test section geometry is given in Fig. 8.1. In all photographs the rear of the test section is on the left. A) Top half of the test article. B) Bottom half of the test article in a top down view as related to the test section as a whole. Note how the rear of the test section is filled and external voids are present at the front. C) Top half of the silicon removed from the top of the test article and flipped vertically. The formation towards the right indicates flowing liquid silicon. D) Top down view of the test article with silicon restored. It is apparent that after initial silicon freezing, liquid silicon was forced from the top of the silicon bead.
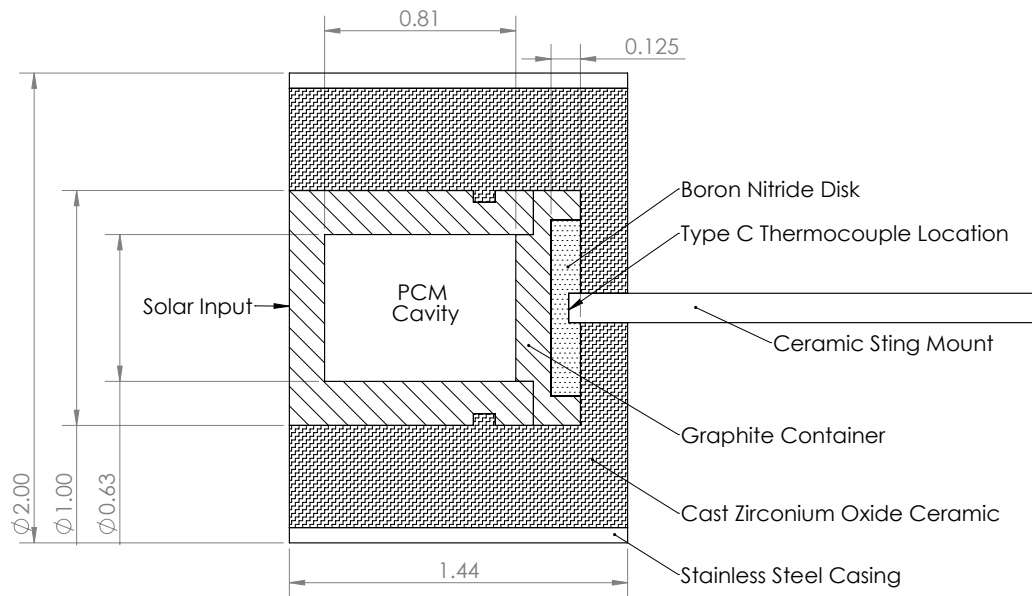
Figure 8.9: Cutaway diagram for test sections with a graphite walled PCM cavity. Note the presence of a small cutout in the outer wall of the graphite container. This was added as a retention mechanism after repeated failures caused by a slight negative draft machined outer wall of test sections. This draft, coupled with differential thermal expansion, would separate the two components of the container. Dimensions are given in inches.
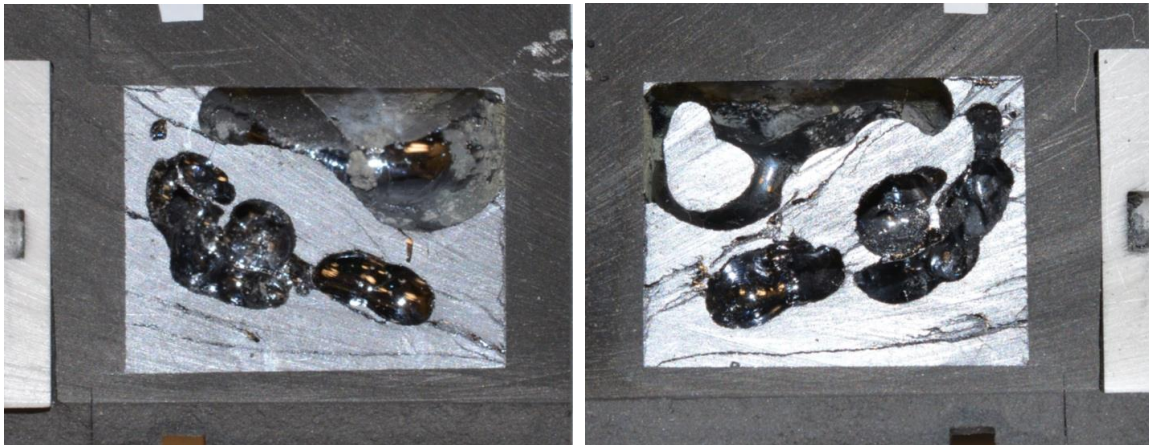
Figure 8.10: Photographs taken after sectioning a test article with a graphite walled PCM cavity. Note the silicon wicked into the upper corners in the front of the test section (center of image) indicating wetting behavior. This is in contrast to the behavior seen in Figure 8.8.

131
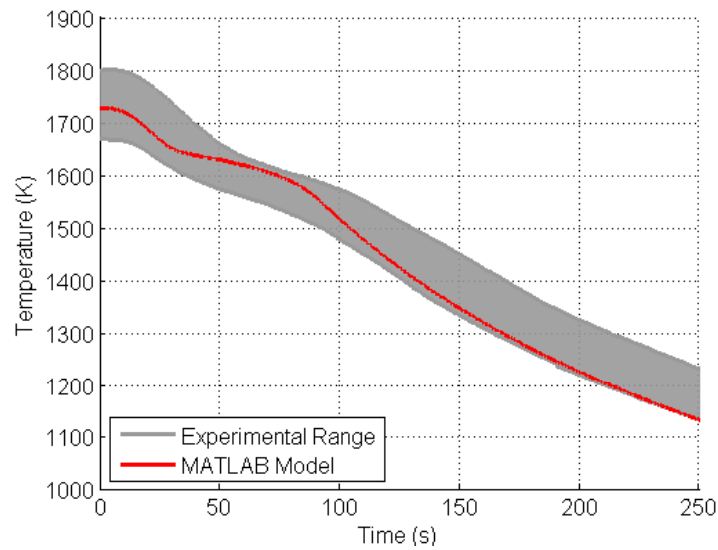
Figure 8.11: Comparison of experimental and MATLAB data for 80% fill factor testing, graphite walled PCM cavity test sections using the geometry given in Fig. 8.9. The experimental data range includes data across three test sections and 6 thermal cycles. The temperatures given are at the Type C thermocouple location shown in Figure 8.9
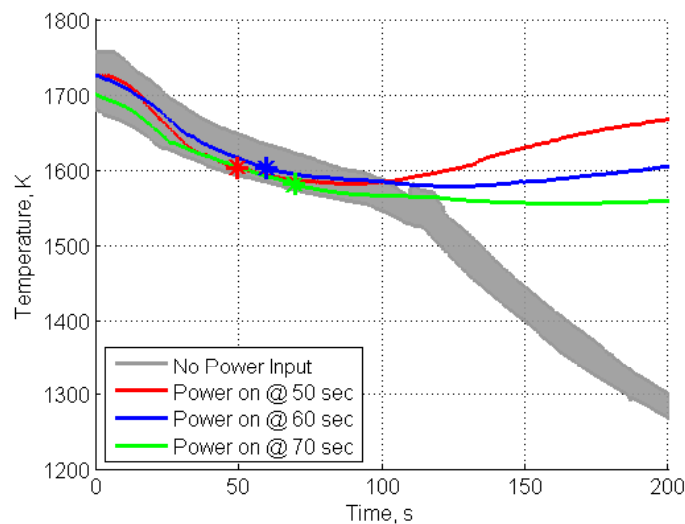
Figure 8.12: Experimental data demonstrating successful partial freezing trials compared with experimental data with now power restoration. A star marks the point where power is restored in each trial.

132

Future Work

The results of the experimental effort at USC prove the basic feasibility of the high temperature latent heat thermal energy storage while highlighting engineering concerns such as asymmetric freezing. This has identified several potential research questions which must be answered before a prototype system can be developed. Chief amongst these concerns are the effects of asymmetric energy release when trying to convectively couple to a propellant or working fluid. Note that future work items are related to the development of silicon based thermal energy storage in general and have benefits beyond solar thermal propulsion applications. In particular, the experimental facility developed during this research effort is well suited to continue molten silicon based work for terrestrial applications with minor improvements.

## 9.1 Convective Coupling Characterization

Recently, a group at the Center for Space Nuclear Research (CSNR) completed a conceptual design of a nuclear thermal bi-modal spacecraft for low-cost interplanetary exploration [92]. The proposed spacecraft design couples a radioisotope thermal generator with a high performance thermal capacitor to create a high power pulsed energy source usable for both direct thermal propulsion or high power electric generation. This configuration takes advantage of the high specific energy of a

133

radioisotope system while still allowing high power operation for short periods. It is proposed that such a bi-modal spacecraft could deliver a 10 kg scientific payload into orbit around the Saturnian moon Enceladus with a total launch mass of only 1000 kg.

At the core of the CSNR design is a combined high performance heat exchanger and thermal capacitor using silicon as a latent heat thermal energy storage material. The use of silicon TES in a nuclear thermal system has similar design constraints as solar thermal application and can be used to further illustrate convective coupling concerns when using latent heat. As illustrated by the boron based systems comparison in Section 4.2.1, harnessing the power of a latent heat medium requires analysis of both the total energy storage density and the effective energy storage density as defined by conjugate heat transfer geometry.

9.1.1 CSNR Design

The thermal power sub-system for the proposed CSNR spacecraft was sized by communication power requirements on-orbit at Enceladus. The design specifies a pair of closed Brayton cycle engines for electrical power generation which are fed via a Helium gas blowdown through the molten silicon based heat exchanger. The design goal for the system is to provide pulsed power of 25 kW_e for 360 seconds enabling a 3 Mbps downlink for the transfer of scientific data every 21 hours. Since the electrical conversion efficiency is specified at 30%, this means that the heat exchanger must supply 83.3 kW of thermal energy throughout each 360 second Helium blowdown cycle. The total helium flow rate for the heat exchanger was specified at 0.02 kg/s with an input temperature of 903 K.

The core of the CSNR heat exchanger / thermal capacitor is specified as an 18.5 cm diameter, 30 cm long cylinder containing the silicon TES mass, 6 PuO_2 fuel rods, and 195 approximately 5 mm diameter flow channels. The amount of silicon TES required was sized purely from the latent heat energy storage density and is specified at 15.58 kg. Insulation is provided by a combination of zirconia and high performance carbon aerogel.

134

To determine the estimated performance of the proposed CSNR design while including convective coupling effects, STAR-CCM+ has been used to model a single representative heat exchanger passage. Similar to the ISUS analysis presented in Section 4.2.1, the macro properties of the CSNR heat exchanger were divided by the total number of heat exchanger passages to yield a single 5 mm diameter ID, 30 cm long helium flow channel surrounded by 80 g of silicon TES. A 0.25 mm thick rhenium layer and a 0.5 mm graphite layer were added to the passage design considering sealing problems during the ISUS program and the need for a suitable container material. Additionally, based on the results of this work, the total silicon density was reduced by 20% to approximate an 80% fill factor condition to accommodate freezing expansion. This resulted in a passage OD of 14.95 mm.

Helium gas flow through the heat exchanger was modeled as a viscous, turbulent and ideal gas with temperature dependent properties and a flow rate of 0.103 g/s. The CSNR design specifies a heat exchanger operating pressure of 4000 kPa. However, in order to speed convergence, STAR-CCM+ models were performed at 101 kPa. Initial flow conditions for both pressures were compared and it was found that output temperatures varied between the two pressure conditions by less than 1% and that peak channel Reynolds numbers varied by less than 5%. Thus, it is expected that the thermal behavior of the simulated system will be comparable to the CSNR design.

Solid properties were modeled as being fully temperature dependent and the silicon phase change process was accommodated via the temperature transforming method with a "mushy" zone of $\pm$ 2.5 K. All outer boundaries were adiabatic which is consistent with the proposed CSNR design at the timescale of a single blowdown. The total insulation losses were estimated to be only 795 W which is approximately 1% of the desired Helium power draw.

After setting an initial solid temperature condition of 1700 K and establishing Helium flow at zero seconds, the STAR-CCM+ model was completed as a 2-D axisymmetric implicit unsteady
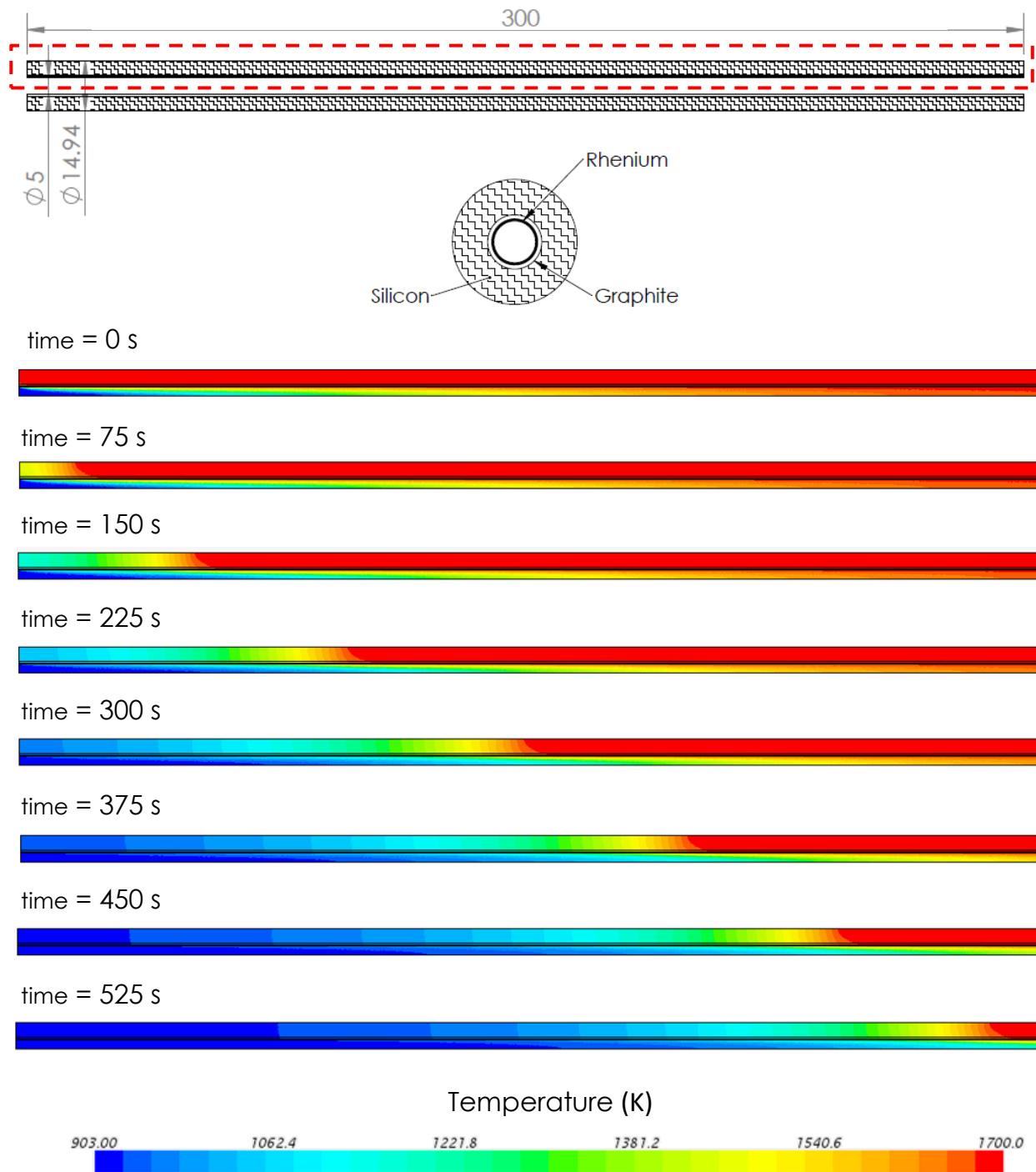
Figure 9.1: Modeling geometry and transient temperature profiles for the "CSNR Design" STAR-CCM+ model. Model geometry is axisymmetric and represents the red outlined region of the cylindrical heat exchanger passage. Helium flow through the passage is from left to right and dimensions are given in millimeters.

136
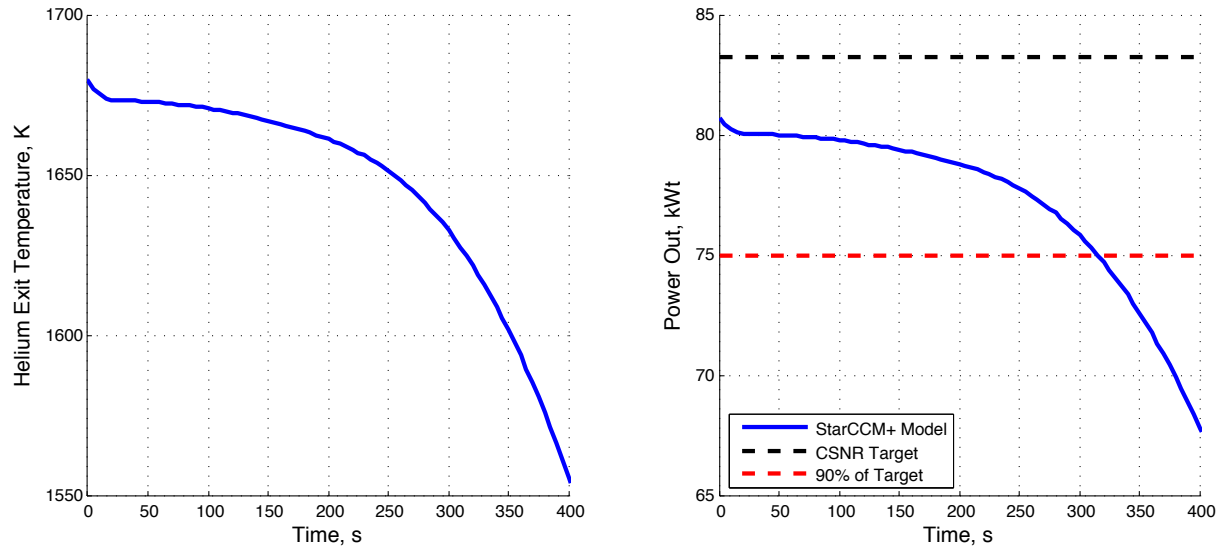
Figure 9.2: Heat exchanger thermal output performance for the proposed CSNR system. Temperatures are calculated as the mass flow averaged temperature for the simulated heat exchanger passage in Figure 9.1. Thermal power output is calculated as the energy required to bring propellant from the inlet temperature of 903 K to the specified output temperature at the given mass flow rate.

simulation. Transient temperature profiles for the model are given in Figure 9.1 and thermal performance of the represented heat exchanger is given in Figure 9.2.

In the model, the silicon freezing process takes in excess of 525 seconds. However, the heat exchanger never achieves the design power output and is only capable of achieving 90% of the desired power level for approximately 316 seconds. There are two factors affecting this performance. The first is the overall length of the heat exchanger. At 30 cm, the initial thermal profile in Figure 9.1 shows that peak temperature is achieved with little margin.

The second concern is asymmetric freezing of the silicon TES due to the convective coupling profile. Like the ISUS system, higher heat draw from the inlet results in an almost 1D phase front which moves further down the heat exchanger passage during blowdown. The low thermal conductivity of solid silicon near the melting point prevents diffusion of the remaining latent heat energy and a large thermal gradient forms within the TES. Once the phase front moves past

137

a certain length, there is insufficient distance for effective heat transfer to the gas flow and the heat exchanger output temperature drops dramatically at approximately 25 seconds as shown in Figure 9.2.

9.1.2 Convective Coupling Optimization

If the effects of asymmetric heat transfer are considered, it is possible to re-design the heat exchanger passage to yield higher effective energy storage density and stronger thermal performance. A basic length optimization of the heat exchanger passage has been performed via a series of STAR-CCM+ models. Passage length was varied from 15 to 70 cm while keeping the helium mass flow rate and the amount of silicon thermal energy storage constant. This effectively varies the aspect ratio of the model, spreading the thermal energy storage across a wider area and providing an extended convective coupling length. The results of this length optimization are given in the left of Figure 9.3.

The first results plot concerns the initial mass flow average exit temperature as a function of passage length. As expected, increasing channel length increases the propellant exit temperature until it reaches quasi-equilibrium with the initial TES temperature of 1700 K. If the acceptable performance threshold for the heat exchanger is set at 90% of the desired power draw, an exit temperature of at least 1624 K is required. It can be seen that at the shortest passage lengths, there is insufficient heat transfer area to achieve minimum acceptable performance even in the initial state.

The second set of results gives the duration of sustained power output at 90% and 95% of the target power level. Note that as the length of the heat exchanger is increased, the same amount of silicon thermal energy storage provides significantly higher performance. This increase in effective energy storage density is a result of a favorable convective coupling environment.

As shown in the model for the 30 cm design case, performance is ultimately limited by differential cooling of the passage. As the rear of the passage cools, the beginning of the effective heat
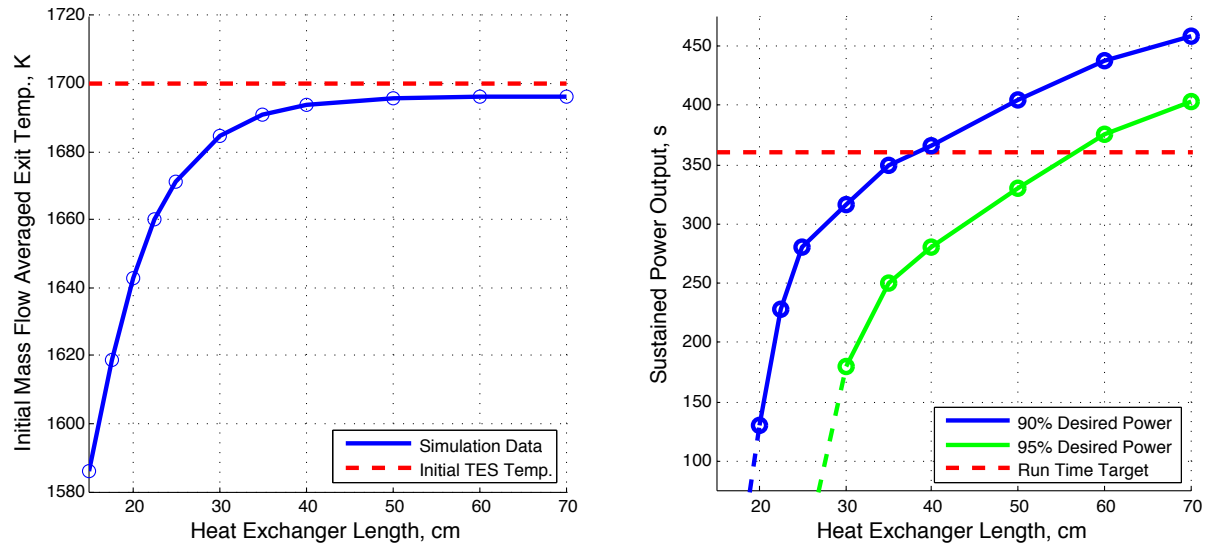
138

Figure 9.3: STAR-CCM+ length optimization data for the proposed CSNR heat exchanger. Increaseing heat exchanger length increases the total area availible for convection producing higher initial temperatures and increases utilization of the silicon PCM producing higher performance.

transfer region moves forward along with the point of quasi-thermal equilibrium. The phase front within the PCM moves in step with the onset of convection since this is the location of maximum ΔT and the low thermal conductivity of the recently frozen PCM prevents rapid diffusion of the remaining latent heat energy. This results in an effective minimum length of liquid PCM which must be maintained within the heat exchanger to reach the desired temperature - a requirement that is quite different from simply the minimum PCM required to store the needed thermal energy.

For the 90% power case, the minimum convective coupling length is slightly under 20 cm. As a result, a 20 cm long passage is able to sustain the desired power output for a short period of time. As the heat exchanger length increases, performance initially shows a rapid increase as the exit temperature approaches quasi-equilibrium with the liquid PCM creating a higher initial exit temperature margin. Once the passage length is sufficient for the fluid to reach quasi-equilibrium with the liquid PCM (approximately 35 cm), performance gradually increases until maximum utilization of the phase change material is reached.

139

Note that the maximum performance value doesn't plateau as graphite and rhenium layers are considered in the model effectively adding more mass to the system producing a sizable sensible heat energy storage component. Additionally, the sensible heat component of the silicon TES must also be considered. At 90% power draw, latent heat energy accounts for approximately 300 seconds of the sustained power.

This simple optimization shows that proper design of a phase change material based system must consider the motion of the phase front in relation to the convective coupling profile. Since heat exchanger length is limited by other concerns such as spacecraft size and insulation requirements a more detailed characterization of the convective coupling problem is required. An extended effort is necessary to relate total PCM storage mass, passage length, passage inner diameter, and mass flow rate for multiple propellant gases. This can provide simple approximations and relations that can be used for future designers to balance effective energy storage density against other requirements.

9.1.3 Convection Model Validation

To validate convective coupling characterization, experiments are required which mirror modeling conditions. The primary concern for these experiments will be attempting to match adiabatic boundary conditions and ensuring that environmental heat loss is a small fraction of the convective power draw. Ideally, this can be accomplished through the use of the molybdenum / zirconium oxide multifoil insulation described in Section 3.3.4 and resistive heaters to achieve molten silicon temperatures.

In the case where advanced multi-foil insulation is unavailable, it is possible to conduct meaningful experiments using alternatives with an increase in experimental complexity. An attempt was made to reach molten silicon temperatures for an approximately 21 cm test section using cast zirconuim oxide insulation as the primary insulator and molybdenum wire heaters. The test article, diagrammed in Figure 9.4 was able to achieve molten silicon temperatures across the entire
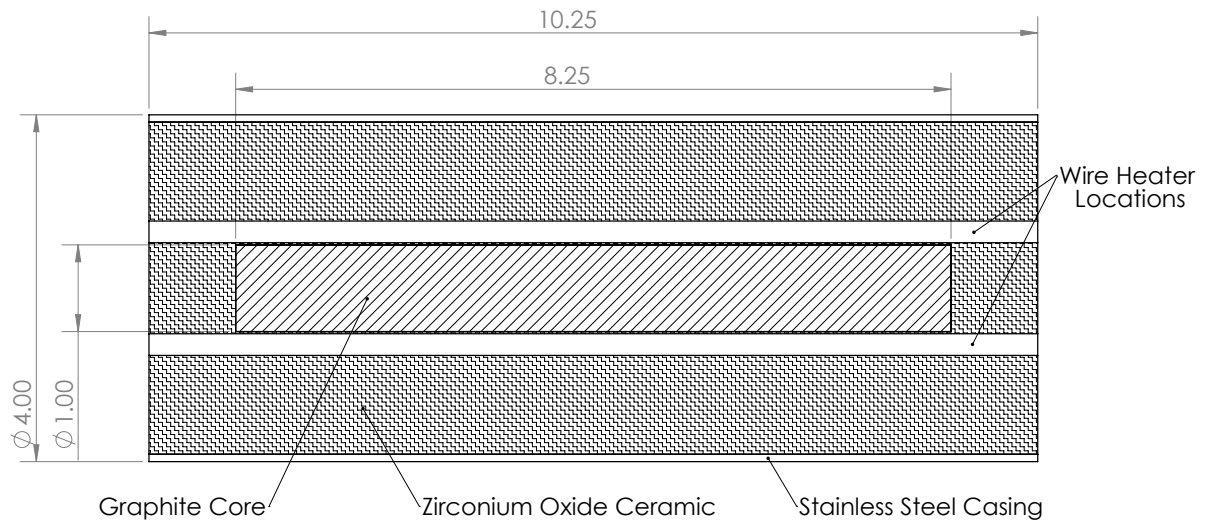
Figure 9.4: Cutaway diagram of an initial resistive heating experiment using low-cost materials to reach molten silicon temperatures. The cylindrical test section was able to achieve molten silicon temperatures across the entire graphite core with a power input of 1400 W.

graphite core but required approximately 1400 W of power. With a desired convective draw of 430 W, environmental losses would dominate the system and provide little insight into convective coupling effects on the silicon storage medium.

It is proposed that the desired quasi-adiabatic conditions are possible with low-cost materials by implementing precise control of the resistive heater. As a simplified case, consider a 1-D slice of the assembly given in Figure 9.4. Thermocouples placed at the edge of the graphite core and within the heater assembly can be used to determined the heat flux across the core boundary. Since the materials and geometry are known, radial conduction equations can be solved simultaneously with the outer boundary condition for the heater power required to maintain a zero heat flux condition. As the core is cooled by the propellant stream, real time calculations can be used to drop the power level in the heater so that the boundary follows the core temperature and maintains a zero flux condition. In the experimental system, accurate thermal control would require real-time calculation of 3-D heat transfer conditions and the resistive heater assembly would have to be divided into multiple controllable segments to accommodate asymmetric heat loss as the PCM is cooled.

141

9.2   Potential Solar Furnace Improvements

The USC solar furnace facility is currently capable of molten silicon based experiments and is well suited for silicon thermal energy storage testing targeting terrestrial thermophotovoltaic systems. In order to mount larger scale experiments and potentially reach molten boron temperatures, furnace improvements are necessary. The heliostat is currently the least efficient component of the solar furnace and replacing the current reflector with commercially available first surface mirrors will increase the power delivery and concentration ratio of the furnace by 30%. Since the heliostat is permanently mounted outdoors, special care will be required to preserve the surface of the new reflector. Careful engineering and a protective cover for when the system is off line can prevent damage from the elements.

Another route to improving the performance of the solar furnace is the addition of a secondary concentrator. Adding a compound parabolic concentrator (CPC) to the system can approximately double the concentration ratio and increase experimental temperatures to where small scale molten boron testing is feasible. Based on the parametric equations for a CPC given by Weldord and Winston, adding a secondary concentrator with an overall reflective efficiency of 80% could increase peak concentration ratios for the solar furnace to approximately 9,600:1 [131]. By combining a CPC with new heliostat mirror panels, concentration ratios above 10,000:1 can certainly be achieved making molten boron experiments possible.

9.3   Developmental Roadmap

The latent heat thermal energy storage component of a high performance bi-modal solar thermal microsatelite has been identified as both an enabling and under-developed technology. This work has succeed in demonstrating the basic feasibility of a silicon based thermal energy storage system and identified key technological hurdles and practical engineering concerns. While the long term goal of future research efforts should be focused on the design and test of a microsatellite scale

142

bi-modal system, key near term research goals must be met before sensible engineering decisions can be made. The following points present the chief design concerns from both this work and the existing literature.

- Expansion damage is the primary extant concern for mounting an effective silicon based thermal energy storage system. This work has demonstrated successful results with reduced fill factors in cylindrical geometries. However, results are limited to the specific tests performed. A combined experimental and analytical approach is recommended to vary geometries and explore the conical container sections proposed in the terrestrial literature by Chubb, Datas, and Veeraragavan [5, 95, 96]. It is important to note that freezing asymmetry, highlighted in this work, necessitates that future experiments emulate the environmental heat loss profile that would be seen in a real system as opposed to uniform furnace testing.

- This work proposes the use of high density graphite containers for molten silicon thermal energy storage based on a survey of the available literature and demonstrated short-term performance in solar furnace tests. Future study is required to quantify both contamination levels and repeatability of this combination across thousands of cycles. Automated furnace tests using varying grades of graphite must be conducted while accurately measuring latent heat release, preferably with a power draw profile simulating a propellant / working fluid blowdown.

- The proper design of a high temperature PCM based heat exchanger must consider the convective coupling profile in addition to total PCM mass as demonstrated by STAR-CCM+ models of the conjugate heat transfer system. An extended modeling effort is required to determine the relationship between effective energy storage density and multiple variables such as heat exchanger diameter and length, mass flow rate and working fluid. The resulting data set will allow mission designers to easily trade effective energy storage density with other design parameters without the use of time consuming transient heat transfer models.

143

- Molten boron experiments were outside the scope and budget of this research effort. However, the ultimate solar thermal bi-modal system requires boron based thermal energy storage to see the proposed 35-60% increase in ΔV capability vs. competing chemical systems. The first stages of molten boron research should focus on a reliable container design capable of surviving multiple cycles using the proposed combination of boron nitride liners and sealed graphite containers. Following these tests, design of a molten boron heat exchanger can draw from convective coupling relations established via molten silicon system development.

144

<div align="right">

Chapter 10

</div>

Conclusions

The promise of high thrust and high efficiency has driven decades of research into solar thermal propulsion (STP). However, despite multiple flight development programs and multiple statements of feasibility with existing technology, no STP spacecraft systems have flown to-date. Perceived and actual system complexity, coupled with vehicle integration concerns overshadow the utility of STP and the benefits of a mid-range I_{sp}, high thrust propulsion mechanism are not enough to outweigh technological and mission uncertainty.

As solar thermal propulsion has progressed, the trend has been toward miniaturization as well as simplification and the latest research efforts have targeted microsatellite systems. In the framework of a high performance microsatellite that requires both quick response time and large ΔV delivery, an STP system fills a unique role that cannot be matched with conventional propulsion technologies. Implementation of an STP system at the microsatellite scale has the potential for a greater than $50\% \ \Delta V$ increase while maintaining response times that can be measured in days. In this case, the risk of a novel flight mechanism is outweighed not by an incremental improvement, but by the enabling of a new class of high performance, low cost spacecraft.

Proper implementation of solar thermal propulsion on board a microsallite requires a bi-modal configuration to both reduce system complexity and provide acceptable propulsion and power mass fractions. In this scenario, the thermal sub-systems on the spacecraft provide both propulsive and

electric power and a review of current technology shows that ready solutions are available for the majority of the necessary spacecraft systems with the exception of high performance thermal energy storage.

Throughout the history of solar thermal propulsion, thermal energy storage has been primarily an afterthought baring the bi-modal development programs of the 1990s. Designs have settled on sensible heat based systems even though the literature frequently mentions the benefits of latent heat thermal energy storage. This work represents the most thorough investigation of high temperature latent heat thermal energy storage to date confirming both the potential gains achievable and the basic feasibility of the concept.

An experimental approach was taken to uncover practical engineering concerns culminating in the first molten silicon experiments exploring the thermal energy storage problem. Experiments conducted with a newly developed solar facility succeeded in the short term demonstration of potential container materials and highlighted the asymmetry of the silicon freezing process in a real world system. Asymmetric freezing and container damage due to freezing expansion were identified as the most pressing engineering concerns for silicon based thermal energy storage and the reduction of container fill factor has been demonstrated as a viable solution in cylindrical geometries at the expense of energy storage density.

Experimental results were also used to validate an in-house MATLAB model of the experiment using the "enthalpy method" for calculating the phase change process. Despite the complexities of of the silicon freezing process, simplified modeling methods are able to capture essential system behaviors.

Ultimately, this work provides a technological basis for future design efforts by proving the basic feasibility of a molten silicon based thermal energy storage system and presenting multiple pathways for future development.

Reference List

[1] Scharfe, D. and Ketsdever, A., "A Review of High Thrust, High Delta-V Options for Microsatellites Missions," *45th AIAA/ASME/SAE/ASEE Joint Propulsion Conference*, No. AIAA-2009-4824, American Institute of Aeronautics and Astronautics, Denver, CO, August 2009.

[2] Wertz, J. R., editor, *Space Mission Engineering: The New SMAD*, Microcosm Press, 2011.

[3] Kennedy, F., *Solar Thermal Propulsion for Microsatellite Manouevering*, Doctoral thesis, University of Surrey, Guildford, Surrey, UK, September 2004.

[4] Ethridge, F. G., *Solar Rocket System Concept Analysis*, Rockwell International Final Report, AFRPL-TR-79-79, December 1979.

[5] Chubb, D. L., Good, B. S., and Lowe, R. A., "Solar Thermophotovoltaic (STPV) System With Thermal Energy Storage," *The 2nd NREL Conference on Thermophotovoltaic Generation of Electricty*, Colorado Springs, CO, July 1995.

[6] Ehricke, K. A., "The Solar-Powered Space Ship," *Semi-Annual Meeting of the American Rocket Society*, No. ARS Paper 310-56, Cleveland, OH, 1956.

[7] Selph, C. C., "The Place of Solar Thermal Rockets In Space," *JANNAF Propulsion Meeting*, New Orleans, LA, May 1981.

[8] Shoji, J. M., *Solar Rocket Component Study*, Rockwell International - Rocketdyne Division, Final Report, AFRPL-TR-84-057, February 1985.

[9] Shoji, J. M., "Performance Potential of Advanced Solar Thermal Propulsion," *19th AIAA/SAE/ASME Joint Propusion Conference*, Seattle, WA, June 1983.

[10] Laug, K., "The Solar Propulsion Concept is Alive and Well at the Astronautics Laboratory," *JANNAF Propulsion Meeting*, Cleaveland, OH, May 1989.

[11] Shoji, J. M., Frye, P. E., and McClanahan, J. A., "Solar Thermal Propulsion Status and Future," *AIAA Space Programs and Technologies Conference*, Huntsville, AL, March 1992.

[12] Shoji, J., Frye, P., Chwiedor, T., and Lim, D., "Advanced Absorber/Thruster Concepts For Solar Thermal Propulsion," *ASME Joint Solar Engineering Conference*, New York, NY, 1993.

[13] Fitzsimmons, M. J., "Technology Considerations For Future Upper Stages," *AIAA Space Programs and Technologies Conference*, Huntsville, AL, 1994.

[14] Zubrin, R. M., Sulmeisters, T. K., Jacox, M. G., and Watts, K., "The Integrated Power and Propulsion Stage: A Mission Driven Solution Utilizing Thermionic Technology," *Proceedings of the Ninth Symposium On Space Nuclear Power Systems*, Alburquerqe, NM, January 1992.

[15] Culver, D., Kolganov, V., D'Yakov, E., and Daragan, I., "Low Cost Space Power: High Performance Nuclear Bimodal System With Flexible Growth Options From Demonstrated Technologies," *30th AIAA/ASME/SAE/ASEE Joint Propulsion Conference*, Indianapolis, IN, June 1994.

[16] Kennedy, F., "Bimodal Power and Propulsion System Requirements," *31st AIAA/ASME/SAE/ASEE Joint Propulsion Conference and Exhibit*, San Diego, CA, July 1995.

[17] Laug, K. K., Holmes, M. R., and Westerman, K. O., *Solar Bi-Modal System Concept: Mission Applications, A Preliminary Assessment*, Technical Paper, Air Force Research Lab Propulsion Directorate, Wright-Patterson AFB, OH, 1992.

[18] Malloy, J. D., Rochow, R. F., and Inman, J. B., "Hybrid Solar Rocket Utilizing Thermal Storage For Propulsion And Electrical Power," US Patent No. 5,459,996, 1995.

[19] Kennedy, F. and Jacox, M., "The Integrated Solar Upper Stage (ISUS) Program," *AIAA 1995 Space Programs and Technologies Conference*, American Institute of Aeronautics and Astronautics, Huntsville, AL, September 1995.

[20] Harper, W. B. and Shatlens, R. K., "NASA Solar Dynamic Ground Test Demonstration (GTD) Program And Its Application To Space Nuclear Power," *10th Symposium on Space Nuclear Power and Propulsion*, Alberquerque, NM, January 1993.

[21] Partch, R. and Frye, P., "Solar Orbit Transfer Vehicle Conceptual Design," *35th AIAA/ASME/SAE/ASEE Joint Propulsion Conference*, No. AIAA-1999-2476, American Institute of Aeronautics and Astronautics, Los Angeles, CA, 1999.

[22] Kerslake, T. W. and Ibrahim, M. B., "Analysis of Thermal Energy Storage Material With Change-of-Phase Volumetric Effects," *Journal of Solar Energy Engineering*, Vol. 115:1, February 1993, pp. 22–31.

[23] Miles, B. J., "Development and Testing of High Temperature Coatings for the Integrated Solar Upper Stage Thermal Energy Storage System," *Space Technology and Applications International Forum*, Alburquerque, NM, January 1997.

[24] Kudija, C., "The Integrated Solar Upper Stage (ISUS) Engine Ground Demonstrator (EGD)," *32nd AIAA/ASME/SAE/ASEE Joint Propulsion Conference and Exhibit*, Lake Buena Vista, FL, July 1996.

[25] Frye, P. E. and Kudija, C., "Integrated Solar Upper Stage Engine Ground Demonstration Test Results and Data Analysis," *34th AIAA/ASME/SAE/ASEE Joint Propulsion Conference*, No. AIAA-1998-3958, American Institute of Aeronautics and Astronautics, 1998.

[26] Wyant, F. J., Luke, J. R., and Luchau, D. W., "START-3: Operational Evaluations of the ISUS Engine Ground Demonstration Thermionic Power System," *Space Technology and Applications International Forum*, Alberquerque, NM, Jan-Feb 1999.

[27] Kennedy, F., Palmer, P., and Paul, M., "Results of Microscale Solar Thermal Engine ground Test Campaign at the Surrey Space Center," *40th AIAA/ASME/SAE/ASEE Joint Propulsion Conference*, No. AIAA-2004-4137, American Institute of Aeronautics and Astronautics, Fort Lauderdale, FL, 2006.

[28] Wassom, S. R., *Focus Control System for Solar Thermal Propulsion*, Technical Paper, Thiokol Propulsion, Brigham City, UT, ADA410345.

[29] Frye, P. E. and and, F. K., "Reusable Orbital Transfer Vehicles (ROTV): Applications of an Integrated Solar Upper Stage (ISUS)," *33rd AIAA/ASME/SAE/ASEE Joint Propulsion Conference*, No. AIAA-1997-2981, American Institute of Aeronautics and Astronautics, Seattle, WA, 1997.

[30] Carroll, J., "Solar Orbit Transfer Vehicle," *AIAA Space Conference*, No. AIAA-2000-5110, American Institute of Aeronautics and Astronautics, Long Beach, CA, 2000.

[31] Holmes, M., "Solar Rocket Propulsion: Ground and Space Technology Demonstration," *12th Annual Advanced Space Propulsion Workshop*, Hunstsville, AL, 2001.

[32] Tucker, S. and Salvail, P., "Solar-Thermal Engine Testing," *Space Technology and Applications International Forum*, Alburquerque, NM, February 2002.

[33] Gerrish, H., Schmidt, G., and Rodgers, S., "Advanced Propulsion Research at Marshall Proulsion Research Center," *37th Joint Propulsion Conference and Exhibit*, Salt Lake City, UT, July 2001.

[34] Kennedy, F. and Palmer, P. L., "Preliminary Design of Micro-Scale Solar Thermal Propulsion System," *38th AIAA/ASME/SAE/ASEE Joint Propulsion Conference*, No. AIAA-2002-3928, American Institute of Aeronautics and Astronautics, Indianapolis, IN, July 2002.

[35] Henshall, P., "Fibre Optic Solar Thermal Propulsion Technology Demonstrtation," *Surrey Space Centre, School of Electronis and Physical Sciences*, University of Surrey, March 2006.

[36] Henshall, P., *A Proposal to Develop and Test a Fibre-Optic Coupled Solar Thermal Proulsion System for Microsatellites*, University of Surrey. AF Contract FA8655-04-1-3030 Final Report., 2006.

149

[37] Nakamura, T., Sullivan, D., and McCalahan, J., "Solar Thermal Propulsion for Small Spacecraft," *40th AIAA/ASME/SAE/ASEE Joint Propulsion Conference*, No. AIAA-2004-4138, American Institute of Aeronautics and Astronautics, Fort Lauderdale, FL, July 2004.

[38] Sahara, H. and Shimizu, M., "Solar Thermal Propulsion System for Microsatellite Orbit Transferring," *40th AIAA/ASME/SAE/ASEE Joint Propulsion Conference*, No. AIAA-2004-3764, American Institute of Aeronautics and Astronautics, Fort Lauderdale, FL, July 2004.

[39] Colonna, G., Capitta, G., Capitelli, M., Wysong, I., and Kennedy, F., "Model for Ammonia Solar Thermal Thruster," *Journal of Thermophysics and Heat Transfer.*, Vol. 20, No. 4, October-December 2006.

[40] Pearson, J., Gierow, P., and Lester, D., "Near Term In-Space Demonstration of an Inflatable Concentrator," *Proceedings of the 37th AIAA Aerospace Sciences Meeting*, Reno, NV, January 1999, pp. 11–14.

[41] Pearson, J. C., Lester, D. M., Holmes, M. R., and Wong, W. A., *Solar Thermal Vacuum Testing of an Integrated Membrane Concentrator System at the NASA GRC Tank 6*, SRS Technologies - Technical Report, Huntsville, AL, June 2003.

[42] Shatlens, R. K. and Mason, L. S., "Early Results from Solar Dynamic Space Power Testing," *Journal of Propulsion and Power*, Vol. 12, No. 5, October 1996, pp. 852–858.

[43] Borell, G. J. and Campbell, J. S., "ISUS Solar Concentrator Array Development," *32nd AIAA, ASME, SAE and ASEE Joint Propulsion Conference and Exhibit*, Lake Buena Vista, FL, July 1996.

[44] Holmes, M. R. and Laug, K. K., "Dependence of Solar-Thermal Rocket Performance on Concentrator Performance," *Journal of Solar Engineering*, Vol. 2, 1995, pp. 837–848.

[45] ESA, *Herschel Observer's Manual.*, Version 5, HERSCHEL-HSC-DOC-0876.

[46] Space, M. and Group, D., *Type 22 Antenna Pointing Assembly Data Sheet*, Chatsworth, CA, 2010.

[47] Hyder, A. K., Halpert, R. L., Halpert, G., Flood, D. J., and Sabripour, S., *Spacecraft Power Technologies*, Imperial College Press, London, 2000.

[48] Gilpin, M., Scharfe, D., Young, M., and Pancotti, A., "Molten Boron Phase-Change Thermal Energy Storage: Containment and Applicability to Microsatellites," *42nd AIAA Thermophysics Conference*, No. AIAA-2011-3637, American Institute of Aeronautics and Astronautics, 2011.

[49] Preijde, J., *Design of a Solar Thermal Power-Propulsion System for a Small Satellite*, Master's thesis, Delft University of Technology, January 2015.

[50] Stone, K. W., Fatemi, N. S., and Garverick, L. M., "Operation and Testing of a Solar Thermophotovoltaic Power System," *25th IEEE Photovoltaic Specialists Conference*, Washington, DC, May 1996.

[51] Stone, K., Leingang, E., Drubka, R., Chubb, D., Good, B., and Wilt, D., "System Performance of a Solar Themophotovoltaic System for Space and Terrestrial Applicaions," *Intersociety Energy Conversion Engineering Conference*, Vol. 1, 1995, pp. 713–718.

[52] Horne, E., "Hybrid Thermophotovoltaic Power Systems," Final Report P500-02-048F, California Energy Commission, 2002.

[53] Kessler, T., "An Overview of a Solar Thermal Propulsion and Power System Demonstration Applicable to HEDS," *AIAA Space 2001 Conference*, No. AIAA-2001-4777, Albuquerque, NM, August 2001.

[54] Lyons, V. J., Gonzolez, G. A., Houts, M. G., Iannello, C. J., Scott, J. H., and Surampudi, S., *Space Power and Energy Storage Roadmap*, NASA, April 2012.

[55] Wei, G. and Robbins, J., *Development and Characterization of Carbon-Bonded Carbon Fiber Insulation for Radioisotope Space Power Systems*, No. ORNL/TM-9381, Oak Ridge National Labratory and Martin Marietta, 1985.

[56] Baxter, R. I., Rawlings, R. D., Iwashita, N., and Sawada, Y., "Effect of Chemical Vapor Infiltration on Erosion and Thermal Properties of Porous Carbon/Carbon Composite on Thermal Insulation," *Carbon*, Vol. 38, No. 3, 2000, pp. 441–449.

[57] Gallego, N. C. and Klett, J. W., "Carbon Foams for Thermal Management," *Carbon*, Vol. 41, 20013, pp. 1461–1466.

[58] Gasch, M., Ellerby, D., Irby, E., Beckman, S., Gusman, M., and Johnson, S., "Processing, Properties and Arc Jet Oxidation of Hafnium Diboride/Silicon Carbide Ulatra High Temperature Ceramics," *Journal of Materials Science*, Vol. 39, No. 19, 2004, pp. 5925–5937.

[59] Lide, D. R., *CRC Handbook of Chemistry and Physics*, Boca Raton, FL, 77th ed., 1996.

[60] "Hot Pressed BN Shapes Data Sheet," Momentive Performance Materials Inc., Strongsville, OH, 2012.

[61] Gilpin, M., Scharfe, D., Young, M., and Pancotti, A., "Molten Boron Phase-Change Thermal Energy Storage to Augment Solar Thermal Propulsion Systems," *47th AIAA/ASME/SAE/ASEE Joint Propulsion Conference*, No. AIAA-2011-5986, American Institute of Aeronautics and Astronautics, San Diego, CA, 2011.

[62] "Rescor Castable Ceramics," Cotronics Corp., New York, NY, 2008.

[63] "Calcarb Rigid Carbon Thermal Insulation Tehcnical Guide," MERSEN USA, Bay City, MI, 2009.

[64] "Ultramet Carbon Foam Data Sheet," Ultramet, Pacoima, CA, 2014.

[65] Glazer, S. D., *Multifoil Insulation Study for Weight Reduction*, No. JPL D-1268, NASA Jet Propulsion Laboratory, January 1984.

[66] Westerman, K. O. and Barry, "Testing of a Receiver-Absorber-Converter (RAC) for the Integrated Solar Upper Stage (ISUS) Program," *Space Technology and Applications International Forum*, Albuquerque, NM, January 1998.

[67] Chase, M. W., editor, *NIST-JANAF Thermochemical Tables 2 Volume-Set (Journal of Physical and Chemical Reference Data Monographs)*, American Institute of Physics, 1998.

[68] Lynch, J., Ruderer, C., and Duckworth, W., editors, *Engineering Properties of Selected Ceramic Materials*, The American Ceramic Society, Columbus, OH, 1966.

[69] Kenisarin, M. and Mahkamov, K., "Solar Energy Storage Using Phase Change Materials," *Renewable and Sustainable Energy Reviews*, Vol. 11, 2007, pp. 19113–1965.

[70] Zalba, B., Marin, J., Cabeza, L., and Mehling, H., "Review on Thermal Energy Storage with Phase Chamge: Materials, Heat Transfer Analysis and Applications," *Applied Thermal Engineering*, Vol. 23, 2003, pp. 251–283.

[71] Ho, C., Powell, R., and Liley, P., "Thermal Conductivity of the Elements: A Comprehensive Review," *Journal of Physical and Chemical Reference Data*, Vol. 3, 1974.

[72] Koyama, K., "Thermal Conductivity of Magnesium Flouride Between 25 and 900 C," *Journal of the American Ceramic Socitey*, Vol. 52, No. 4, June 2006.

[73] Glassbrenner, C. and Slack, G. A., "Thermal Conductivity of Silicon and Germanium from 3 K to the Melting Point," *Physical Review*, Vol. 134, No. 4A, May 1964, pp. A1058–A1069.

[74] Cooper, H. S., *Rare Metals Handbook*, Reinhold, London, 2nd ed., 1961.

[75] Jansen, L. H., editor, *Kirk-Othmer Encyclopedia of Chemical Technology*, Vol. 14, Wiley InterScience, New York, 5th ed., 2004.

[76] Sands, D. and Hoard, J., "Rhombohedral Elemental Boron," *Journal of the American Chemical Society*, Vol. 79, October 1957, pp. 5582–5583.

[77] Hoard, J., "Remarks on Structure and Polymorphism in Boron," *Proceedings of the 1st International Symposium on Boron*, Asbury Park, NJ, 1959.

[78] Amundson, T. R., *Computational Evaluation of the Effects of Voids on a Thermal Energy Storage System in a Combined Solar Power and Propulsion System*, Master's thesis, University of Colorado Colorado Springs, 2013.

[79] Gilpin, M., Scharfe, D., and Young, M., "Phase-Change Thermal Energy Storage and Conversion: Development and Analysis for Solar Thermal Propulsion," *48th AIAA/ASME/SAE/ASEE Joint Propulsion Conference*, No. AIAA-2012-3715, American Institute of Aeronautics and Astronautics, Atlanta, GA, 2012.

[80] Frye, P., "Integrated Solar Upper Stage (ISUS) Space Demonstration Design," *Space Technology and Applications International Forum (STAIF - 97)*, Albaquerque, NM, Jan 1997.

[81] Nakamura, T., Sullivan, D., McClanahan, A., Shoji, J., Partch, R., and Quinn., S., "Solar Thermal Propulsion for Small Spacecraft - Engineering System Development and Evaluation," *41st AIAA/ASME/SAE/ASEE Joint Propulsion Conference*, No. AIAA-2005-3923, American Institute of Aeronautics and Astronautics, Tucson, AZ, 2005.

[82] Mueller, J., "Thruster Options for Microspacecraft: A Review and Evaluation of Existing Hardware and Emerging Technologies," Tech. Rep. AIAA-97-3058, AIAA, 1997.

[83] Astrium, E., 1N Hydrazine Thruster, Technical Specifications: http://cs.astrium.eads.net.

[84] Astrium, E., 20 N Hydrazine Thruster, Technical Specifications: http://cs.astrium.eads.net.

[85] Biagioni, L., Cesari, U., and Saverdi, M., "Development Status of the HT-100 Miniaturized Hall Effect Thruster System," *41st AIAA/ASME/SAE/ASEE Joint Propulsion Converence & Exhibit*, Tucson, AZ, July 2005.

[86] Brown, C., *Spacecraft Propulsion*, AIAA, Reston, VA, 1st ed., 1996.

[87] Larson, W. and Wertz, J., editors, *Space Mission Engineering: The New SMAD*, Microcosm Press, 1st ed., 2011.

[88] "NASA Technology Roadmaps: Propulsion and Power Workshop," Tech. rep., Aeronautics and Space Engineering Board, National Research Council, March 2012.

[89] Strumpf, H. and Coombs, M., "Solar Reciever Experiment for the Space Station Freedom Brayton Engine," *Journal of Solar Energy En*, Vol. 112, 1990, pp. 12–18.

[90] Abbott, R., "MultiUse Solar Thermal Power Generators," *Space Technology and Applications International Forum*, Alburquerque, NM, February 2001.

[91] Calabro, M., "Solar Thermal Upper Stages," *International Conference on Recent Advances in Space Technologies*, Istanbul, Turkey, November 2003.

[92] Jerred, N., Howe, T., Howe, S., and Rajguru, A., "Dual-Mode Propulsion System Enabaling Cubesat Exploration of the Solar System," Tech. rep., NASA Inovative Advanced Concepts: Phase 1 Final Report, 2014.

[93] Woodall, "Energy Conversion," US Patent No. 4,316,048, 1982.

[94] Stone, K. W., Schneider, S., and Schmitt, R. J., "Solar Thermophotovoltaic Power Conversion Method and Apparatus," 1999'.

[95] Datas, A., Chubb, D., and Veeraragavan, A., "Steady State Analysis of A Storage Integrated Solar Thermophotovoltaic (SISTPV) System," *Solar Energy*, Vol. 96, 2013, pp. 33–45.

[96] Veeraragavan, A., Montgomery, L., and Datas, A., "Night Time Performance of a Storage Integrated Solar Thermophotovoltaic (SISTPV) System," *Solar Energy*, Vol. 108, 2014, pp. 377–389.

[97] Hukuo, N., "Design Problems of a Solar Furnace," *The Proceedings of the Solar Furnace Symposium*, Association for Applied Solar Energy, 1957.

[98] Michalsky, J. J., "The Astronomical Almanac's Algorithm For Approximate Solar Position (1950-2050)," *Solar Energy*, Vol. 40, No. 3, 1988, pp. 227–235.

[99] Meeus, J., *Astonomical Algorithms*, Willmann-Bell, Inc., 2009.

[100] Strachan, J. W. and Houser, R. M., "Testing and Evaluation of Large-Area Heliostats for Solar Thermal Applications," Tech. rep., Sandia National Laboratories, Albuquerque, NM, February 1993.

[101] Haueter, P., Steitz, T., and Steinfeld, A., "A New High-Flux Solar Furnace for High-Temperature Thermochemical Research," *Journal of Solar Engery Engineering*, Vol. 121, 1999, pp. 77–80.

[102] Ries, H. and Schubnell, M., "The Optics of a Two-Stage Solar Furnace," *Solar Energy Materials*, Vol. 21, 1990, pp. 213–217.

[103] Muggleton, A. and Howe, F., "The Preparation of Thin Self Supporting Boron Films," *Nuclear Instruments and Methods*, Vol. 13, August-October 1961, pp. 211–214.

[104] Searcy, A. W. and Myers, C. E., "The Heat of Sublimation of Boron and Gaseous Species of the Boron-Boric Oxide System," *Journal of Physical Chemistry*, Vol. 67, No. 7, July 1957, pp. 957–960.

[105] Storms, E. and Mueller, B., "Phase Relations and Thermodynamic Properties of Transition Metal Borides. I. The Molybdenum-boron system and Elemental Boron," *Journal of Physical Chemistry*, Vol. 81, 1977, pp. 318–324.

[106] Leitnaker, J. M. and Bowman, M. G., "High-Temperature Phase Studies in the Tantalum-Boron System between Ta and TaB," *Journal of the Electrochemical Society*, Vol. 108, No. 6, June 1961, pp. 568–572.

[107] Itoh, H., Matsudaira, T., and Naka, S., "Formation Process of Tungsten Borides by Soild State Reaction Between Tungsten and Amorphous Boron," *Journal of Materials Science*, Vol. 22, No. 8, 1987, pp. 2811–2815.

[108] Steinitz, R., Binder, I., and Moskowitz, D., "System Molybdenum-Boron and Some Properties of The Molybdenum-Borides," *Journal of Metals*, September 1952, pp. 983–988.

[109] Stout, N. D., Mar, R. W., and Boo, W. O., "The High-Temperature Enthalpy of Fusion of Boron by Drop Calorimetry," *High Temperature Science*, Vol. 5, No. 4, August 1973, pp. 241–251.

[110] Wald, F. and Stormont, R. W., "Investigations on the Constitution of Certian Binary Boron-Metal Systems," *Journal of the Less Common Metals*, Vol. 9, No. 6, December 1965, pp. 423–433.

[111] Kimpel, R. F. and Moss, R. G., "Melting Point of 98.9 to 99.6% Pure Boron," *Journal of Chemical Engineering Data*, Vol. 13, No. 2, April 1968, pp. 231–234.

[112] Mar, R., "High-temperature Thermal Analysis of High Boron Alloys Using Automatic Optical Pyrometry," *Thermochimica Acta*, Vol. 4, No. 3-5, August 1972, pp. 367–376.

[113] Hildenbrand, D. L. and Hall, W., "The Vaporization Behavior of Boron Nitride and Aluminum Nitride," *Journal of Physical Chemistry*, Vol. 67, No. 4, April 1963, pp. 888–893.

[114] Fesenko, V. and Bolgar, A., "Evaporation Rate and Vapor Pressure of Carbides, Silicides, Nitrides and Borides," *Power Metallurgy and Metal Ceramics*, Vol. 2, No. 1, January 1964, pp. 11–17.

[115] Paine, R. and Narula, C., "Synthetic Routes to Boron Nitride," *Chemical Reviews*, Vol. 90, No. 1, January 1990, pp. 73–91.

[116] Patrick, W. J., Scilla, S. J., and Westdrop, W. A., "Controlling the Oxygen Content of Czochralski Process of Silicon Crystals By Sandblasting Silica Vessel," US Patent No.4,010,064, 1977.

[117] Ciszek, T., Schwuttke, G., and Yang, K., "Directionally Solidified Solar-Grade Silicon Using Carbon Crucibles," *Journal of Crystal Growth*, Vol. 46, 1979, pp. 527–533.

[118] Drevet, B., Voytovych, R., Israel, R., and Eustathopoulous, N., "Wetting and Adhesion of Si on Si_3N_4 and BN substrates," *Journal of the European Ceramic Society*, Vol. 29, February 2009, pp. 2363–2367.

[119] Wang, L., Clancy, P., Thompson, M., and Murthy, C., "Thermodynamic and Kinetic Studies of Laser Thermal Processing of Heavily Boron-Doped Amorphous Silicon Using Molecular Dynamics," *Journal of Applied Physics*, Vol. 92, No. 5, September 2002, pp. 2412–2419.

[120] Enriquez, O., Marin, A., Winkels, K., and Snoeijer, J., "Freezing Singularities in Water Drops," *Physics of Fluids*, Vol. 24, 2012.

[121] Rhim, W.-K. and Ohsaka, K., "Thermophysical Properties Measurements of Molten Silicon by High-Temperature Electrostatic Levitator: Density, Volume Expansion, Specific Heat Capacity, Emissivity, Surface Tension and Viscosity," *Journal of Crystal Growth*, Vol. 208, 1999, pp. 313–321.

[122] Steinfeld, A. and Fletcher, E. A., "A Spherical Reciever-Reactor with Specularly Reflecting Inner Surfaces for High-Temperature Solar Furnace Applications," *Proceedings of the Nineth International Heat Transfer Conference*, Jerusalem, Israel, 1990, pp. 127–132.

[123] Touloukian, Y., editor, *Thermophysical Properties of Matter - The TPRC Data Seires*, Purdue University, 1971.

[124] Incropera, F. P., DeWitt, D. P., Bergman, T. L., and Lavine, A. S., *Introduction to Heat Transfer*, Wiley, 2006.

[125] Elgafy, A. and Mesalhy, O., "Numerical and Experimental Investigations of Melting and Solidification Processes of High Melting Point PCM in a Cylindrical Enclosure," *Journal of Heat Transfer*, Vol. 126, October 2004, pp. 869–875.

[126] Burmeister, L. C., *Convective Heat Transfer*, Wiley-Interscience, 1993.

[127] Hollahan, J. R. and Gregory, N., "A Torsion Effusion Study of the Reaction of Graphite with Oxides of Thorium and Zirconium," *The Journal of Physical Chemistry*, Vol. 68, August 1964, pp. 2346–2351.

[128] Kobatake, H., Fukuyama, H., Minato, I., Tsukada, T., and Awaji, S., "Noncontact Measurement of Thermal Conductivity of Liquid Silicon In A Static Magnetic Field," *Applied Physics Le*, Vol. 90, 2007.

[129] Oswald, M., Turek, M., and Bagdahn, J., "Numerical Simulations of Thermo-Mechanical Stresses During The Casting of Multi-Crystaline Silicon Ingots," *11th. Int. Conf. on Thermal, Mechanical and Multiphysics Simulation and Experiments in Micro-Electronics and Micro-Systems*, Bordeaux, France, April 2010.

[130] Ciszek, T. F. and Schwuttke, G. H., "Method for Directional Solidification of Silicon," US Patent No. 4,243,471, 1981.

[131] Welford, W. and Winston, R., *The Optics of Nonimaging Concentrators*, Academic Press, Inc., New York, NY, 1st ed., 1978.

Matlab Model Formulation

Interior heat transfer for the MATLAB model discussed in Chapter 7 is handled via a 2-D axisymmetric (r,z) conduction formulation. An energy balance method is used to calculated transient conduction and the enthalpy method is used to accommodate the phase change process [124, 125]. Consider a single node (m, n) as defined in Figure A.1.

During each time step, dt, heat transfer via conduction is calculated between node (m, n) and the four surrounding nodes to determine the net heat transfer

$$q_{net,(m,n)} = q_{up,(m,n)} + q_{down,(m,n)} + q_{left,(m,n)} + q_{right,(m,n)} \tag{A.1}$$

Exterior nodes have additional q_{rad} and q_{conv} terms taking into account radiation and convection respectively and negate conduction terms when no adjacent node exists.

For nodes not containing a phase change material, the temperature change for the specified dt is then calculated as

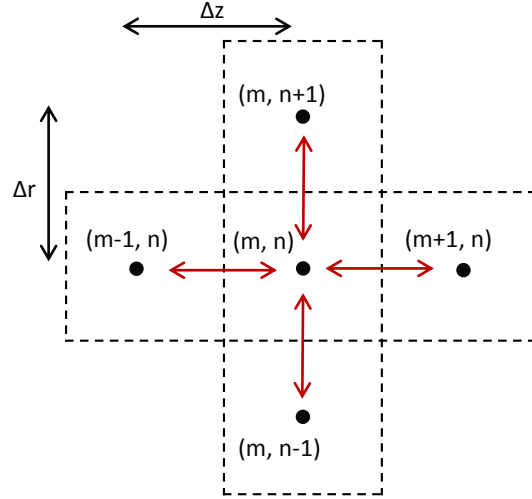$$\Delta T_{(m,n)} = \frac{q_{net,(m,n)}dt}{m_{(m,n)}c_{p,(m,n)}} \tag{A.2}$$

157

Figure A.1: Diagram illustrating node (m, n) and the adjacent nodes used for computations

For nodes that do contain a phase change material, the "enthalpy method" is used to approximate the phase change process. Each node is assigned a latent heat reservoir based on the mass of PCM within the node. When the temperature of the node is within the "mushy zone" $(T_{melt} \pm 0.1K)$, all heat transfer is assigned to the phase change process and the temperature of the node is kept constant

$$
\Delta T(m, n) = \begin{cases} 0, & T_{melt} - 0.1 \leq T_{(m,n)} \leq T_{melt} + 0.1 \\ \frac{q_{net,(m,n)}dt}{m_{(m,n)}c_{p,(m,n)}}, & otherwise \end{cases}
\tag{A.3}
$$

$$
L_{f,(m,n)} = L_{f,(m,n)} + q_{net,(m,n)}
\tag{A.4}
$$

When the latent heat reservoir value is either depleted in the case of cooling, or reaches a maximum value in the case of heating, the node is considered either completely solid or completely liquid and the node is allowed to change temperature out of the "mushy zone."
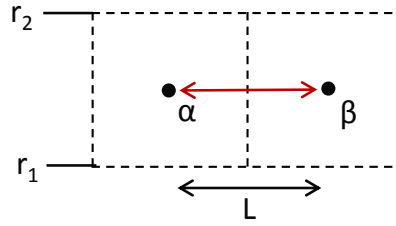
158

Figure A.2: Diagram illustrating two adjacent nodes in the z direction

The conduction equations used to calculate heat transfer between adjacent nodes assume one-dimensional steady state condition for either a plane wall in the z direction, or a radial system in the case of conduction in the r direction.

For conduction in the z direction, consider two adjacent nodes α and β as shown in Figure A.2. Heat transfer from node α to node β can be defined as

$$q_{\alpha\beta} = \frac{\pi(r_2^2 - r_1^2)(T_\alpha - T_\beta)}{L(1/k_\alpha + 1/k_\beta)} \tag{A.5}$$

with L defined as the distance between nodes, r_1 and r_2 as the upper and lower node radii, T as the node temperature, and k as the thermal conductivity. In the model, computational time is saved by pre-calculating temperature independent terms and storing them in a matrix so that for each node (m, n), coefficients a, b, c and d are defined containing this information for conduction left, right, up, and down respectively.

For instance, conduction "right" as defined by Equation A.5 is calculated in the software as

$$q_{\alpha\beta} = \frac{b_\alpha(T_\alpha - T_\beta)}{(1/k_\alpha + 1/k_\beta)} \tag{A.6}$$
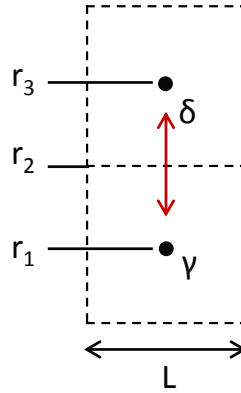
with b_α pre-calculated and defined as

159

Figure A.3: Diagram illustrating two adjacent nodes in the r direction

$$b_\alpha = \frac{\pi(r_2^2 - r_1^2)}{L} \tag{A.7}$$

For conduction in the r direction, consider two adjacent nodes γ and δ as shown in Figure A.3. Heat transfer from node γ to node δ can be defined as

$$q_{\gamma\delta} = \frac{(T_\gamma - T_\delta)}{\frac{\ln(r_1/r_2)}{2\pi L k_\gamma} + \frac{\ln(r_3/r_2)}{2\pi L k_\delta}} \tag{A.8}$$

where r_1, r_2 and r_3 are defined as the location of the lower node, the location of the node boundary, and the location of the upper node respectively and L is defined as the node width. Again, to decrease computation time, temperature independent properties are pre-calculated and stored. However, radial conduction equations require the storage of two constants to accommodate differing geometries when calculating the thermal resistance. This is accomplished by using a three dimensional matrix in MATLAB.

For example, conduction "up" as defined by Equation A.8 is calculated in the software as

160

$$q_{\gamma\delta} = \frac{(T_\gamma - T_\delta)}{\frac{c_{\gamma,1}}{k_\gamma} + \frac{c_{\alpha,2}}{k_\delta}} \tag{A.9}$$

with constants $c_{\gamma,1}$ and $c_{\gamma,2}$ defined as

$$c_{\gamma,1} = \frac{\ln(r_2/r_1)}{2\pi L} \tag{A.10}$$

$$c_{\gamma,2} = \frac{\ln(r_3/r_2)}{2\pi L} \tag{A.11}$$

Ultimately, at each time step, for the original node (m,n) as defined in Figure A.1, the four following equations are used to calculate conduction with adjacent nodes.

$$q_{up,(m,n)} = \frac{(T_{(m,n)} - T_{(m,n+1)})}{\frac{c_{(m,n,1)}}{k_{(m,n)}} + \frac{c_{(m,n,2)}}{k_{(m,n+1)}}} \tag{A.12}$$

$$q_{down,(m,n)} = \frac{(T_{(m,n)} - T_{(m,n-1)})}{\frac{d_{(m,n,1)}}{k_{(m,n)}} + \frac{d_{(m,n,2)}}{k_{(m,n-1)}}} \tag{A.13}$$

$$q_{left,(m,n)} = \frac{a_{(m,n)}(T_{(m,n)} - T_{(m-1,n)})}{1/k_{(m,n)} + 1/k_{(m-1,n)}} \tag{A.14}$$

161

$$q_{right,(m,n)} = \frac{a_{(m,n)}(T_{(m,n)} - T_{(m+1,n)})}{1/k_{(m,n)} + 1/k_{(m+1,n)}} \quad\quad\quad (A.15)$$

162